

Thesis for *Doctor of Philosophy*

The Effect of Mo or W on TiC Coarsening in HSLA Steel

Jang, Jae Hoon (장 재 훈)

Computational Metallurgy

Graduate Institute of Ferrous Technology

Pohang University of Science and Technology

2012

HSLA강 내의 TiC 조대화에 미치는
Mo 와 W 효과

The Effect of Mo or W on TiC
Coarsening in HSLA Steel

The Effect of Mo or W on TiC Coarsening in HSLA Steel

by

Jang, Jae Hoon

Computational Metallurgy

Graduate Institute of Ferrous Technology

Pohang University of Science and Technology

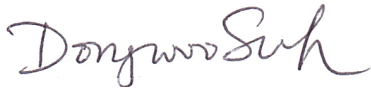
A thesis submitted to the faculty of Pohang University of Science and Technology in partial fulfillment of the requirements for the Doctor of Philosophy in the Graduate Institute of Ferrous Technology (Computational Metallurgy).

Pohang, Korea

30 May 2012

Approved by

Prof. Suh, Dong-Woo



Major Advisor

Prof. Bhadeshia, H. K. D. H.



Co-advisor

The Effect of Mo or W on TiC Coarsening in HSLA Steel

Jang, Jae Hoon

This dissertation is submitted for the degree of Doctor of Philosophy at the Graduate Institute of Ferrous Technology of Pohang University of Science and Technology. The research reported herein was approved by the committee of Thesis Appraisal.

30 May 2012

Thesis Review Committee

Chairman : Suh, Dong-Woo (signature)

Member: Kim, Sung-Joon (signature)

Member: Lee, Byeong-Joo (signature)

Member: Lee, Jae-Kon (signature)

Member: Lee, Jae-Sang (signature)

Preface

This dissertation is submitted for the degree of Doctor of Philosophy at Pohang University of Science and Technology. The research described herein was conducted under the supervision of Professor Suh, Dong-Woo and Professor Bhadeshia, H. K. D. H., Professor of Computational Metallurgy in the Graduate Institute of Ferrous Technology, Pohang University of Science and Technology between March 2007 and June 2012.

This work is to the best of my knowledge original, except where acknowledgements and references are made to previous work. Neither this, nor any substantially similar dissertation has been or is being submitted for any other degree, diploma or other qualification at any other university. This dissertation does not exceed 60,000 words in length.

Part of this work has been published:

J. H. Jang, C. H. Lee, Y. U. Heo and D.W. Suh: Stability of (Ti,M)C (M=Nb, V, Mo and W) carbide in steels using first-principles calculations, *Acta Materialia* 60 (2012) 208-217

DFT Jang, Jae Hoon
20090908 The Effect of Mo or W on TiC Coarsening in HSLA Steel
Department of Ferrous Technology (Computational Metallurgy)
2012, 161 p
Advisor : Suh, Dong-Woo and Bhadeshia, H. K. D. H.
Text in English

Abstract

There is a new vigour in the development of low-alloy steels containing a fine dispersion of substitutionally alloyed carbides. The steels have a microstructure which is essentially ferritic, but with TiC or (Ti,Mo)C particles which are less than 10 nm in size, generated at the austenite-ferrite interface during the course of phase transformation. This interphase precipitation mechanism has been known for a long time, but its application to automotive steels which compete with dual phase and transformation plasticity based alloys is much more recent.

The steels are mass produced and in the final stages are coiled at temperatures in the vicinity of 600°C. A key feature of alloy design, therefore, is the use of the complex (Ti,Mo)C carbide, which is found to coarsen at a much slower rate than the pure TiC, during the cooling of the coil to ambient temperature. The mechanism for the effect of molybdenum is not understood, but it is the fine dispersion of carbides that permits the otherwise weak ferrite to gain sufficient strength to be of use in a variety of engineering applications.

Many of the variants that have been developed also contain niobium as a microalloying addition. High-resolution transmission electron microscopy has been used to characterise the precipitates in Ti-Nb and Ti-Nb-Mo bearing steels, using both thin foil and extracted carbides. In

this way, precipitation and coarsening kinetics have been characterised and form the basis for comparison against mathematical models later in the thesis.

The role of molybdenum has been investigated using wide ranging first-principles calculations for a variety of (Ti,M)C precipitates, where ‘M’ stands for niobium, vanadium, molybdenum or tungsten. The purpose of this was to see whether the molybdenum acts to reduce coarsening by a thermodynamic effect or whether the phenomenon is principally kinetic. In fact, molybdenum has the effect of reducing the stability of TiC, but it at the same time reduces the crystallographic misfit between ferrite and the carbide, and as a consequence, the interfacial energy per unit area. It is this latter parameter which controls coarsening and explains why molybdenum leads to a more stable dispersion. Furthermore, it is found that molybdenum incorporated into the carbide at the early stages of precipitation, is rejected as the carbide grows beyond the nucleation stage, confirming the first principles estimates that its presence in the TiC is not favoured.

In an interesting the results from the *ab-initio* calculations suggest a new alloy system based on (Ti,W)C precipitates which should be as effective as (Ti,Mo)C by the same mechanism, in resisting coarsening.

Finally, a detailed analysis is reported on three different models for representing the observed coarsening behaviours. The first is based on classical Ostwald ripening theory due to Lifshitz, Slyozov and Wagner, which essentially assigns the problem to the diffusion of a ‘controlling’ solute (i.e., a binary alloy), and leads to a result in which the normalised size distribution is invariant with time, even though the small particles dissolve and larger ones grow. A model due to Kampmann and Wagner avoids the assumption of a particular form of particle size distribution, but still treats the problem as if the system concerned is binary. A computational model based on the LSW particle size distribution, but which properly treats multicomponent diffusion has also been studied; this model also

has the advantage of revealing concentration profiles within the matrix as the particles evolve. Naturally, the different models give similar results except for the Kampmann–Wagner method, where the particle size distribution is not invariant with time.

Contents

Contents	v
Nomenclature	xiii
1 Introduction	1
1.1 Experimental Observation of (Ti,Mo)C	2
1.2 Crystal Structure and Orientation Relationship	7
1.3 Thermodynamics and Solubility Product	10
1.4 Interphase Precipitation	14
1.5 Density Functional Theory	18
1.5.1 The <i>Born-Oppenheimer</i> Approximation	19
1.5.2 The Kohn-Sham Equation	20
1.5.3 The Exchange-Correlation Functional	22
1.5.4 The Full-Potential Linearized Augmented Plane- Wave Method	22
1.6 Precipitate	25
1.6.1 Capillarity Effect	25
1.6.2 Nucleation	26
1.6.3 Growth	28
1.6.4 Coarsening	31
References	34

2	Interphase Precipitation	43
2.1	Sample Preparation	44
2.2	Ti-Nb Steel	50
2.2.1	Isothermal Holding at 700°C for 40 min	50
2.2.2	Prolonged Aging at 650°C for 24 h	54
2.2.3	Prolonged Aging at 700°C for 120 h	57
2.3	Ti-Nb-Mo Steel	59
2.3.1	Isothermal Holding at 700°C for 40 min	59
2.3.2	Prolonged Aging at 650°C for 24 h	62
2.3.3	Prolonged Aging at 700°C for 120 h	66
2.4	Hardness and Precipitate Size	74
References	76
 3	 Stability of (Ti,M)C	 77
3.1	Formation Energy and Lattice Parameter	77
3.1.1	Computational Model and Methods	78
3.1.2	Reference States	79
3.1.3	(Ti,M)C Structure	81
3.1.4	M(C,Va) Structure	87
3.2	Interfacial Energy	89
3.2.1	First-Principles Calculations	89
3.2.2	Discrete-Lattice Plane, Nearest-Neighbor Broken-Bond Model	96
3.2.3	(Ti,Mo)C Coarsening	102
3.3	Model Alloys	103
3.3.1	Experimental Procedures	103
3.3.2	Optical Microscopy	106
3.3.3	0.1Ti Alloy	109
3.3.4	0.2Ti Alloy	111
3.3.5	0.1Ti+Mo Alloy	114
3.3.6	0.1Ti+W Alloy	117

NOMENCLATURE

3.3.7 Comparison	120
References	123
4 Coarsening	127
4.1 Lifshitz, Slyozov and Wagner Model	128
4.2 DICTRA Model	134
4.3 Kampmann and Wagner's Numerical Model	146
References	156
5 Conclusions	159

Nomenclature

Roman Symbols

$V_{xc}(r)$	Exchange-correlation potential
Z_I	Atomic number of element I
G^*	Critical activation energy for nucleation
$a_{[M]}$	Activity of element M
N_A	Avogadro's number
C_e	The equilibrium concentration of solute in the matrix
c_M^{MC}	Atomic fraction of M in $(Ti,M)C$ carbide
$E_C[n]$	Classical electrostatic Coulomb energy functional
E_e	Energy eigenvalue depending only on the position of the electrons
r_i	Position vector for electron
$E[n]$	Density functional for the ground state energy
E_{tot}	Energy eigenvalue
f	Volume fraction of carbide
ΔG	Gibbs free energy change of system for the chemical reaction

NOMENCLATURE

ΔG^0	Standard Gibbs free energy change
ΔG_s	Strain energy change per unit volume
ΔG_v	Chemical Gibbs free energy change per unit volume
h	Planck constant
H_{tot}	Hamiltonian operator
R_I	Position vector for nuclei
k	Reciprocal lattice vector
k	Solubility product
T_e	Hamiltonian of electronic kinetic
T_n	Hamiltonian of nuclei kinetic
M_I	Atomic mass of element I
[M]	Weight percent of element M
R	Universal gas constant
r^*	Critical radius for nucleation
r_p	Particle radius in the DICTRA model
r_v	Cell size in the DICTRA model
T	Temperature in Kelvin
Ψ_i	Normalized eigenfunction corresponds to i th eigenvalue
$\tilde{T}[n]$	Kinetic energy functional of non-interacting particles
V_{eff}	Effective potential
v	Interface velocity

NOMENCLATURE

$V_C(r)$	Classical electrostatic Coulomb potential
V_{e-e}	Hamiltonian of interaction part between the electron
V_{ext}	External field from the electrostatic potential generated by the nuclei
V_m	Molar volume of precipitate
V_{n-e}	Hamiltonian of nuclei-electrons interaction
V_{n-n}	Hamiltonian of interaction part between the nuclei
\bar{x}	Mean linear intercept diameter
$E_{xc}[n]$	Exchange-correlation functional
D	Diffusivity of solute

Greek Symbols

ε_i	i th energy eigenvalue
Γ	Capillarity constant
σ_c	Chemical bonding contribution for interfacial energy
$\Delta\sigma$	Increment of yield stress
ε_{xc}	Density functional for exchange-correlation potential
δ	Lattice misfit
ν	ν th sphere
Ψ	Normalized eigenfunction
Ψ_e	Normalized eigenfunction depending only on the position of the electrons

NOMENCLATURE

Ψ^n	Normalized eigenfunction generating electron density n
Ψ_n	Normalized eigenfunction depending only on the position of the nuclei
σ	Interfacial energy
σ_s	Strain contribution for interfacial energy

Other Symbols

a_γ	Austenite lattice parameter
a_α	Ferrite lattice parameter
a_{MoC}	MoC lattice parameter
a_{NbC}	NbC lattice parameter
a_{TiC}	TiC lattice parameter
a_{VC}	VC lattice parameter
a_{WC}	WC lattice parameter
\bar{c}	Average mole fraction of solute
$C_{k,\nu}^G$	Expansion coefficients
$c^{\alpha\beta}$	Equilibrium composition in α with phase β
$c_r^{\alpha\beta}$	Composition in α with phase β with interface curvature r
$c^{\gamma\alpha}$	Mole fraction in austenite in equilibrium with ferrite
$c^{\gamma p}$	Mole fraction in austenite which is in equilibrium with the precipitate
\bar{d}_s	Average sizes of precipitates with respect to 2 dimension

NOMENCLATURE

- $\overline{d_v}$ Average sizes of precipitates with respect to 3 dimension
- $\phi_G(k, r)$ Basis function sets
- σ_s Standard deviation of precipitate sizes with respect to 2 dimension
- $u_l(r)$ Radial part to express inside muffin-tine sphere
- $Y_{lm}(\theta, \phi)$ Spherical harmonics

Acronyms

- APW Augmented plane-wave
- BCC Body centered cubic
- B-R Baker-Nutting
- CALPHAD Calculation of phase diagrams
- DFT Density Functional Theory
- EDS Energy-dispersive X-ray spectroscopy
- FCC Face centered cubic
- FLAPW Full-potential linearized augmented plane-wave
- GGA Generalized gradient approximations
- HSLA High strength low alloy
- K-S Kurdjumov-Sachs
- LAPW Linearized augmented plane-wave
- LDA Local density approximations
- LSW Lifshitz, Slyozov and Wagner
- MT Muffin-tin

NOMENCLATURE

SEM Scanning electron microscopy

STEM Scanning transmission electron microscope

TEM Transmission electron microscopy

Chapter 1

Introduction

Many studies on high-strength low-alloy (HSLA) steels have been conducted bearing in mind applications in the buildings, bridge construction, energy transportation and automotive industries (Jun *et al.*, 2003; Rodrigues *et al.*, 2000; Santos *et al.*, 2003). Of particular importance in such alloys is the role of micro-alloying elements such as titanium, niobium and vanadium, which help control and optimize the microstructure and mechanical properties (Hong *et al.*, 2003). It is in this context that extremely fine TiC particles have been actively investigated for strengthening low-carbon steels (Funakawa & Seto, 2007; Funakawa *et al.*, 2004; Lee *et al.*, 2009; Wang *et al.*, 2011; Yen *et al.*, 2011). It has occasionally been observed that the particles form at the interface between austenite and growing ferrite, via the classical interphase precipitation mechanism. These particles are susceptible to coarsening during subsequent processing, such as in the coiling operation, in which case their contribution to precipitation hardening can be compromised. It has been reported that the coarsening kinetics of TiC particles can be suppressed using certain amounts of molybdenum additions. Early results showed that molybdenum partly substitutes for titanium in the TiC lattice, but its precise role remains unclear.

1.1. Experimental Observation of (Ti,Mo)C

The purpose here was to study the effect of substitutional solutes on the nucleation and coarsening kinetics of (Ti,M)C carbide, where ‘M’ is a metal atom corresponding to niobium (Nb), vanadium (V), molybdenum (Mo) and tungsten (W). The primary goal was to examine both the stability, by using first-principles calculations and transmission electron microscopy (TEM), in terms of the formation energy and interfacial energy of (Ti,M)C and other aspects, such as the dependence of the lattice parameter on solute substitution, in order to reveal the role of molybdenum. Suggestions from the calculations are validated by the characterization of precipitates in a series of steels containing Ti, Ti-Mo and Ti-W, observing the precipitation size and by simulating the coarsening kinetics based on several theories.

1.1 Experimental Observation of (Ti,Mo)C

It is required to maintain a stable distribution of fine precipitate in the steel in spite of high coiling temperature. During the last decades, a relationship between the strength of ferritic steels strengthened by nanometer-sized carbides and coiling temperature has been studied (Fukunakawa & Seto, 2007; Seto *et al.*, 2007; Wang *et al.*, 2011; Yen *et al.*, 2009). The precipitation of (Ti,Mo)C and TiC in ferrite has been analyzed to evaluate the resistance to coarsening and hence the strengthening effect of Ti-Mo bearing and Ti-bearing steels as a function of the coiling temperature.

Figs 1.1 and 1.2 show the results of scanning electron microscopy (SEM) of Ti-Mo and Ti bearing steels and a transmission electron microscopy (TEM) of the precipitates, respectively. The matrix is ferrite in order to obtain a high hole-expansion ratio, with a large number density of fine precipitates with a size on the order of about 3 nm in rows, because tiny form at the interface during the transformation from austenite to ferrite. In Fig. 1.3, TEM images show carbides in Ti-Mo bearing

1.1. Experimental Observation of (Ti,Mo)C

and Ti bearing hot-rolled sheet steels after aging at 650°C for 24 h to check the effect of molybdenum addition. Ti-Mo bearing steel exhibited high strength and hardness even at the high coiling temperature, while the strength of the Ti-bearing steel decreased significantly. Because, the carbides in Ti-bearing steels are much bigger than in the Ti-Mo bearing steels after long time aging (Funakawa & Seto, 2007).

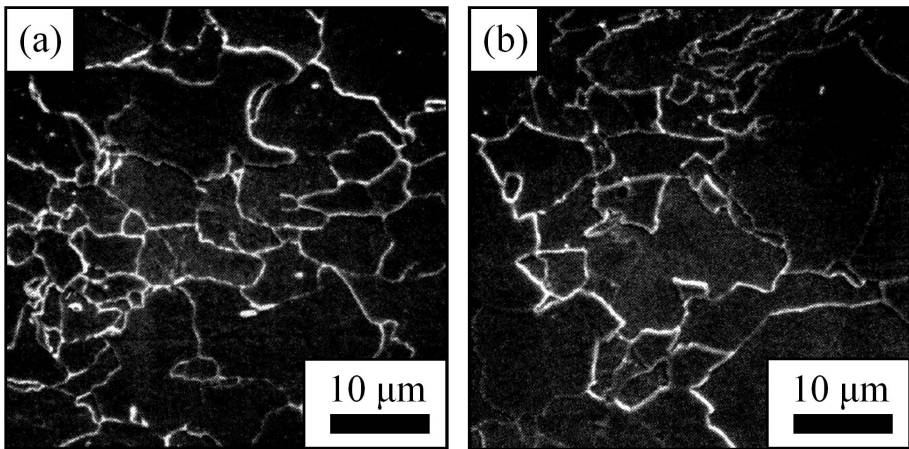


Figure 1.1: Scanning electron micrographs showing microstructure of hot-rolled sheet steels coiled at 625°C for (a) Ti-Mo bearing (b) Ti bearing steel (Funakawa & Seto, 2007).

Fig 1.4 shows the calculation results of the relationship between the amount of precipitates and the increment of strengthening as a function of particle size, assuming the Orowan-Ashby mechanism (Gladman *et al.*, 1977). The yield stress increases, because the dislocation have to move through a field of particles. The increment of yield stress are give as

$$\Delta\sigma(\text{MPa}) = \frac{5.9\sqrt{f}}{\bar{x}} \ln\left(\frac{\bar{x}}{2.5 \times 10^{-4}}\right), \quad (1.1)$$

where \bar{x} is mean linear intercept diameter of the precipitate particles and

1.1. Experimental Observation of (Ti,Mo)C

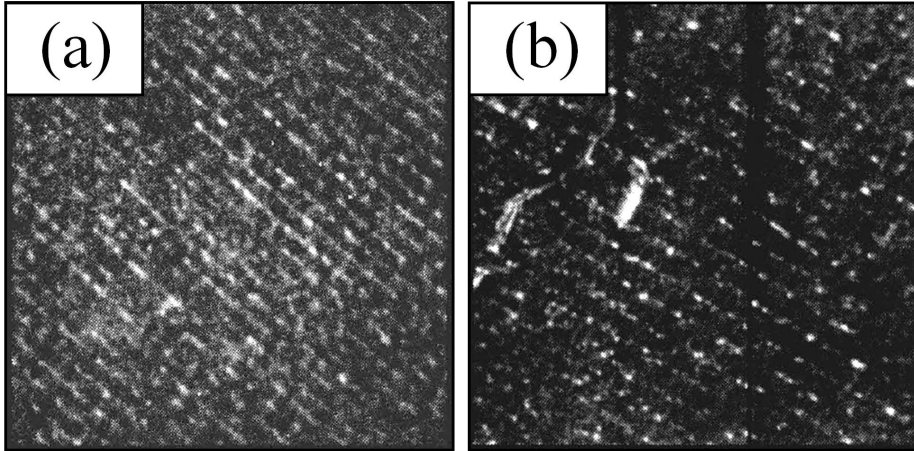


Figure 1.2: Dark field images formed using the (200) reflection of fine carbides in hot-rolled sheet steels for (a) Ti-Mo bearing and (b) Ti bearing steel (Funakawa & Seto, 2007).

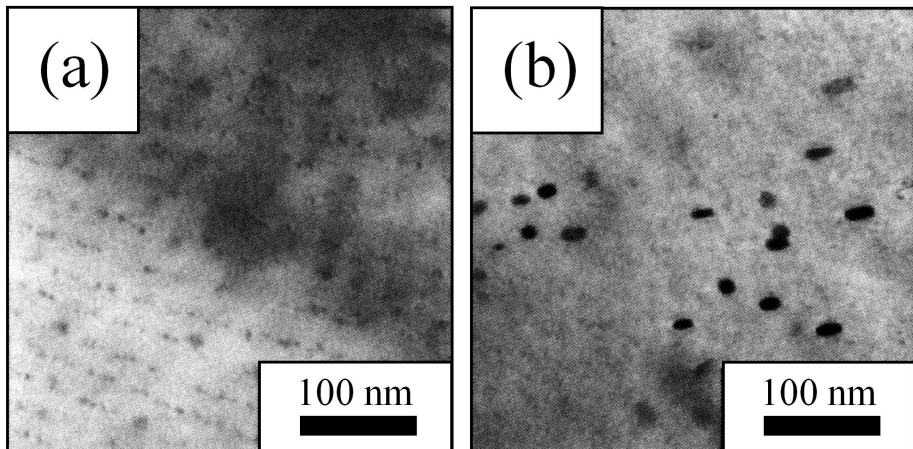


Figure 1.3: Transmission electron micrographs showing carbides in hot-rolled sheet steels after aging at 650°C for 86400 s for (a) Ti-Mo bearing (b) Ti bearing steel (Funakawa & Seto, 2007).

1.1. Experimental Observation of (Ti,Mo)C

f is volume fraction of carbides. From Eq. (1.1), it can be seen that at constant f , precipitate strengthening increases with reduction in particle size and with increase in the particle volume fraction. For the same volume fraction of precipitates, the number density of 1 nm particles should be 1000 times bigger than that of 10 nm precipitates. Because the strength increment is determined by the number density of the precipitates, the strengthening effect of 1 nm sized particle is much higher than that of 10 nm particle assuming that the Orowan mechanism still operates. The significant strength decrease during coiling of Ti-bearing steel is due to the reduction of precipitate density with high coarsening rate compared with Ti-Mo bearing steel. Experimental observations show that unlike TiC, (Ti,Mo)C is not coarsened easily by Ostwald ripening at the high coiling temperature.

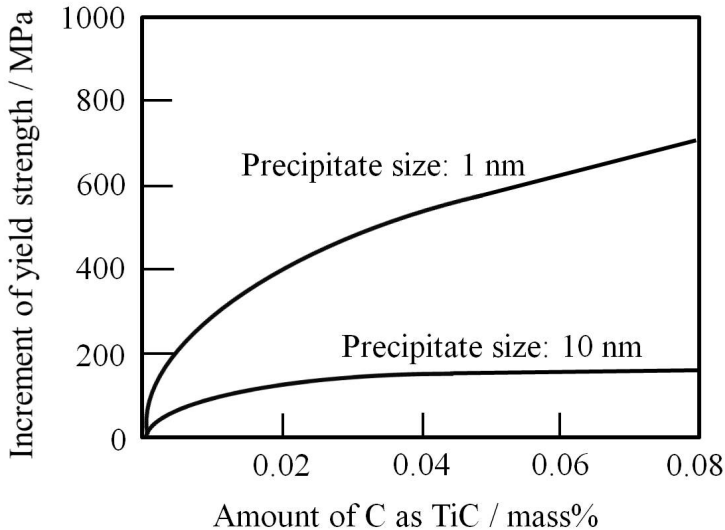


Figure 1.4: Effect of size and amount of precipitates on the increment of tensile strength (Seto *et al.*, 2007).

In previous studies, the Ti/Mo atomic ratio was measured for various

1.1. Experimental Observation of (Ti,Mo)C

sizes of coarsened (Ti,Mo)C precipitates as shown in Fig. 1.5. Small size particles, assumed to correspond to the initial stage of coarsening, contain a relatively large concentration of molybdenum. These results have been interpreted to indicate that titanium is the coarsening-controlling element. It has been confirmed experimentally that the coarsening of precipitates is suppressed by reducing the Ti concentration in a matrix, assumed that the interfacial energy between (Ti,Mo)C and ferrite is same as that of TiC (Funakawa & Seto, 2007). The mechanism governing the role of molybdenum in the coarsening of (Ti,Mo)C particles has not get been resolved (Lee *et al.*, 2009; Wang *et al.*, 2011; Yen *et al.*, 2011).

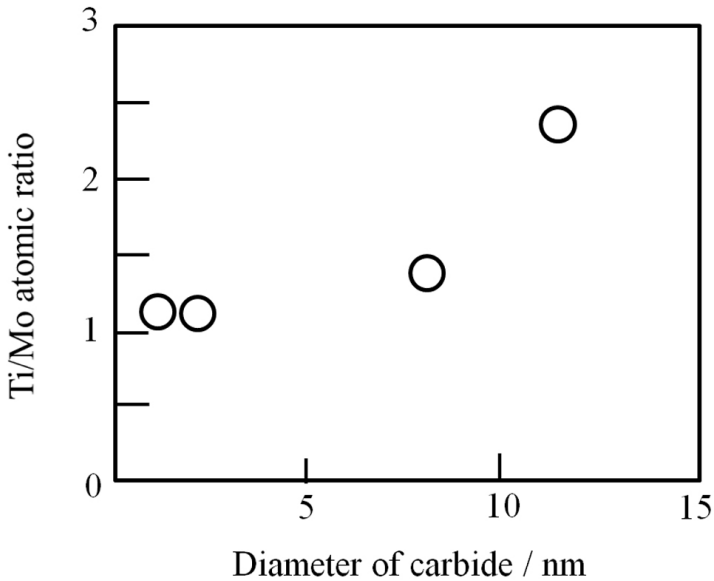


Figure 1.5: Change in Ti/Mo atomic concentration ratio of (Ti,Mo)C with coarsening (Seto *et al.*, 2007).

1.2 Crystal Structure and Orientation Relationship

The carbides TiC, NbC and VC form with the NaCl (B1) crystal structure which is described as face-centered cubic with a motif consisting of a metal atom at (0,0,0) and carbon atom at (0,0, $\frac{1}{2}$). The conventional unit cell for crystal structure of NaCl type carbide is illustrated in Fig. 1.6. The reported lattice parameters are $a_{TiC} = 4.32 \text{ \AA}$, $a_{NbC} = 4.47 \text{ \AA}$ and $a_{VC} = 4.17 \text{ \AA}$ at room temperature (Lipatnikov *et al.*, 1997; Teresiak & Kubsch, 1995). The lattice parameters for MoC and WC with the same crystal structure, determined by preserving the phases through rapid quenching in order to suppress their hexagonal form with the M_2C formula unit, have been reported as $a_{MoC} = 4.28 \text{ \AA}$ and $a_{WC} = 4.27 \text{ \AA}$ (Wilens *et al.*, 1967). These parameters are approximately 1% smaller than that of TiC. Indeed, first-principles calculations suggest the lattice parameters at 0 K to be $a_{MoC} = 4.38 \text{ \AA}$, which is larger than $a_{TiC} = 4.32 \text{ \AA}$, a different tendency relative to the experimental data (Lee *et al.*, 2009). Some results of previous reported experimental and calculated lattice parameters are listed in Table 1.1.

It is observed frequently that the carbide with the B1 crystal structure has a Baker-Nutting (B-R) orientation relationship with the ferrite (Charleux *et al.*, 2001),

$$(100)_\alpha || (100)_{TiC} \quad [010]_\alpha || [011]_{TiC} \quad (1.2)$$

and the misfit strain δ are determined as,

$$\delta = \frac{a_{TiC} - \sqrt{2}a_\alpha}{a_{TiC}}. \quad (1.3)$$

Supposing ferrite and TiC carbide lattice parameters of $a_\alpha = 2.87 \text{ \AA}$ and $a_{TiC} = 4.32 \text{ \AA}$, the lattice misfit (δ) between ferrite and TiC is approxi-

1.2. Crystal Structure and Orientation Relationship

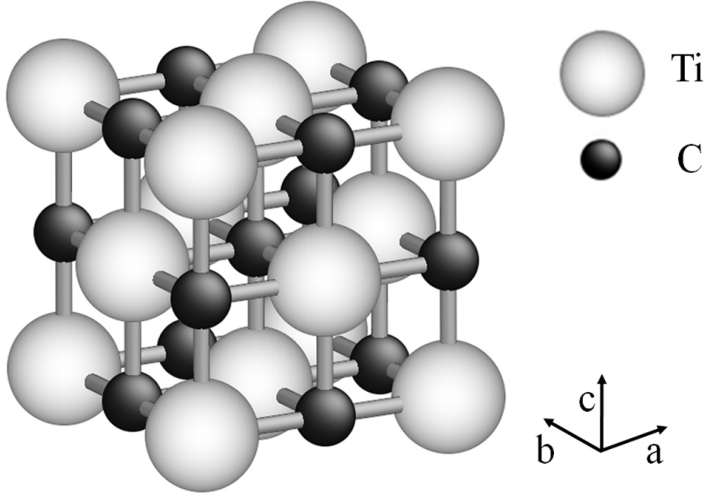


Figure 1.6: Conventional unit cell of NaCl (B1) crystal structure type carbide, which contains four metal atoms at the face-centered cubic position and four carbon atoms at its corresponding octahedral interstitial sites.

Table 1.1: Experimentally measured and calculated lattice parameters for various MC carbides with B1 structure.

type	experimental (298 K) / Å	calculation (0 K) / Å
TiC	4.323 ^a 4.332 ^b	4.27 ^c 4.317 ^d 4.36 ^e 4.38 ^f
NbC	4.468 ^a 4.471 ^b	4.45 ^g 4.470 ^{d,h} 4.476 ^e
VC	4.17 ^{b,i}	4.10 ^g 4.154 ^e 4.159 ^d 4.22 ^f
MoC	4.277 ^j	4.254 ^d 4.278 ^h 4.366 ^e 4.38 ^k 4.42 ^f
WC	4.221 ^b 4.266 ^j	4.336 ^d 4.38 ^{e,f}

^a(Teresiak & Kubsch, 1995), ^b(Nartowski *et al.*, 1999), ^c(Price *et al.*, 1992), ^d(Raju *et al.*, 1992), ^e(Isaev *et al.*, 2007), ^f(Grossman *et al.*, 1999), ^g(Singh & Klein, 1992), ^h(Guillermet *et al.*, 1993), ⁱ(Lipatnikov *et al.*, 1997), ^j(Willens *et al.*, 1967), ^k(Lee *et al.*, 2009)

1.2. Crystal Structure and Orientation Relationship

mately 6.0%. This means that a contraction of the TiC lattice is necessary to maintain coherency at the interface with the ferrite matrix.

Precipitates with a B1 crystal structure, when they are formed in austenite, usually have a cube-cube orientation relationship (Davenport *et al.*, 1975; Enomoto, 1998).

$$(100)_\gamma || (100)_{TiC} \quad [010]_\gamma || [010]_{TiC} \quad (1.4)$$

and the misfit strain δ are determined as,

$$\delta = \frac{a_{TiC} - a_\gamma}{a_{TiC}}. \quad (1.5)$$

During the transformation from austenite to ferrite, the latter usually grows with Kurdjumov-Sachs (K-S) orientation (Bhadeshia & Honeycombe, 2006). The precipitates obtained in austenite matrix at high temperature are observed to have K-S orientation relationship with ferrite at room temperature (Lee *et al.*, 2000). Therefore, the matrix condition can be identified by analyzing the orientation relationship between carbide and matrix. With the lattice parameter of austenite $a_\gamma = 3.56 \text{ \AA}$, the misfit of the TiC lattice for a cube-cube relationship is nearly 18%, which implies that the formation of a coherent interface would be difficult. This is not, however, the case, because a greater coherency is achieved by the Baker-Nutting relation that the carbide adopts with the ferrite when the carbide precipitates at the ferrite-austenite interface.

The electronic structure at interface, the interfacial energy and the interface structure between metal and carbide have been reported for Fe-TiC, Fe-VN, Co-WC and Co-TiC using first-principles calculations (Christensen *et al.*, 2002; Hartford, 2000; Mizuno *et al.*, 1998). The stable atomic arrangement of Fe at the Fe-TiC interface having the Baker-Nutting orientation relationship can be determined from the previous studies. The interface structures assume that the locations of Ti atoms correspond to the positions of Fe atoms in the body-centered cubic struc-

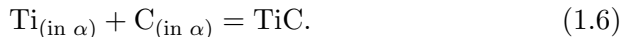
1.3. Thermodynamics and Solubility Product

ture and C atoms are located on the corresponding octahedral interstitial sites.

1.3 Thermodynamics and Solubility Product

The majority of alloying elements used in HSLA steels, including titanium, niobium, vanadium, molybdenum and tungsten will form alloy carbides, which are thermodynamically more stable than cementite. The formation energy and solubility product of metal carbides in austenite and ferrite can help interpret the precipitation process. The chemical properties of transition metal carbides at room temperature have been reported experimentally. The stability of carbides, nitrides and borides of the alloy, which is used frequently in steels, are shown in Fig. 1.7, where the enthalpies of formation are plotted. The formation energies of TiC, NbC and VC have been reported as about -92 , -71 and -59 kJ mol $^{-1}$, respectively (Teresiak & Kubisch, 1995).

Consider the equilibrium reaction between a solid solution of titanium and carbon in ferrite, and its carbide TiC at the given temperature T ,



The Gibbs free energy changes ΔG of the system in the reaction can be expressed as

$$\Delta G = \Delta G^0 + RT \ln\left(\frac{a_{[\text{TiC}]}}{a_{[\text{Ti}]}a_{[\text{C}]}}\right) \quad (1.7)$$

where ΔG^0 is the standard Gibbs free energy change for the chemical reaction at the temperature T . The standard Gibbs free energy is the difference between the sum of the Gibbs free energies of the reaction products in their standard states and the sum of the Gibbs free energies of the reactants in their standard states. $a_{[\text{TiC}]}$, $a_{[\text{Ti}]}$ and $a_{[\text{C}]}$ are the activities of the TiC in ferrite, the dissolved Ti and the dissolved C,

1.3. Thermodynamics and Solubility Product

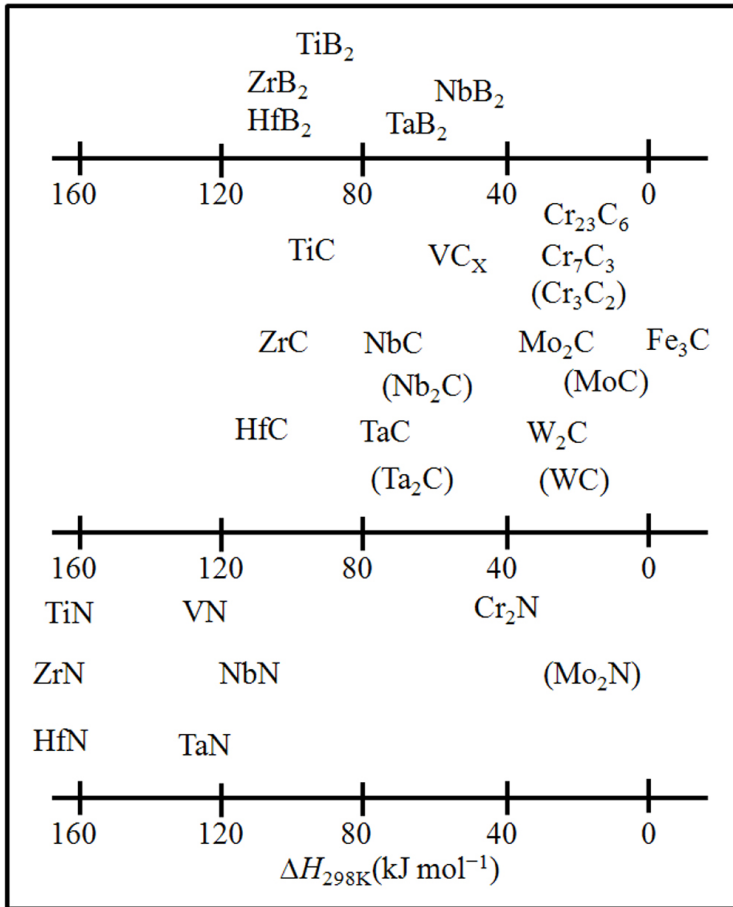


Figure 1.7: Enthalpies of formation of carbides, nitrides and borides at room temperature (Schick, 1966).

1.3. Thermodynamics and Solubility Product

respectively. Since $\Delta G = 0$ at the equilibrium,

$$\frac{-\Delta G^0}{RT} = \ln\left(\frac{1}{a_{[Ti]}a_{[C]}}\right) \quad (1.8)$$

when $a_{[Ti]}$ is taken as one for a pure substance. The equation can be rewritten as

$$\ln(a_{[Ti]}a_{[C]}) = \frac{\Delta G^0}{RT} = \frac{\Delta H^0}{RT} - \frac{\Delta S^0}{R}. \quad (1.9)$$

Then the temperature dependency of solubility product $k = [Ti] \times [C]$ can be expressed based on the Arrhenius equation assumed that $a_{[M]} = [M]$.

$$\ln(k) = A - \frac{B}{T} \quad (1.10)$$

Therefore, it is possible to calculate the equilibrium amount of precipitate at a given temperature by using Eq. (1.10) if A and B are known. The solubility relationships for titanium carbide in austenite and ferrite phases are measured experimentally and calculated based on thermodynamics databases (Akben *et al.*, 1984; Taylor, 1995).

$$\log[Ti][C] = -\frac{7000}{T} + 1.986 \text{ (in austenite)} \quad (1.11)$$

$$\log[Ti][C] = -\frac{9575}{T} + 4.40 \text{ (in ferrite)} \quad (1.12)$$

where $[Ti]$ and $[C]$ are in the units of weight percent of Ti and C. T is temperature in a unit of K .

Fig. 1.8 contains a comparison of the solubility products of vanadium carbide (VC), titanium carbide (TiC), niobium carbide (NbC), niobium nitride (NbN) and titanium nitride (TiN) in austenite and in ferrite, respectively. The solubility for carbides is lower than in the austenite at temperatures in the ferrite range, and the difference of TiC is relatively small compared with NbC and VC. Therefore, the carbides can be precipitated during the transformation from austenite to ferrite as interphase

1.3. Thermodynamics and Solubility Product

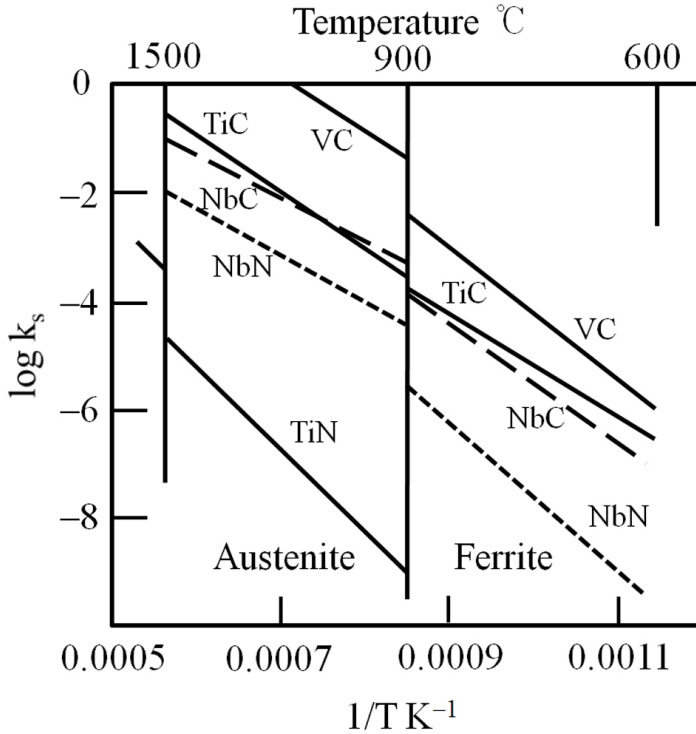


Figure 1.8: Temperature dependence of the solubility products of vanadium carbide (VC), titanium carbide (TiC), niobium carbide (NbC), niobium nitride (NbN) and titanium nitride (TiN) in austenite and in ferrite, respectively (Gladman *et al.*, 1977).

1.4. Interphase Precipitation

precipitates. It is necessary to reheat above 1250°C to resolve titanium nitride, because it shows small solubility product relative to that of the carbide.

1.4 Interphase Precipitation

Investigations of carbide precipitation during from the austenite to ferrite transformation in alloy steels have proposed the different modes of the carbide formation in steels, other than the morphology of pearlite (Howell *et al.*, 1980; Ricks & Howell, 1983; Ricks *et al.*, 1982; Smith & Dunne, 1988). Carbides can precipitate through different processes, such as (1) nucleation in austenite, (2) formation of rows of carbides during the austenite-ferrite interphase transformation, (3) fibers growing normal to the slowest moving austenite-ferrite boundary and (4) precipitation of fine carbides from supersaturated ferrite solid solutions (Honeycombe & Mehl, 1976). Interphase precipitates may form at ferrite-austenite interfaces during cooling from the austenite or isothermal heat treatment in a ferrite phase field. These precipitates align parallel to planar segments of ferrite-austenite interfaces. The strengthening effect of interphase precipitation is important for the development of strong and tough hot-rolled steels which rely on a low carbon concentration. The particles formed during interphase precipitation or in ferrite after the phase transformation, can be very small, on the order of 5 nm, and are effective as strengthening agents.

The features of the interphase precipitates have been reported extensively in the previous literature. Smith and Dunne studied the morphologies of inter-phase precipitation carbides in different micro-alloyed steels, and summarized them into (1) planar interphase precipitation with regular sheet spacing, (2) curved interphase precipitation with regular sheet spacing, and (3) curved inter-phase precipitation with irregular sheet spacing as in Fig. 1.9 (Smith & Dunne, 1988). A few models have

1.4. Interphase Precipitation

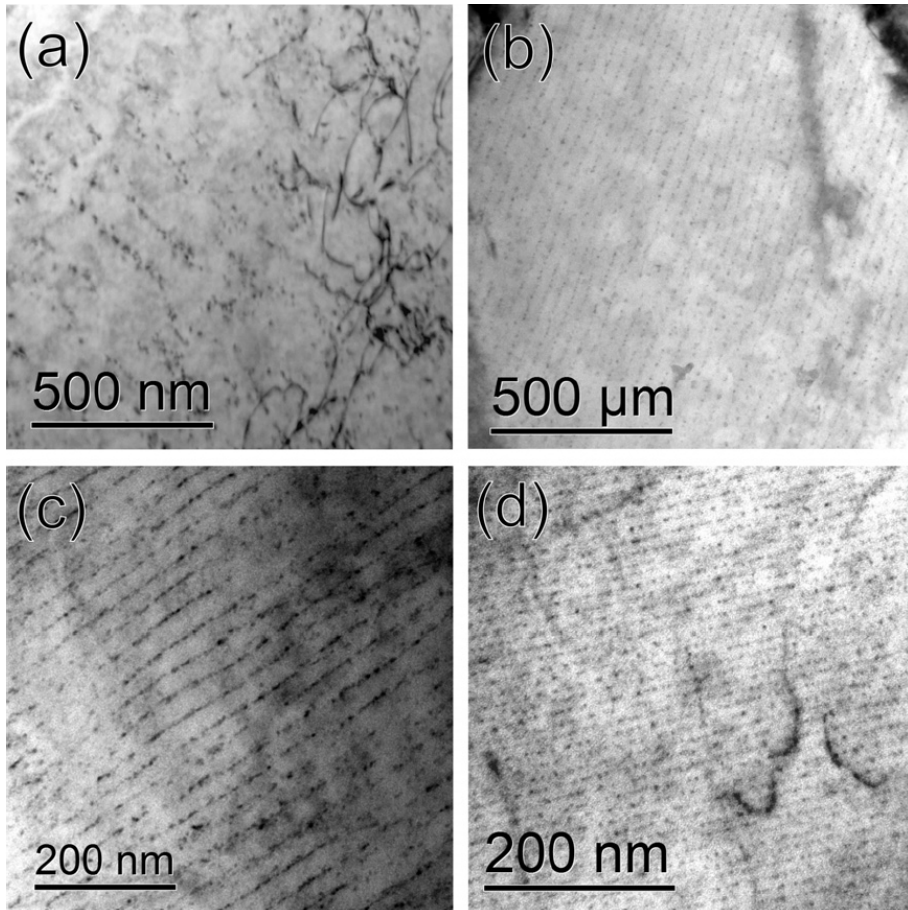


Figure 1.9: Transmission electron micrographs showing (a) curved with irregular spacing (b) curved with regular spacing (c) a mixture of planar and curved with regular spacing and (d) planar with regular spacing interphase precipitates in a titanium-molybdenum bearing low carbon steel (Yen *et al.*, 2011).

1.4. Interphase Precipitation

been proposed to illustrate the interphase precipitation reaction and these models can be classified to two groups as based on ledge mechanism and based on solute drag mechanism (Li & Todd, 1988).

The first group is further subdivided into ledge, quasi-ledge, and bowing mechanisms although the temperature dependencies and transitions between such mechanisms are not well established. The bowing mechanism was proposed to account for the curved boundary based on the effect of nucleated precipitation on the mobility of high energy interphase boundaries (Ricks & Howell, 1983). The quasi-ledge mechanism was proposed for precipitation on high energy, disordered, austenite-ferrite interphase boundaries which have been immobilized by copious precipitation, forming curved sheets of precipitates (Ricks & Howell, 1983).

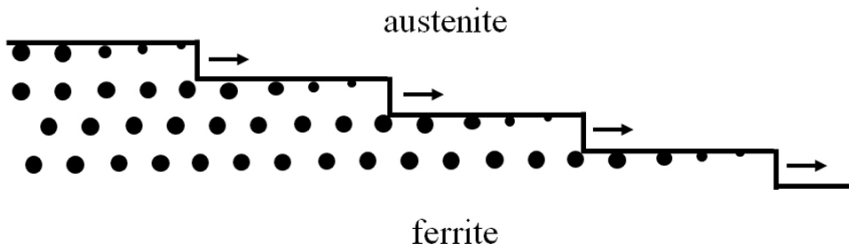


Figure 1.10: A schematic diagram of the mechanism of nucleation and growth of carbides on the austenite-ferrite interface for regular ledge heights (Davenport & Honeycombe, 1971).

The planar interphase precipitation has long been accepted to be associated with the ledge mechanism of growth as illustrated in Fig. 1.10, of a partially coherent austenite-ferrite interface motion (Davenport & Honeycombe, 1971). Such interfaces within a single austenite grain are seldom curved. They are composed of planar facets joined by ledges. The regularly spaced sheets of precipitate particles are nucleated at the interface and grow further in the ferrite. The ledges are probably non-coherent

1.4. Interphase Precipitation

and move too rapidly for nucleation of carbides to occur on them. The ledge height is often uniform and a between 5 and 50 nm, but sometimes it may vary.

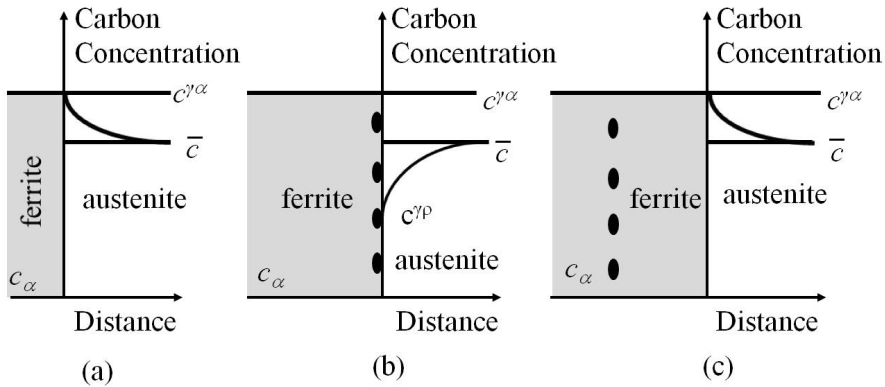


Figure 1.11: Schematic model of interphase precipitation (a) Carbon concentration in austenite increases at the ferrite-austenite boundary. (b) The carbon concentration promotes carbide nucleation on the ferrite side of the boundary. (c) The process repeated again. (Davenport & Honeycombe, 1971).

The second group, which is based on solute drag mechanism, considers nucleation at or behind a moving interface. Davenport & Honeycombe (1971) have suggested a concepts of solute-drag nucleation model which is illustrated in Fig. 1.11, where \bar{c} , $c^{\gamma\alpha}$ and $c^{\gamma\rho}$ indicate the average mole fraction of solute in austenite, mole fraction in austenite in equilibrium with ferrite and mole fraction in austenite which is in equilibrium with the precipitate, respectively. This model suggests a buildup of carbon in the austenite ahead of the moving boundary, which aids the nucleation of carbides at the boundary. Such nucleation also can be assisted by the drag of substitution solutes by the advancing boundary. Pinning the boundary and depletion of the carbon concentration can occur in the austenite. The depletion of carbon increases the driving force for the transformation of

1.5. Density Functional Theory

austenite, moving the boundary away from the precipitate particles and the previous process should be repeated.

Roberts has proposed a solute depletion model, which is a diffusion model in which nucleation of carbide was assumed to take place immediately behind a smooth migrating interface (Roberts & Sandberg, 1980). The growth rate of depleted area is very fast at the initial stages of nucleation, but it slows down following a parabolic rate. The solute concentration reaches to the local equilibrium after certain amount of traveling. Solute depletion of the ferrite matrix, as the precipitates grew, would then be responsible for the repeated coplanar arrays of the interphase precipitates.

A solute balance model has been developed by Li & Todd (1988). This model assumes that the diffusion profile developed by the growing sheet of interphase precipitates is similar to that resulting from the growth of pseudo-phase of constant composition equal to the average solute concentration in the sheet. It assumes that the solute lost by the depleted layer during growth is equal to the excess solute found in the sheet. This model provides a theoretical rationale for the correlations among parameters including transformation temperature, sheet spacing, sheet width and average boundary velocity.

1.5 Density Functional Theory

A solid consists of nuclei and electrons which are classified into two groups; valence electrons which contribute to chemical bonding and core electrons which are tightly bound in the closed shells of the lattice nucleus. In principle, the solution of the many-body Schrödinger's equations with electrons and nuclei, for a given solid, gives all possible information. However, it is impractical to solve the many-body coupled-equation directly. Density functional theory (DFT) is the most commonly used first-principles calculation for materials simulations. The definition of 'First-

1.5. Density Functional Theory

principles' is the calculation of electronic structure using Schrödinger's equation within a set of approximations that do not include fitting the model to experimental data. In first principles calculation, the total energy is calculated by following equations:

$$H_{tot}\Psi(\{R_I\}, \{r_i\}) = E_{tot}\Psi(\{R_I\}, \{r_i\}) \quad (1.13)$$

where Ψ and E_{tot} represent the normalized eigenfunction and the energy eigenvalue of the Hamiltonian operator H_{tot} . R_I and r_i are the position vector sets for nuclei and electronic positions. The Hamiltonian of a solid consists of the nuclei kinetic T_n and electronic kinetic T_e part and the interaction part between the nuclei V_{n-n} and electrons V_{e-e} with nuclei-electrons interaction V_{n-e} .

$$H_{tot} = T_n + V_{n-n} + T_e + V_{e-e} + V_{n-e} \quad (1.14)$$

$$H_{tot} = - \sum_i \frac{1}{2} \nabla_i^2 + \sum_{i \neq j} \frac{1}{|r_i - r_j|} - \sum_I \frac{1}{2M_I} \nabla_I^2 + \sum_{I \neq J} \frac{Z_I Z_J}{|R_I - R_J|} - \sum_{i,I} \frac{Z_I}{|r_i - R_I|} \quad (1.15)$$

where Z_I are the atomic mass of nuclei. Since the Schrödinger's equation Eq. (1.13) has complex structure, it is necessary to use a variety of approximations to reach a practical solution.

1.5.1 The *Born-Oppenheimer* Approximation

The *Born-Oppenheimer* or *adiabatic* approximation was proposed in the early days of quantum mechanics (Bates *et al.*, 1950; Jost & Pais, 1951; Kohn & Rostoker, 1954). The masses of the nuclei of the solid are heavy with respect to those of the electrons, so nuclei by comparison have almost no wave-like properties. The nuclei are not much affected by the movements of the electrons, but the electrons do respond to the motions of the nuclei. It is possible to approximate the positions of nuclei as being fixed, with respect to the electron motion. This allows the wave-function

1.5. Density Functional Theory

to the decoupling into the electrons and nuclei components.

$$\Psi(\{R_I\}, \{r_i\}) = \Psi_n(\{R_I\}) \times \Psi_e(\{r_i\}|\{R_I\}) \quad (1.16)$$

where Ψ_n and Ψ_e are a function depending only on the position of the lattice nuclei and electrons, respectively (Springborg, 1997).

$$\{T_e + V_{e-e} + V_{n-e}(R_I)\}\Psi_e = E_e(R_I)\Psi_e \quad (1.17)$$

$$\{T_n + V_{n-n} + E_e(R_I)\}\Psi_n = E_{tot}\Psi_n. \quad (1.18)$$

Most problems in solid state physics are reduced to the solution of Eq. (1.17), with N -electrons permeating a given static nucleus array, in a solid.

1.5.2 The Kohn-Sham Equation

In the mid 1960's, new approach for obtaining the ground state of a given many electron system was suggested by Hohenberg & Kohn (1964). They derived the basic theorems of the density functional formalism that the electron density $n(r)$ determines uniquely the external potential $V_{ext}(r)$ using the variational principle. This implies that the ground-state energy is a functional of $n(r)$, since electron kinetic part T_e and electron-electron interaction contribution V_{e-e} is determined by electron density naturally. Eq. (1.17) can be rewritten as

$$\{T_e + V_{e-e} + \sum_{i=1}^N V_{ext}(r_i)\}\Psi(r_1, \dots, r_N) = E\Psi(r_1, \dots, r_N) \quad (1.19)$$

where, r_i is the position of the i th electron, N is the total number of electrons, V_{ext} is the external field in which the electrons move which is the electrostatic potential generated by the nuclei, whose positions are assumed fixed and whose spatial movements are assumed negligible. Then

1.5. Density Functional Theory

the density functional for ground state energy $E[n]$ can be as

$$\begin{aligned}
 E[n] &= \int V_{ext}(r)n(r)dr + \langle \Psi^n | T + V_{e-e} | \Psi^n \rangle \\
 &= \int V_{ext}(r)n(r)dr + T[n] + E_C[n] + E_{xc}[n] \quad (1.20) \\
 &= \int V_{ext}(r)n(r)dr + \frac{1}{2} \int V_C(r)n(r)dr + E_{xc}[n],
 \end{aligned}$$

where $E_C[n]$ and $V_C(r)$ are the classical electrostatic Coulomb energy and potential, respectively, and $E_{xc}[n]$ is exchange-correlation functional which is everything not contained in the other term, and its approximation determines the quality of practical applications and their results. The problem is then reformulated to a single quasi-electron Schrödinger-like equation to obtain the appropriate energy functional of the system (Kohn *et al.*, 1965; Sham & Kohn, 1966).

$$\frac{\delta E[n]}{\delta n} = V_{ext}(r) + V_C(r) + \frac{\delta E_{xc}[n]}{\delta n} = \frac{\delta \tilde{T}[n]}{\delta n} + V_{eff}(r) \quad (1.21)$$

where $\tilde{T}[n]$ is the kinetic energy of these non-interacting particles. The advantage of the fictitious particles is that it is possible to solve the Schrödinger-like equation which is a single-particle equation of the form

$$\left[-\frac{1}{2}\nabla^2 + V_{eff} \right] \Psi_i(r) = \varepsilon_i \Psi_i(r) \quad (1.22)$$

Comparing the Eq. (1.20) with Eq. (1.21), the effective potential given by

$$\begin{aligned}
 V_{eff}(r) &= V_{ext}(r) + V_C(r) + \frac{\delta E_{xc}[n]}{\delta n} + \left(\frac{\delta T[n]}{\delta n} - \frac{\delta \tilde{T}[n]}{\delta n} \right) \quad (1.23) \\
 &\equiv V_{ext}(r) + V_C(r) + V_{xc}(r)
 \end{aligned}$$

where $V_{xc}(r)$ is the exchange-correlation potential.

1.5.3 The Exchange-Correlation Functional

The remaining major problem with DFT is that the exact functional for exchange and correlation are not known except for the free electron gas. However, approximations exist which permit the calculation of certain physical quantities quite accurately. The most widely used approximations are the local density approximation (LDA) and generalized gradient approximations (GGA). The LDA method suggested by Hedin and Lundqvist based on the assumption that $V_{xc}(r)$ depends on the local electron density at the point r (Hedin & Lundqvist, 1971).

$$E_{xc}^{LDA} = \int \varepsilon_{xc}(n(r)) n(r) dr \quad (1.24)$$

The GGA method is still local, but it also takes into account the gradient of the density at the same point (Perdew *et al.*, 1996).

$$E_{xc}^{GGA} = \int \varepsilon_{xc}(n(r), \nabla n(r)) n(r) dr \quad (1.25)$$

Unlike the LDA scheme, where the energy functional has a known form, the form $\int \varepsilon_{xc}(n(r), \nabla n(r))$ is unfixed. There is a large amount of variation in determining their form, since there is no specific physical system to fit.

1.5.4 The Full-Potential Linearized Augmented Plane-Wave Method

The solution of many electron problems has been changed to an eigenvalue problem of single particle Kohn-Sham equation, Eqs (1.22) and (1.23).

$$\left[-\frac{1}{2} + V_{ext}(r) + V_C(r) + V_{xc}(r) \right] \Psi_i(r) = \varepsilon_i \Psi_i(r). \quad (1.26)$$

1.5. Density Functional Theory

A lot of methods have been proposed for solving Eq. (1.26) for different applications, geometries, symmetries, chemical elements and materials requiring different approximations (Blügel & Bihlmayer, 2006). The eigenvalue problem Eq. (1.26) is directly related to choosing basis function sets $\{\phi_G(k, r)\}$ for all reciprocal lattice vectors up to G to the largest value of K_{max} ,

$$\Psi_{k,\nu}(r) = \sum_{|k+G| \leq K_{max}} C_{k,\nu}^G \phi_G(k, r) \quad (1.27)$$

where $C_{k,\nu}^G$ are variational coefficients with the reciprocal lattice vector k for the ν th sphere (Blügel & Bihlmayer, 2006). Using Eq. (1.27), the partial differential equation Eq. (1.26) can be solved through algebraic equations which gives the values of $C_{k,\nu}^G$'s.

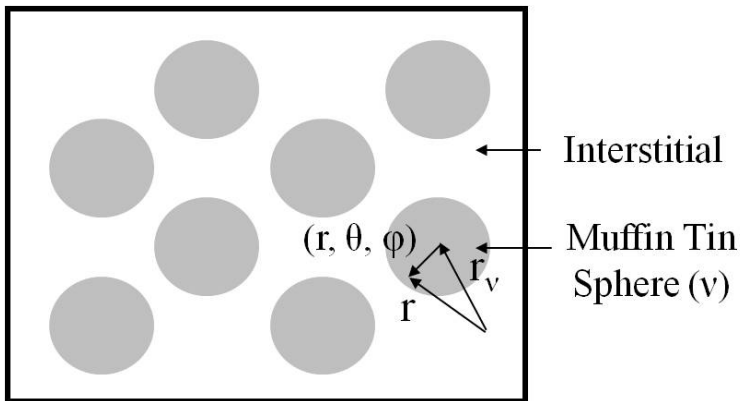


Figure 1.12: Space division both in the APW and LAPW methods.

The Bloch theorem gives the most straightforward suggestion for three dimensional periodic solids, which would be to expand the wave function into plane-waves or Fourier series, respectively,

$$\phi_G(k, r) = e^{i(k+G) \cdot r}. \quad (1.28)$$

1.5. Density Functional Theory

Slater developed the augmented plane-wave (APW) method in which the space is partitioned into spheres centered at each atom site, which is strongly varying but nearly spherical, the so-called muffin-tin (MT) sphere, and into the remaining interstitial region as in Fig. 1.12 (Slater, 1937). Koelling and independently Andersen proposed a linearization method in the radial functions inside the MT sphere, i.e., the basis functions inside the spheres are linear combinations of $u_l(r)Y_{lm}(\theta, \phi)$ and its radial derivative $u_l'(r)Y_{lm}(\theta, \phi)$ (Andersen, 1975; Koelling & Arberman, 1975).

$$\phi_G(k, r) = \begin{cases} e^{i(k+G)\cdot r} & r \in \text{Interstitial} \\ \sum_{lm} \{A_{lm}^\nu u_l(r) + B_{lm}^\nu u_l'(r)\} Y_{lm}(\theta, \phi) & r \in \text{MT sphere } \nu. \end{cases} \quad (1.29)$$

The radial function $u_l(r)$ satisfies

$$\left\{ -\frac{d^2}{dr^2} + \frac{l(l+1)}{r^2} + V_\nu(r) - E_l \right\} r u_l(r) = 0, \quad (1.30)$$

where V_ν is the spherically symmetric potential inside the ν -th sphere and E_l is the angular momentum dependent energy parameter. The spherical harmonics $Y_{lm}(\theta, \phi)$, which is used to illustrate an atomic orbital of hydrogen atom, is the solution of the angular part of Laplace's equation $\nabla^2 f = 0$. These functions are matched to the values and derivatives of the plane-waves on the sphere boundaries and the basis functions augmented in the way are the linearized APW (LAPW) method. Harmann and Weinert have introduced the full-potential LAPW (FLAPW) method which solves the non-spherical potential problem by partitioning the region to vacuum, interstitial and MT sphere regions (Hamann, 1979; Wimmer *et al.*, 1981).

1.6 Precipitate

The precipitation process in a matrix can be classified nucleation, growth and coarsening. All the often separated stages occur simultaneously, governed by interfacial energy and the chemical free energy change. The fact that an interface must be created requires the forming particle to cross a size threshold before there is a reduction in free energy. Even after this stage, curved interfaces change local equilibrium, an effect known as capillarity.

1.6.1 Capillarity Effect

When atoms are transferred from α to the β phase, there is an additional energy term due to the increase in interfacial area and capillarity pressure of the particles. There will be a change in the equilibrium composition of the matrix as an effect of the curvature as shown in Fig. 1.13. Let σ be the interfacial energy per unit area between α and β phase, then the additional free energy of particles with radius r should be,

$$G = 4\pi r^2 \sigma. \quad (1.31)$$

Let dn moles of atoms are moved from α to β phase, dr and dV be the radius and volume changes of particles then the additional free energy $\frac{dG}{dn}$ be

$$\frac{dG}{dn} = \frac{dG}{dr} \times \frac{dr}{dV} \times \frac{dV}{dn}. \quad (1.32)$$

Since $\frac{dV}{dn}$ is the constant molar volume V_m of β phase and $V = \frac{4}{3}\pi r^3$, the free energy increment with respect to particles with curvature r should be

$$\frac{dG}{dn} = 8\pi r \sigma \times \frac{1}{4\pi r^2} \times V_m = \frac{2\sigma V_m}{r}. \quad (1.33)$$

For an infinite radius of curvature, the original composition of the matrix α equilibrium with phase β would be $c^{\alpha\beta}$, but the composition will be in-

creased to $c_r^{\alpha\beta}$ with interface curvature r . Thus, the change in composition becomes

$$c_r^{\alpha\beta} = \left(1 + \frac{2\Gamma}{r}\right) c^{\alpha\beta} \quad (1.34)$$

$$\Gamma = \frac{\sigma V_m}{kT(c^{\beta\alpha} - c^{\alpha\beta})} \quad (1.35)$$

where Γ is the capillarity constant given by the dilute solution approximation.

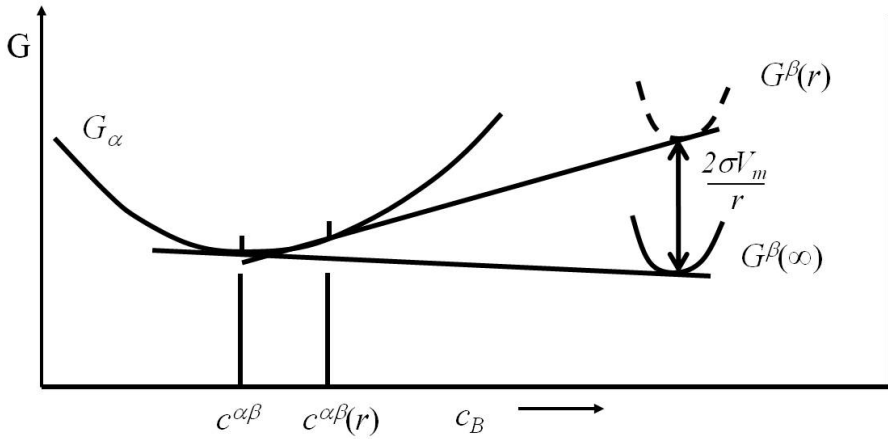


Figure 1.13: Increase of the Gibbs energy due to the interfacial energy of the particle (Christian, 2002).

1.6.2 Nucleation

Nucleation is the process through which the smallest particle of a new phase is formed such that it can grow with a reduction in free energy. The embryo is created by statistical fluctuations involving individual atom additions. It evolves to a critical size whose growth leads to a reduction in free energy. Assuming that the precipitate nucleates as a spherical particle of radius r , a fluctuation of size leads to a change in the free

energy by an amount ΔG given by

$$\Delta G = \frac{4}{3}\pi r^3 \Delta G_v + \frac{4}{3}\pi \Delta G_s + 4\pi r^2 \sigma \quad (1.36)$$

where ΔG_v is the chemical free energy change per unit volume, which is negative during the transformation to precipitate phase, ΔG_s is the strain energy per unit volume associated with creation of precipitates, and σ is the interfacial energy per unit area of the precipitate-matrix interface. The maximum value of ΔG with respect to r gives the activation free energy G^* to form a nucleus of critical radius r^* (Aaronson *et al.*, 1978).

$$G^* = \frac{16\pi\sigma^3}{3(\Delta G_v + \Delta G_s)^2} \quad (1.37)$$

$$r^* = \frac{2\sigma}{\Delta G_v + \Delta G_s}. \quad (1.38)$$

If V_m , R and T are defined as the precipitate molar volume, universal gas constant and temperature, respectively, the activation free energy G^* can be expressed in terms of the precipitate and matrix concentrations by substitution of $\Delta G_v + \Delta G_s$ as (Christian, 2002)

$$\Delta G_v + \Delta G_s = \left(\frac{1}{V_m}\right) RT \ln \left(\frac{\bar{c}}{c^{\alpha\beta}}\right). \quad (1.39)$$

A relationship between r^* and the concentrations can be obtained from Eqs (1.38) and (1.39)

$$\frac{2\sigma V_m}{r^*} = RT \ln \left(\frac{\bar{c}}{c^{\alpha\beta}}\right). \quad (1.40)$$

The rate of nucleation is

$$I = N \frac{RT}{hN_A} \exp \left(-\frac{G^* + Q^*}{RT} \right) \quad (1.41)$$

where Q^* is the activation energy required to transfer atoms across the precipitate interface, N is the number density of nucleation sites for the precipitate, N_A is the Avogadro constant, h is the Planck constant (Christian, 2002). The critical radius of the nucleus can be approximated by using capillarity constant Γ (San Martín *et al.*, 2005),

$$\rho_c = \frac{2c^{\alpha\beta}\Gamma}{(\bar{c} - c^{\alpha\beta})}. \quad (1.42)$$

1.6.3 Growth

Zener proposed a simple theory for the precipitation in dilute solutions of matrix considering one dimensional growth (Zener, 1949). Fig. 1.14 shows a schematic plot of the concentration of the solute as a function of distance in which the concentration is expressed in atoms per volume. For the migration of the interface between precipitates and matrix, there should be a movement of solute atoms at the interface. The rate at which solute is incorporated into the growing precipitate must be equal to that arriving by diffusion to the interface.

Let the composition of the matrix α equilibrium with phase β and the composition of β phase equilibrium with α be $c^{\alpha\beta}$ and $c^{\beta\alpha}$ respectively, then the following equation are derived from Fick's first law.

$$J = -D \left(\frac{dc}{dx} \right) = (c^{\beta\alpha} - c^{\alpha\beta})v \quad (1.43)$$

where J is the flux or number of solute atoms crossing unit area per second, D is the diffusion coefficient which is assumed to be independent of concentration, and $\frac{dc}{dx}$ is the concentration gradient of the solute component in the matrix at the interface and v is the interface velocity. Zener gave an approximate solution to this equation based on the drawing of Fig. 1.14 (Zener, 1949). Substituting approximate slope into the

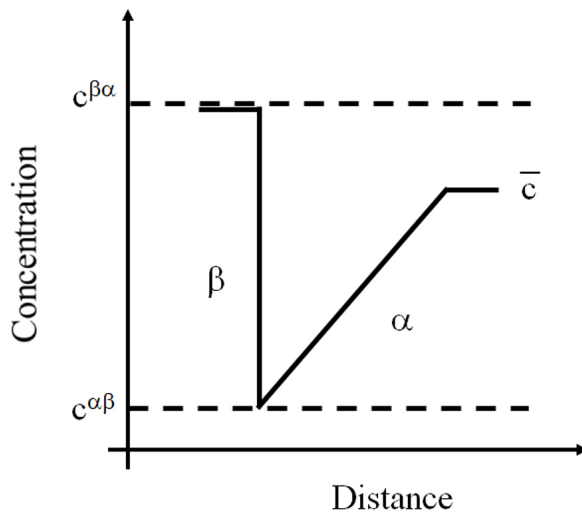


Figure 1.14: A planar precipitate growing under conditions, where growth is controlled by diffusion, showing schematically how the composition varies with distance.

velocity equation yields

$$v = \frac{dx}{dt} = \frac{D(\bar{c} - c^{\alpha\beta})^2}{(c^{\beta\alpha} - c^{\alpha\beta})(c^{\beta\alpha} - \bar{c})x}. \quad (1.44)$$

Integration of this differential equation leads to the following relation for the position of the boundary as a function of time.

$$x = \alpha\sqrt{DT} \quad (1.45)$$

$$\alpha = \frac{\bar{c} - c^{\alpha\beta}}{(c^{\beta\alpha} - c^{\alpha\beta})(c^{\beta\alpha} - \bar{c})}. \quad (1.46)$$

These results have a very general application and Zener has shown that whenever the growth is controlled by a simple diffusion process of the type indicated above, the interface position varies with the square root of the time (Zener, 1949). Zener also obtained several asymptotic approximations of the values of α for three dimensional cases for spherical precipitates, which can be illustrated as Eq. (1.45).

Zener's growth model has been extended to approximately account for capillarity effect (Bhadeshia, 2003; Rivera-Díaz-Del-Castillo & Bhadeshia, 2002). The development of the radius of the spherical precipitate is assumed to follow the Eq. (1.45). At a radius r with the origin located at the center of the particle, the concentration field can be described by applying modified boundary condition by capillarity effect as

$$c(t, r) = \bar{c} + \left[\left(c^{\alpha\beta} + \frac{2c^{\alpha\beta}\Gamma}{\rho} \right) - \bar{c} \right] \frac{\Phi(r/\sqrt{Dt})}{\Phi(\alpha)} \quad (1.47)$$

$$\Phi(\alpha) = \frac{1}{\alpha} \exp\left(-\frac{\alpha^2}{4}\right) - \frac{\sqrt{\pi}}{2} \operatorname{erfc}\left(\frac{\alpha}{2}\right) \quad (1.48)$$

where \bar{c} is the average solute concentration in the matrix. Then Eqs (1.43)

and (1.44) can be reformulated as

$$v \left[c^{\beta\alpha} - \left(c^{\alpha\beta} + \frac{2c^{\alpha\beta}\Gamma}{\rho} \right) \right] = D \frac{\partial c}{\partial r} \Big|_{r=\rho} \quad (1.49)$$

$$v = \frac{d\rho}{dt} = \frac{-2D\sqrt{Dt}(2c^{\alpha\beta}\Gamma - \bar{c}r + c^{\alpha\beta}r)}{r(2c^{\alpha\beta}\Gamma + c^{\alpha\beta}r - c^{\beta\alpha}r)[-2\sqrt{Dt} + \sqrt{\pi}r \exp(r^2/4Dt)\operatorname{erfc}(r/2\sqrt{Dt})]} \quad (1.50)$$

The growth rate v should be negative for the precipitate size less than critical radius. These results are advantageous because these can be applicable not only for growth kinetics, but also for coarsening process within the same formulation.

1.6.4 Coarsening

The last process of precipitation is coarsening, in which the number of particles decreases and average size of particles increases maintaining the total precipitate volume fraction by consuming the driving force of capillarity effect. This process occurs since larger particles are more energetically favored than smaller particles. Fig. 1.15 is a schematic free energy diagram with respect to solute composition showing the principle of coarsening process. When the smaller and bigger particles exist together, the matrix concentration near the interface which is equilibrium with smaller particle is higher than bigger one due to capillarity effect. Therefore, there is concentration gradient in matrix inducing the solute atom diffusion from the smaller particles to the bigger one. As a result, smaller particles should shrink and disappear, while bigger ones are coarsened.

The earliest quantitative treatment of the coarsening process of metallic precipitates was by Greenwood and a few years later, the most widely used theory was developed independently by Lifshitz and Slyozov and Wagner (LSW theory) (Greenwood, 1956; Lifshitz & Slyozov, 1961; Wagner, 1961). In 1961, Lifshitz and Slyozov performed a mathematical for-

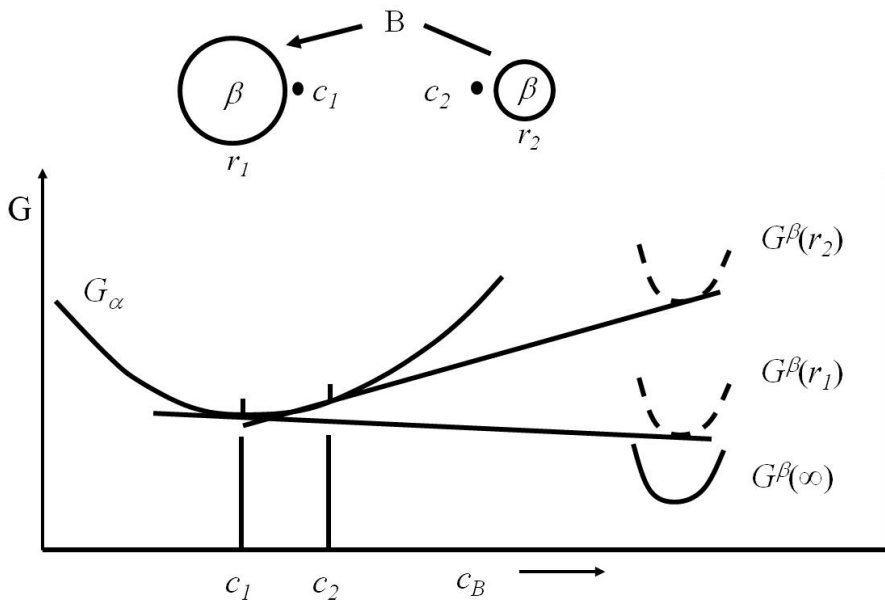


Figure 1.15: A schematic free energy and composition diagram showing the principle of precipitate coarsening (Porter & Easterling, 1992).

1.6. Precipitate

mulation of Ostwald ripening in the case where diffusion of material is the rate controlling process. The solution method they used was to define a particle radius distribution function $f(r, t)$ to which they applied the continuity equation. The distribution function obeys the continuity equation

$$\frac{\partial f}{\partial t} + \frac{\partial}{\partial r} \left(f \frac{\partial r}{\partial t} \right) = 0 \quad (1.51)$$

which has to be satisfied along with the flux balance equation and a mass balance equation. There is no source of new droplets, since nucleation has ceased. Their results are for small volume fractions of transformed phase, and can be expressed as

$$\bar{r}(t)^n - \bar{r}(0)^n = \frac{8 \sigma V_m^2 D C_e}{9 RT} t \quad (1.52)$$

where t is time, \bar{r} is the average radius of all the particles, σ is interfacial energy between particles and matrix per unit area, D is diffusion coefficient of the particle element which controls coarsening process, C_e is the equilibrium concentration of solute in the matrix in the units of mol m^{-3} and V_m is the molar volume of the particle (Wagner, 1961). n is a constant determined by the coarsening mechanism; $n = 2$ for interface migration coarsening, $n = 3$ for bulk diffusion, $n = 4$ for grain boundary diffusion and $n = 5$ for dislocation diffusion (Ardell, 1972; Lifshitz & Slyozov, 1961; Wagner, 1961).

The size distribution function of particles is also contained in the Lifshitz and Slyozov derivation (Lifshitz & Slyozov, 1961). For convenience, let ρ be a new variable which is the radius of particles divided by the average radius, then

$$f(\rho, t) = \frac{4}{9} \left(\frac{3}{3 + \rho} \right)^{7/3} \left(\frac{1.5}{1.5 - \rho} \right)^{11/3} \exp \left(- \frac{1.5}{1.5 - \rho} \right). \quad (1.53)$$

The time independent distribution function $f(\rho)$ is calculable and is

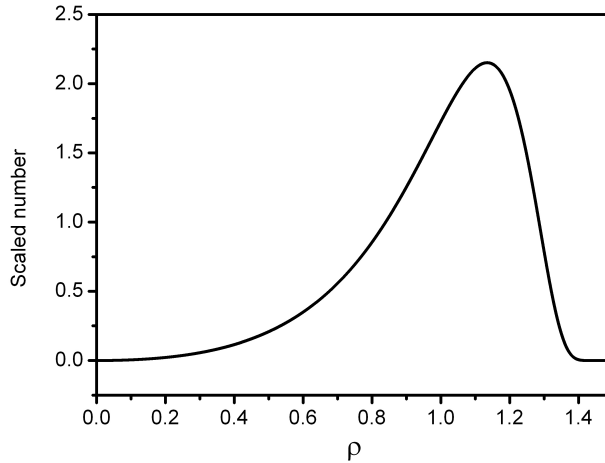


Figure 1.16: Particle size distributions predicted by the mean-field theory of the LSW model.

shown in Fig. 1.16. The LSW theory predicts that after long times the distribution of particle size, properly scaled, should reach a universal form that is independent of all material parameters.

References

- AARONSON, H., LEE, J. & RUSSELL, K. (1978). Precipitation processes in solids. In *Conference Proceeding of the Metallurgical Society of AIME, Warrendale, PA*, 31. [27](#)
- AKBEN, M., CHANDRA, T., PLASSIARD, P. & JONAS, J. (1984). Dynamic precipitation and solute hardening in a titanium microalloyed steel containing three levels of manganese. *Acta Metallurgica*, **32**, 591–601. [12](#)

REFERENCES

- ANDERSEN, O. (1975). Linear methods in band theory. *Physical Review B*, **12**, 3060. [24](#)
- ARDELL, A. (1972). The effect of volume fraction on particle coarsening: theoretical considerations. *Acta Metallurgica*, **20**, 61–71. [33](#)
- BATES, D., FUNDAMINSKY, A., MASSEY, H. & LEECH, J. (1950). Excitation and ionization of atoms by electron impact—the born and oppenheimer approximations. *Philosophical Transactions of the Royal Society of London. Series A. Mathematical and Physical Sciences*, 93–143. [19](#)
- BHADESHIA, H. (2003). Advances in the kinetic theory of carbide precipitation. In *Materials Science Forum*, vol. 426, 35–42, Trans Tech Publ. [30](#)
- BHADESHIA, H. & HONEYCOMBE, R. (2006). *Steels: microstructure and properties*. Butterworth-Heinemann. [9](#)
- BLÜGEL, S. & BIHLMAYER, G. (2006). Computational nanoscience: Do it yourself. *Forschungszentrum Jülich GmbH*, 85–129. [23](#)
- CHARLEUX, M., POOLE, W., MILITZER, M. & DESCHAMPS, A. (2001). Precipitation behavior and its effect on strengthening of an HSLA-Nb/Ti steel. *Metallurgical and Materials Transactions A*, **32**, 1635–1647. [7](#)
- CHRISTENSEN, M., DUDIY, S. & WAHNSTRÖM, G. (2002). First-principles simulations of metal-ceramic interface adhesion: Co/WC versus Co/TiC. *Physical Review B*, **65**, 045408. [9](#)
- CHRISTIAN, J. (2002). *The Theory of Transformations in Metals and Alloys: Part I+ II.* Elsevier. [26](#), [27](#), [28](#)
- DAVENPORT, A. & HONEYCOMBE, R. (1971). Precipitation of carbides at austenite/ferrite boundaries in alloy steels. In *Proc. Roy. Soc. London*, vol. 322, 191–205. [16](#), [17](#)

REFERENCES

- DAVENPORT, A., BROSSARD, L. & MINER, R. (1975). Precipitation in microalloyed high-strength low-alloy steels. *J. Met.*, **27**, 21–26. [9](#)
- ENOMOTO, M. (1998). Nucleation of phase transformations at intragranular inclusions in steel. *Metals and Materials International*, **4**, 115–123. [9](#)
- FUNAKAWA, Y. & SETO, K. (2007). Stabilization in strength of hot-rolled sheet steel strengthened by nanometer-sized carbides. *Tetsu-to-Hagane(Journal of the Iron and Steel Institute of Japan)*, **93**, 49–56. [1](#), [2](#), [3](#), [4](#), [6](#)
- FUNAKAWA, Y., SHIOZAKI, T., TOMITA, K., YAMAMOTO, T. & MAEDA, E. (2004). Development of high strength hot-rolled sheet steel consisting of ferrite and nanometer-sized carbides. *ISIJ international*, **44**, 1945–1951. [1](#)
- GLADMAN, T., DULIEU, D. & MCIVOR, I. (1977). Structure/property relationships in high-strength micro-alloyed steels. In *Proc. Conf. on Microalloying 75, 1977, 32-55*. [3](#), [13](#)
- GREENWOOD, G. (1956). The growth of dispersed precipitates in solutions. *Acta Metallurgica*, **4**, 243–248. [31](#)
- GROSSMAN, J., MIZEL, A., CÔTÉ, M., COHEN, M. & LOUIE, S. (1999). Transition metals and their carbides and nitrides: Trends in electronic and structural properties. *Physical review B*, **60**, 6343–6347. [8](#)
- GUILLERMET, A., HÄGLUND, J. & GRIMVALL, G. (1993). Cohesive properties and electronic structure of 5d-transition-metal carbides and nitrides in the NaCl structure. *Physical Review B*, **48**, 11673. [8](#)
- HAMANN, D. (1979). Semiconductor charge densities with hard-core and soft-core pseudopotentials. *Physical Review Letters*, **42**, 662–665. [24](#)

REFERENCES

- HARTFORD, J. (2000). Interface energy and electron structure for Fe/VN. *Physical Review B*, **61**, 2221. [9](#)
- HEDIN, L. & LUNDQVIST, B. (1971). Explicit local exchange-correlation potentials. *Journal of Physics C: Solid state physics*, **4**, 2064. [22](#)
- HOHENBERG, P. & KOHN, W. (1964). Inhomogeneous electron gas. *Physical Review*, **136**, B864. [20](#)
- HONEYCOMBE, R. & MEHL, R. (1976). Transformation from austenite in alloy steels. *Metallurgical Transactions A*, **7**, 915–936. [14](#)
- HONG, S., JUN, H., KANG, K. & PARK, C. (2003). Evolution of precipitates in the Nb–Ti–V microalloyed HSLA steels during reheating. *Scripta materialia*, **48**, 1201–1206. [1](#)
- HOWELL, P., RICKS, R. & HONEYCOMBE, R. (1980). The observation of interphase precipitation in association with the lateral growth of widmanstätten ferrite. *Journal of Materials Science*, **15**, 376–380. [14](#)
- ISAEV, E., SIMAK, S., ABRIKOSOV, I., AHUJA, R., VEKILOV, Y., KATSNELSON, M., LICHTENSTEIN, A., JOHANSSON, B. *et al.* (2007). Phonon related properties of transition metals, their carbides, and nitrides: A first-principles study. *Journal of applied physics*, **101**, 123519–123519. [8](#)
- JOST, R. & PAIS, A. (1951). On the scattering of a particle by a static potential. *Physical Review*, **82**, 840. [19](#)
- JUN, H., KANG, K. & PARK, C. (2003). Effects of cooling rate and isothermal holding on the precipitation behavior during continuous casting of Nb–Ti bearing HSLA steels. *Scripta materialia*, **49**, 1081–1086. [1](#)

REFERENCES

- KOELLING, D. & ARBMAN, G. (1975). Use of energy derivative of the radial solution in an augmented plane wave method: application to copper. *Journal of Physics F: Metal Physics*, **5**, 2041. [24](#)
- KOHN, W. & ROSTOKER, N. (1954). Solution of the schrödinger equation in periodic lattices with an application to metallic lithium. *Physical Review*, **94**, 1111. [19](#)
- KOHN, W., SHAM, L. & JOLLA., C.U.S.D.L. (1965). *Self-consistent equations including exchange and correlation effects*. APS. [21](#)
- LEE, S., LEE, Y., JUNG, W. & CHOI, J. (2009). Predictions on atomic structures of (Ti $1-x$, Mo x) C using combined approach of first-principles calculation and the cluster expansion method. *Metals and Materials International*, **15**, 797–801. [1](#), [6](#), [7](#), [8](#)
- LEE, W., HONG, S., PARK, C., KIM, K. & PARK, S. (2000). Influence of Mo on precipitation hardening in hot rolled HSLA steels containing Nb. *Scripta materialia*, **43**, 319–324. [9](#)
- LI, P. & TODD, J. (1988). Application of a new model to the interphase precipitation reaction in vanadium steels. *Metallurgical and Materials Transactions A*, **19**, 2139–2151. [16](#), [18](#)
- LIFSHTIZ, I. & SLYOZOV, V. (1961). The kinetics of precipitation from supersaturated solid solutions. *Journal of Physics and Chemistry of Solids*, **19**, 35–50. [31](#), [33](#)
- LIPATNIKOV, V., LENGAUER, W., ETTMAYER, P., KEIL, E., GROBOTH, G. & KNY, E. (1997). Effects of vacancy ordering on structure and properties of vanadium carbide. *Journal of Alloys and Compounds*, **261**, 192–197. [7](#), [8](#)

REFERENCES

- MIZUNO, M., TANAKA, I. & ADACHI, H. (1998). Chemical bonding at the Fe/TiX (X= C, N or O) interfaces. *Acta Materialia*, **46**, 1637–1645. [9](#)
- NARTOWSKI, A., PARKIN, I., MACKENZIE, M., CRAVEN, A. & MACLEOD, I. (1999). Solid state metathesis routes to transition metal carbides. *J. Mater. Chem.*, **9**, 1275–1281. [8](#)
- PERDEW, J., BURKE, K., WANG, Y. *et al.* (1996). Generalized gradient approximation for the exchange-correlation hole of a many-electron system. *Physical Review-Section B-Condensed Matter*, **54**, 16533–16539. [22](#)
- PORTER, D. & EASTERLING, K. (1992). *Phase transformations in metals and alloys*. CRC. [32](#)
- PRICE, D., COOPER, B. & WILLS, J. (1992). Full-potential linear-muffin-tin-orbital study of brittle fracture in titanium carbide. *Physical Review B*, **46**, 11368. [8](#)
- RAJU, S., MOHANDAS, E., TERRANCE, A. & RAGHUNATHAN, V. (1992). Structural systematics of cubic binary carbides and nitrides. *Materials Letters*, **15**, 56–67. [8](#)
- RICKS, R. & HOWELL, P. (1983). The formation of discrete precipitate dispersions on mobile interphase boundaries in iron-base alloys. *Acta Metallurgica*, **31**, 853–861. [14](#), [16](#)
- RICKS, R., HOWELL, P. & BARRITTE, G. (1982). The nature of acicular ferrite in HSLA steel weld metals. *Journal of Materials Science*, **17**, 732–740. [14](#)
- RIVERA-DÍAZ-DEL-CASTILLO, P. & BHADESHIA, H. (2002). Theory for growth of needle-shaped particles in multicomponent systems. *Metallurgical and Materials Transactions A*, **33**, 1075–1081. [30](#)

REFERENCES

- ROBERTS, W. & SANDBERG, A. (1980). *The composition of V (C, N) as precipitated in HSLA steels microalloyed with vanadium.* [18](#)
- RODRIGUES, P., PERELOMA, E. & SANTOS, D. (2000). Mechanical properties of an HSLA bainitic steel subjected to controlled rolling with accelerated cooling. *Materials Science and Engineering: A*, **283**, 136–143. [1](#)
- SAN MARTÍN, D., VAN DIJK, N., YAGODZINSKY, Y., BRÜCK, E. & VAN DER ZWAAG, S. (2005). Contribution to the understanding of austenite stability in a 12Cr-9Ni-4Mo maraging steel. In *Materials Science Forum*, vol. 500, 339–346, Trans Tech Publ. [28](#)
- SANTOS, D., RODRIGUES, P. & COTA, A. (2003). Modeling of mechanical behaviour of HSLA low carbon bainitic steel thermomechanically processed. In *Journal de Physique IV (Proceedings)*, vol. 112, 449–452. [1](#)
- SCHICK, H. (1966). Thermodynamics of certain refractory compounds. *V 1, 1966, 632 P. ACADEMIC PRESS, 111 FIFTH AVENUE, NEW YORK, N. Y., 10003.* [11](#)
- SETO, K., FUNAKAWA, Y. & KANEKO, S. (2007). Hot rolled high strength steels for suspension and chassis parts ‘NANO HITEN’ and ‘BHT Steel’. *JFE Technical Report*, 19–25. [2](#), [5](#), [6](#)
- SHAM, L. & KOHN, W. (1966). One-particle properties of an inhomogeneous interacting electron gas. *Physical Review*, **145**, 561. [21](#)
- SINGH, D. & KLEIN, B. (1992). Electronic structure, lattice stability, and superconductivity of CrC. *Physical Review B*, **46**, 14969. [8](#)
- SLATER, J. (1937). Wave functions in a periodic potential. *Physical Review*, **51**, 846. [24](#)

REFERENCES

- SMITH, R. & DUNNE, D. (1988). Structural aspects of alloy carbonitride precipitation in microalloyed steels. In *Materials forum*, vol. 11, 166–181, Institute of Metals and Materials Australasia. [14](#)
- SPRINGBORG, M. (1997). *Density-functional methods in chemistry and materials science*. Wiley Chichester. [20](#)
- TAYLOR, K. (1995). Solubility products for titanium-, vanadium-, and niobium-carbide in ferrite. *Scripta Metallurgica et Materialia;(United States)*, **32**. [12](#)
- TERESIAK, A. & KUBSCH, H. (1995). X-ray investigations of high energy ball milled transition metal carbides. *Nanostructured Materials*, **6**, 671–674. [7](#), [8](#), [10](#)
- WAGNER, C. (1961). Theory of precipitate change by redissolution. *Electrochimie*, **65**, 581–591. [31](#), [33](#)
- WANG, T., KAO, F., WANG, S., YANG, J., HUANG, C. & CHEN, H. (2011). Isothermal treatment influence on nanometer-size carbide precipitation of titanium-bearing low carbon steel. *Materials Letters*, **65**, 396–399. [1](#), [2](#), [6](#)
- WILLENS, R., BUEHLER, E. & MATTHIAS, B. (1967). Superconductivity of the transition-metal carbides. *Physical Review*, **159**, 327. [7](#), [8](#)
- WIMMER, E., KRAKAUER, H., WEINERT, M. & FREEMAN, A. (1981). Full-potential self-consistent linearized-augmented-plane-wave method for calculating the electronic structure of molecules and surfaces: O₂ molecule. *Physical Review B*, **24**, 864. [24](#)
- YEN, H., HUANG, C. & YANG, J. (2009). Characterization of interphase-precipitated nanometer-sized carbides in a Ti–Mo-bearing steel. *Scripta Materialia*, **61**, 616–619. [2](#)

REFERENCES

- YEN, H., CHEN, P., HUANG, C. & YANG, J. (2011). Interphase precipitation of nanometer-sized carbides in a titanium-molybdenum-bearing low-carbon steel. *Acta Materialia*. **1**, **6**, **15**
- ZENER, C. (1949). Theory of growth of spherical precipitates from solid solution. *Journal of Applied Physics*, **20**, 950–953. **28**, **30**

Chapter 2

Interphase Precipitation

The use of carbides in micro-alloyed steels is an efficient way of strengthening steels. In most cases, the carbides are controlled to precipitate randomly in ferrite after the austenite-ferrite transformation. However, alloy carbides can be formed at ferrite-austenite phase interfaces during the transformation, so-called interphase precipitation, which is of considerable importance in the field of high-strength low-alloy (HSLA) steels. The most important of elements for interphase precipitation are vanadium, titanium, niobium, chromium, molybdenum and tungsten, which have a strong affinity for carbon and are commonly known as carbide formers. These carbides can contribute to the high strengthening effect, because interphase precipitation can occur in a short time. In this chapter, the heat-treatment condition for the formation of interphase precipitation has been confirmed for Ti-Nb bearing steels and Ti-Nb-Mo bearing steels. Mechanical characterisation, transmission electron microscopy and chemical extraction have been conducted to analyze the precipitation kinetics of titanium, niobium and molybdenum containing carbides.

2.1. Sample Preparation

Table 2.1: Chemical composition of Ti-Nb and Ti-Nb-Mo steels examined in the present study (in wt%)

	C	Mn	Al	Ti	Mo	Nb
Ti-Nb	0.07	1.5	0.03	0.1	-	0.03
Ti-Nb-Mo	0.07	1.5	0.03	0.1	0.2	0.03

2.1 Sample Preparation

The chemical compositions of the alloys investigated are presented in Table 2.1. Based on the Ti-Nb steels with 1.5Mn-0.03Al-0.07C-0.1Ti-0.03Nb wt% composition, Ti-Nb-Mo steels with 1.5Mn-0.03Al-0.07C-0.1Ti-0.03Nb-0.2Mo wt% are designed to check the effects of molybdenum. The alloys were prepared as 30 kg ingots by vacuum induction melting, then hot rolled into 20 mm plates.

Figs 2.1 and 2.2 represent calculated phase fractions as a function of temperature, including the phases ferrite, austenite, cementite and B1 structure carbides in system of Ti-Nb and Ti-Nb-Mo steels, respectively, using *ThermoCalc* with the *TCFE6.2* database. It is necessary to hold the steel above 1250°C to resolve carbides. The highest equilibrium temperatures between austenite and ferrite phase are 840°C and 845°C for Ti-Nb and Ti-Nb-Mo steels, respectively, above which ferrite is not stable. This shows that about 0.2 wt% of molybdenum addition increases the equilibrium transformation start temperature from austenite to ferrite by about 5°C.

Cylindrical specimens with a diameter of 3 mm and a length of 10 mm were machined and subjected to the heat treatment using a quench dilatometer. The specimens were heated to 1100°C to obtain a fully austenitic structure, followed by slow cooling to ambient temperature with a cooling rate of 0.5°C s⁻¹. Fig. 2.3 contains cooling dilatation curves of a Ti-Nb and Ti-Nb-Mo steels showing continuous cooling transformation

2.1. Sample Preparation

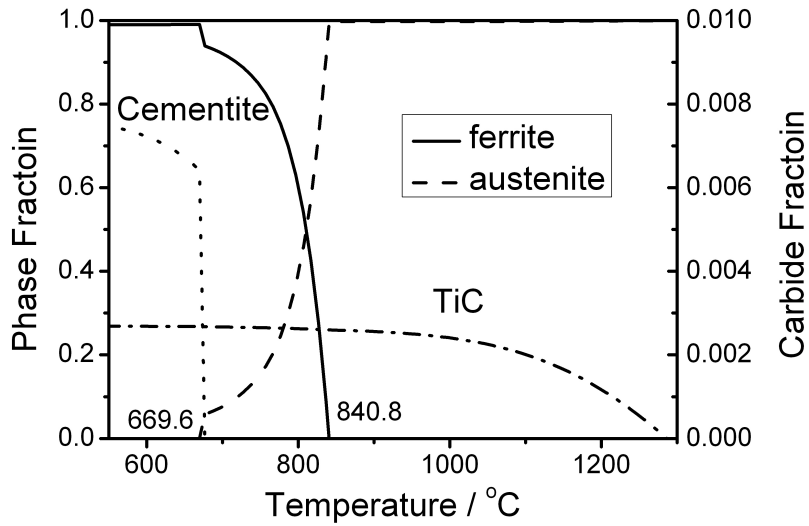


Figure 2.1: Calculated phase fraction of ferrite, austenite, cementite and titanium carbide in system Ti-Nb steel using *ThermoCalc* with *TCFE6.2* database. Ferrite and austenite phase correspond to the scale of left bar. Cementite and TiC phase correspond to right bar.

2.1. Sample Preparation

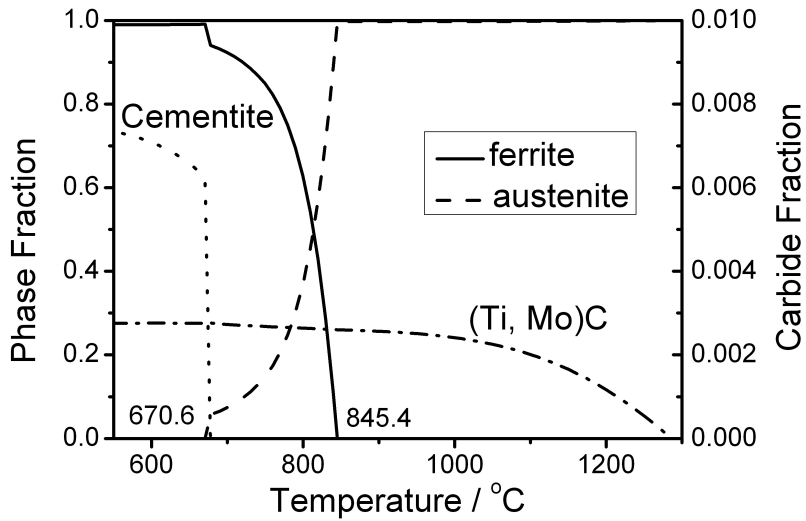


Figure 2.2: Calculated phase fraction of ferrite, austenite, cementite and titanium carbide in system Ti-Nb-Mo steel using *ThermoCalc* with *TCFE6.2* database. Ferrite and austenite phase correspond to the scale of left bar. Cementite and TiC phase correspond to right bar.

2.1. Sample Preparation

from austenite to ferrite. The ferrite transformation start temperature from austenite estimated as 742°C and 728°C for Ti-Nb and Ti-Nb-Mo steels, respectively, by using the offset method with 1 vol.% offset (Yang & Bhadeshia, 2007). The transformation start temperature for Ti-Nb-Mo steels is about 14°C lower than that of Ti-Nb steels, due to slow transformation rates of Ti-Nb-Mo steels.

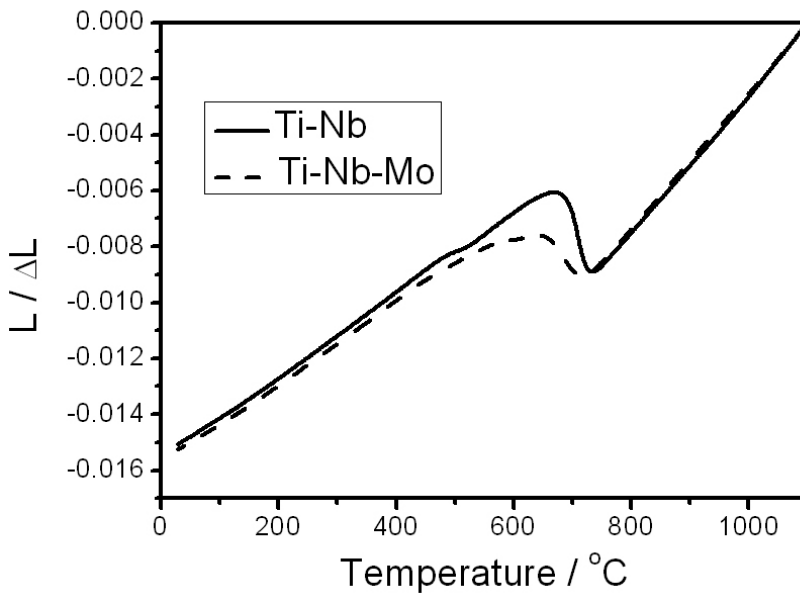


Figure 2.3: Cooling dilatation curves of a Ti-Nb and Ti-Nb-Mo steels obtained at a cooling rate of $0.5^{\circ}\text{C s}^{-1}$.

Based on the thermodynamic calculation results and dilatometric curves, new heat treatments were designed to stimulate interphase precipitation and confirm the role of molybdenum on coarsening phenomena. Cylindrical specimens with a diameter of 8 mm and a length of 12 mm were prepared and subjected to the heat treatment cycle in Fig. 2.4 by using *THERMOMASTER-Z* thermo-mechanical simulator.

2.1. Sample Preparation

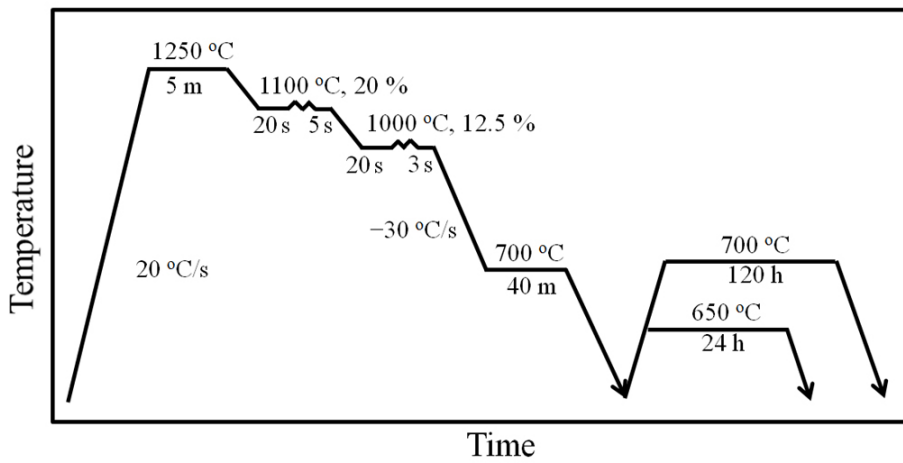


Figure 2.4: Schematic diagram showing the two-step heat treatment. The first heating temperature, 1250°C, is determined to resolve TiC precipitation and the isothermal holding temperature, 700°C, is determined to obtain ferrite from austenite. Prolonged ageing time and temperatures are designed to check the effect of the coarsening process.

2.1. Sample Preparation

The specimens were heated to 1250°C for 300 s to dissolve pre-existing precipitation in vacuum atmosphere. After that, the specimen were cooled to the deformation temperature 1100°C and 1000°C at the cooling rate of 30°C s⁻¹, and hot compression was carried out at a strain rate of 1 s⁻¹ for the total strain of 0.3 to control the austenite grain size. After the hot deformation, the specimens were cooled to an isothermal holding temperature, 700°C. They were then cooled to room temperature after 40 min holding. Two more prolonged ageing were conducted to check coarsening behavior using a box furnace. The specimens encapsulated in evacuated quartz tubes and reheated to 650°C and 700°C, and hold for 24 h and 120 h, respectively.

A cross-section along the longitudinal direction of the specimen was observed using a light microscope with 2% nital solution. The detailed microstructure of (Ti,Nb)C and (Ti,Nb,Mo)C precipitates were analyzed by transmission electron microscope (TEM) and scanning TEM (STEM), together with energy-dispersive X-ray spectroscopy (EDS). The equipment used was a field-emission-gun TEM, *JEOL JEM 2100F*, operated at 200 kV, in which the relative rotation of the image with the pattern are corrected. The ferrite fraction in the corresponding optical samples and precipitation size in TEM images were measured using graphic software, *Image Pro Plus*. The chemical composition of each carbides are characterized using EDS in thin foil samples or carbon extraction replica allowing Ti, Nb and Mo elements. It is assumed that there is no overlap of information from the matrix in thin foil samples since the compositions of Ti, Nb and Mo in matrix are extremely small.

Thin foil samples were produced by cutting slices from the specimens, thinning mechanically to 0.08 mm by abrasion on SiC papers, and then twin-jet electro-polishing using a mixture of 5% perchloric acid and 95% ethanol at 18°C with a current of 60~70 mA. Carbon extraction replicas were also prepared. A layer of carbon was deposited on the etched specimen, which was then cut as 1.5 mm grid size. Then specimens were

electro-polished using a mixture of 10% perchloric acid and 90% ethanol at room temperature with 0.015 mA current until the replicas began to lift. The specimen was slid into distilled water, and the replicas were collected by a copper net.

2.2 Ti-Nb Steel

Fig. 2.5 presents optical micrographs of Ti-Nb steels after isothermal holding at 700°C for 40 min, prolonged ageing at 650°C for 24 h and at 700°C for 120 h, respectively. The white-etched phase is allotriomorphic ferrite, which nucleated and grew during isothermal transformation at 700°C. The dark etched phase is martensite, which originated from the rapid cooling of untransformed austenite. The ferrite volume fraction and grain size are measured using the image analyzing software, *Image Pro*. The ferrite volume fraction is measured at about 0.72 ± 0.05 for all the samples. The measured ferrite grain size was about $25 \pm 5 \mu\text{m}$, and there is no significant difference in this size over the three samples.

2.2.1 Isothermal Holding at 700°C for 40 min

Fig. 2.6 presents bright field TEM images of Ti-Nb steels after isothermal holding at 700°C for 40 min showing carbides. Fig. 2.7 includes dark field images showing carbides as rows and its corresponding diffraction pattern with $[012]$ zone axis of ferrite. The dark field image are obtained using a diffraction pattern within the blank circle. The additional diffraction patterns without indexing come from the other precipitate with different orientation relationship. The images show curved interface interphase precipitation with irregular spacing with average distance as about 43 nm. The precipitates rows are perpendicular to the $[0\bar{2}1]$ ferrite direction between $[\bar{1}\bar{2}1]$ and $[\bar{1}2\bar{1}]$. Fig. 2.8 indicates the results of characteristic EDS spectra of the (Ti,Nb)C carbides with about 5 nm size carbide in Fig. 2.7 from thin foil sample. It is estimated to contain

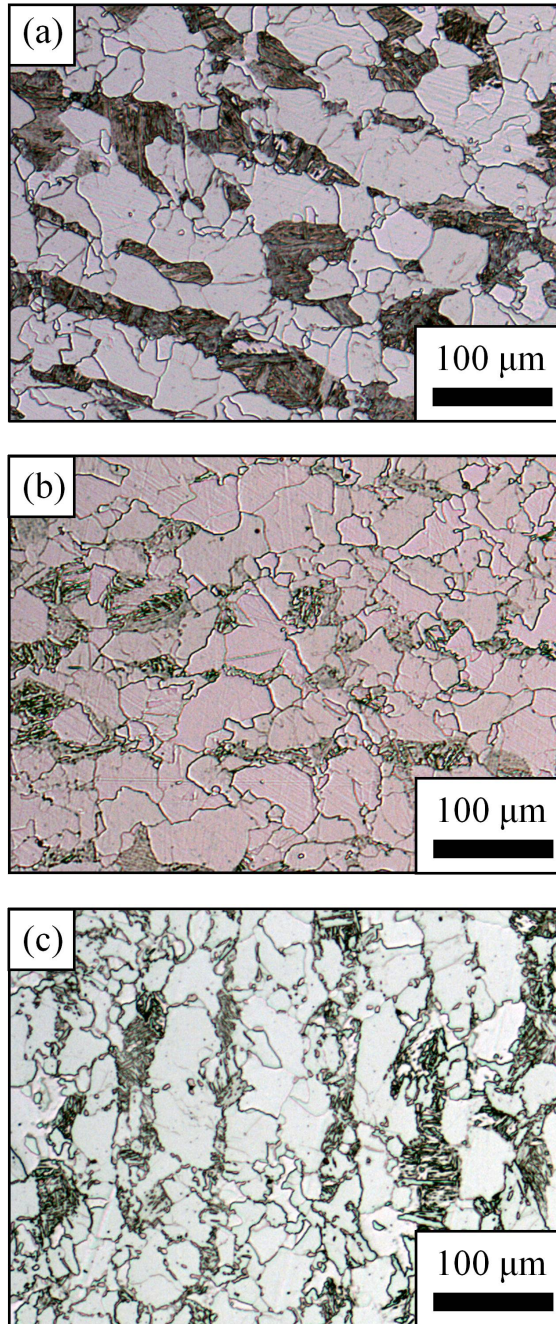


Figure 2.5: Optical micrographs showing ferrite fraction and grain size of Ti-Nb steels after (a) isothermal holding at 700°C for 40 min, (b) prolonged ageing at 650°C for 24 h and (c) at 700°C for 120 h.

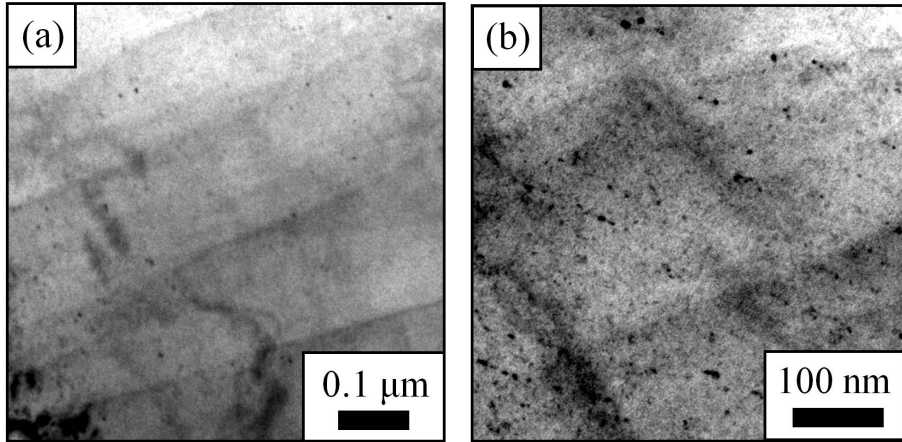


Figure 2.6: Transmission electron micrograph of Ti-Nb steel after isothermal holding at 700°C for 40 min bright field images with (a) low magnification and (b) high magnification showing carbides.

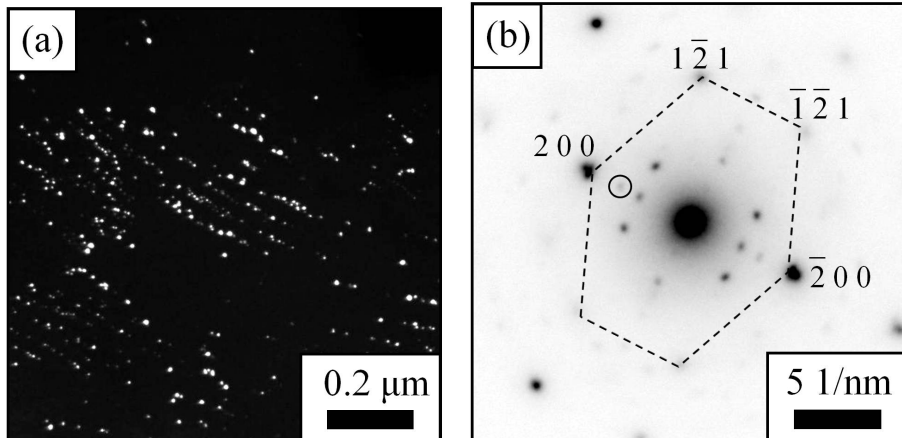


Figure 2.7: Transmission electron micrograph of Ti-Nb steel after isothermal holding at 700°C for 40 min. (a) Dark field image and (b) corresponding diffraction pattern with $[012]$ zone axis of ferrite.

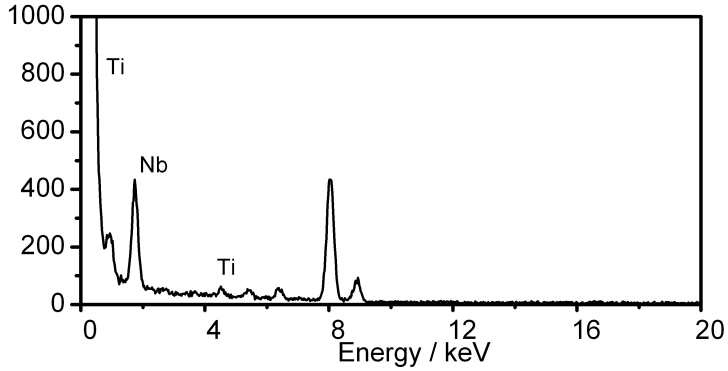


Figure 2.8: Characteristic EDS spectra of the (Ti,Nb)C carbides with about 5 nm size in the Ti-Nb steel after isothermal holding at 700°C for 40 min from thin foil sample. It is estimated to contain 57(72 at%)±11 wt% Ti and 42(27 at%)± 11 wt% Nb, respectively.

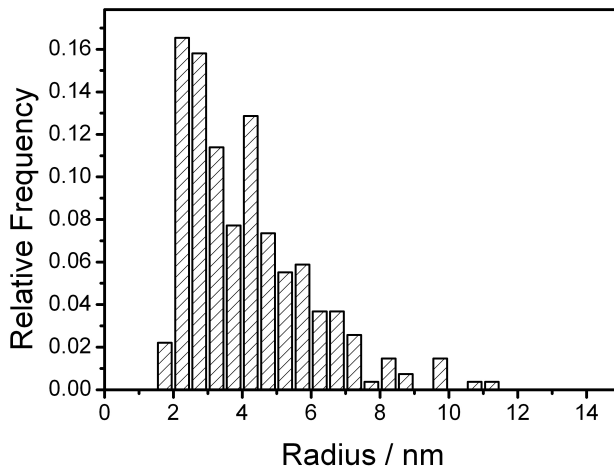


Figure 2.9: Relative frequency as a function of particle radius of (Ti,Nb)C particles in Ti-Nb steel after isothermal holding at 700°C for 40 min. The mean value and standard deviation of radius are 4.13 nm and 1.81 nm, respectively.

57(72 at%) \pm 11 wt% Ti and 42(27 at%) \pm 11 wt% Nb, respectively, which contains much higher niobium concentration than average concentration. Fig. 2.9 shows the distribution of particle radii for (Ti,Nb)C particles, as obtained from dark field images. The radius is estimated by the maximum distance from the cent of each particle. The measured mean value and standard deviation of particle radius are 4.13 nm and 1.81 nm, respectively.

2.2.2 Prolonged Aging at 650°C for 24 h

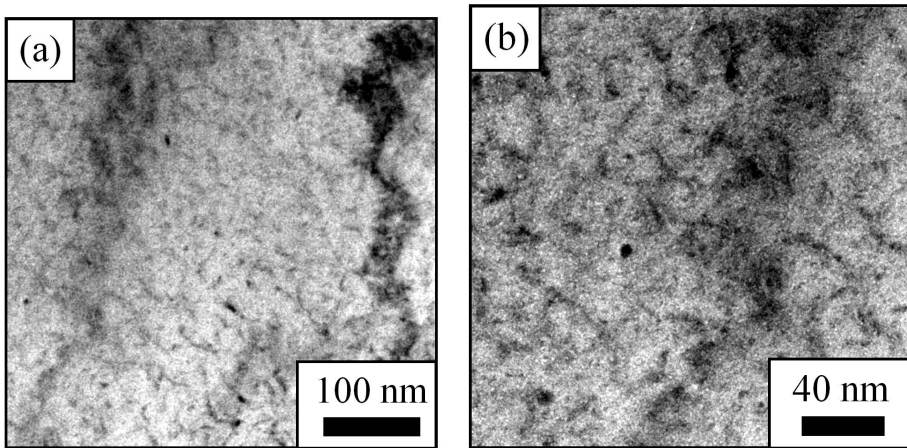


Figure 2.10: Bright field TEM images of Ti-Nb steel after prolonged aging at 650°C for 24 h with (a) lower and (b) higher magnification showing carbides.

Fig. 2.10 shows bright field TEM images of Ti-Nb steel after prolonged aging at 650°C for 24 h showing carbides. Fig. 2.11 includes dark field images showing carbides with curved interface interphase precipitation with irregular spacing. The measured average spacing between precipitates is about 41 nm. Fig. 2.12 indicates the results of characteristic EDS spectra of the (Ti,Nb)C carbides with about 6 nm size carbide contained in Fig. 2.11 from thin foil sample. It is estimated to contain

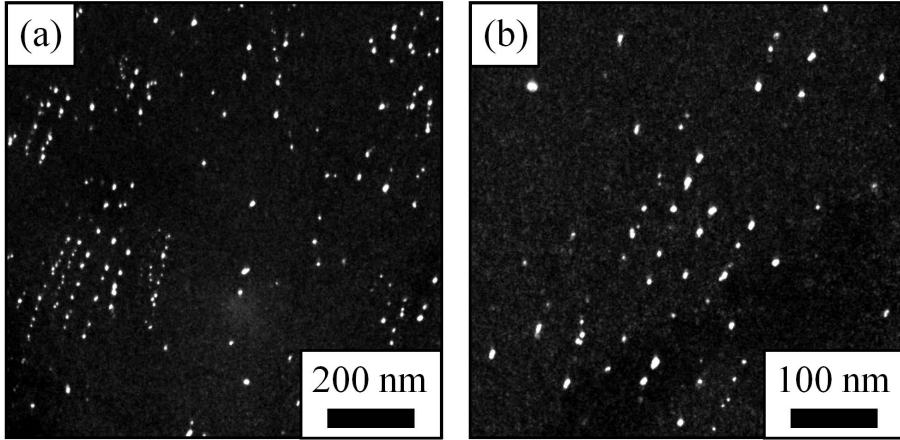


Figure 2.11: Dark field TEM images of Ti-Nb steel after prolonged aging at 650°C for 24 h with (a) lower and (b) higher magnification showing carbides.

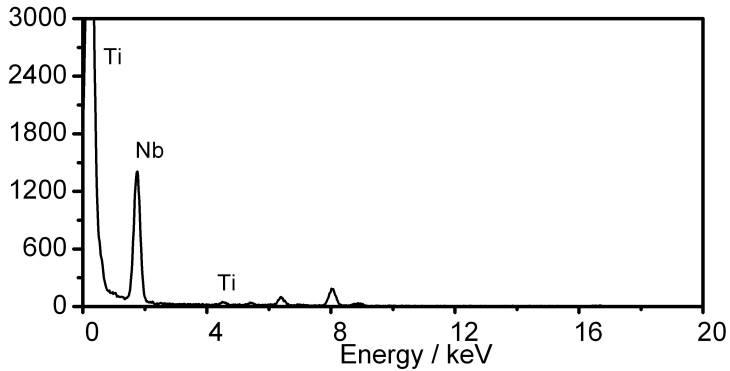


Figure 2.12: Characteristic EDS spectra of the (Ti,Nb)C carbides with about 6 nm size in the Ti-Nb steel after prolonged ageing at 650°C for 24 h from thin foil sample. It is estimated to contain 61(75 at%) \pm 9 wt% Ti and 39(25 at%) \pm 9 wt% Nb, respectively.

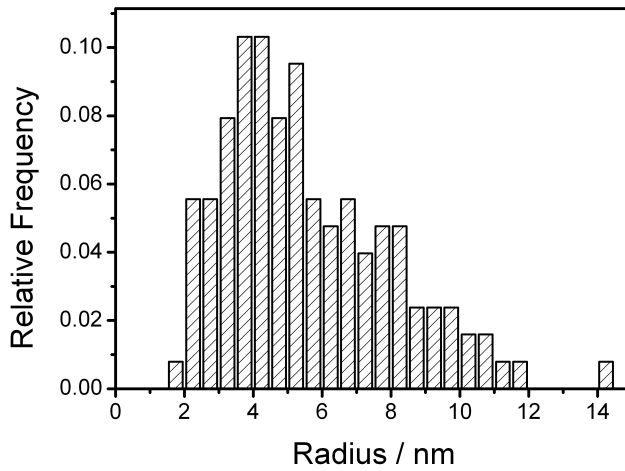


Figure 2.13: Relative frequency as a function of particle radius of (Ti,Nb)C particles in Ti-Nb steel after prolonged ageing at 650°C for 24 h. The mean value and standard deviation of radius are 5.74 nm and 2.84 nm, respectively.

61(75 at%) \pm 9 wt% Ti and 39(25 at%) \pm 9 wt% Nb, respectively. Fig. 2.13 shows relative frequency dependency on radius of (Ti,Nb)C particles obtained from dark field images. The measured mean value and standard deviation of radius are 5.74 nm and 2.84 nm, respectively.

2.2.3 Prolonged Aging at 700°C for 120 h

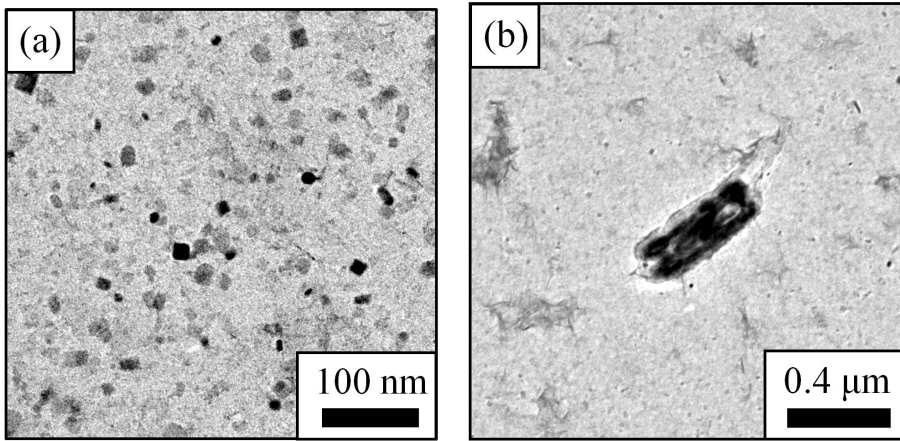


Figure 2.14: Bright field TEM images of Ti-Nb steel after prolonged aging at 700°C for 120 h showing the distribution of (a) small and (b) big (Ti,Nb)C carbides.

Fig. 2.14 presents carbon extraction replicas of Ti-Nb steel after prolonged aging at 700°C for 120 h showing the distribution of small and big (Ti,Nb)C carbides. They contain two different size scale carbides with less than 10 nm radius and bigger than 0.1 μm. Fig. 2.15 indicates the results of characteristic EDS spectra of the (Ti,Nb)C carbides with about 8 nm size carbide contained in Fig. 2.14 from carbon extraction replicas. It is estimated to contain 56(71 at%) \pm 4 wt% Ti and 44(29 at%) \pm 4 wt% Nb, respectively. There is no significant difference of titanium and niobium compositions among samples at the different heat-treatment. Fig. 2.16 shows relative frequency dependency on radius of (Ti,Nb)C particles ob-

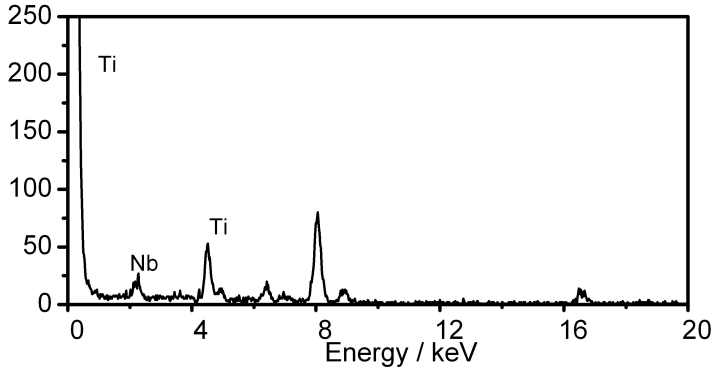


Figure 2.15: Characteristic EDS spectra of the (Ti,Nb)C carbides with about 8 nm size in the Ti-Nb steel after prolonged ageing at 700°C for 120 h from thin foil sample. It is estimated to contain 56(71 at%)±4 wt% Ti and 44(29 at%)±4 wt% Nb, respectively.

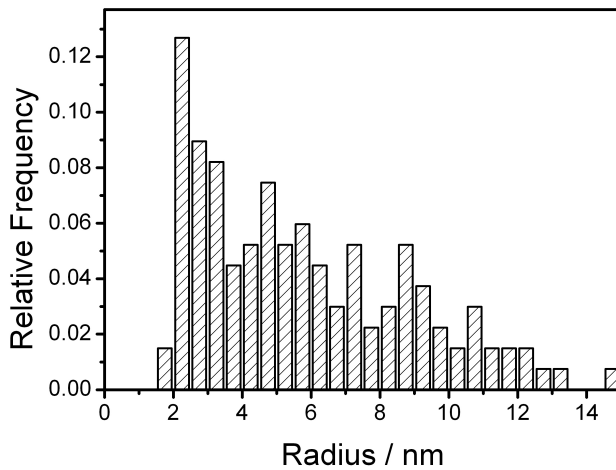


Figure 2.16: Relative frequency as a function of particle radius of (Ti,Nb)C particles in Ti-Nb steel after prolonged ageing at 700°C for 120 h. The mean value and standard deviation of radius are 7.65 nm and 4.23 nm, respectively.

tained from carbon extraction replicas. The measured mean value and standard deviation of radius are 7.65 nm and 4.23 nm, respectively.

2.3 Ti-Nb-Mo Steel

Fig. 2.17 presents optical micrographs of Ti-Nb-Mo steels after isothermal holding at 700°C for 40 min, prolonged ageing at 650°C for 24 h and at 700°C for 120 h, respectively. The white-etched phase is allotriomorphic ferrite, due to isothermal transformation at 700°C. The ferrite volume fraction is measured about 0.71 ± 0.07 for the three different heat-treatments, which is almost identical to the Ti-Nb steels.

2.3.1 Isothermal Holding at 700°C for 40 min

Fig. 2.18 presents bright field images using transmission electron microscope of Ti-Nb-Mo steels after isothermal holding at 700°C for 40 minutes showing carbides. Fig. 2.19 includes dark field image showing carbides as rows and its corresponding diffraction pattern with [012] zone axis of ferrite. The precipitation is shown to be a planar interphase precipitation with regular spacing with average distance as about 22 nm. The precipitates rows are perpendicular to the $[0\bar{2}1]$ ferrite direction between $[1\bar{2}1]$ and $[\bar{1}21]$.

Fig. 2.20 shows carbon extraction replicas of Ti-Nb-Mo steel showing the distribution. There are two different size scales carbides with less than 10 nm radius and bigger than 50 nm. Fig 2.21 indicates the results of characteristic EDS spectra of the (Ti,Nb,Mo)C carbides with about 3 nm size and 25 nm size carbide shown in Fig. 2.20. The concentration of small size particle is estimated to $38(55 \text{ at}\%) \pm 1.6 \text{ wt}\%$ Ti and $14(10 \text{ at}\%) \pm 1.7 \text{ wt}\%$ Nb and $48(34 \text{ at}\%) \pm 1.8 \text{ wt}\%$ Mo, respectively. The atomic ration Mo/Ti is about 0.617. The bigger particle contains $88(93 \text{ at}\%) \pm 2.3 \text{ wt}\%$ Ti and $8(5 \text{ at}\%) \pm 1.9 \text{ wt}\%$ Nb and $4(2 \text{ at}\%) \pm 1.8 \text{ wt}\%$ Mo, respectively, which is almost pure TiC. Fig 2.22 shows relative frequency dependency on

2.3. Ti-Nb-Mo Steel

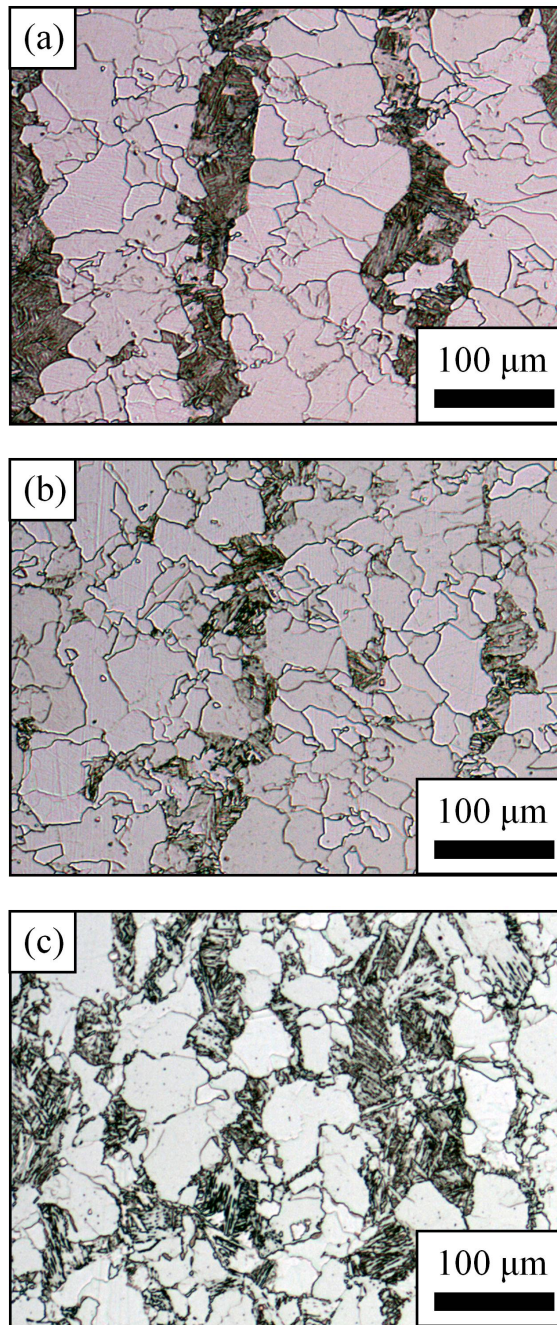


Figure 2.17: Optical micrographs showing ferrite fraction and grain size of Ti-Nb-Mo steels after (a) isothermal holding at 700°C for 40 min, (b) prolonged ageing at 650°C for 24 h⁶⁰ and (c) at 700°C for 120 h.

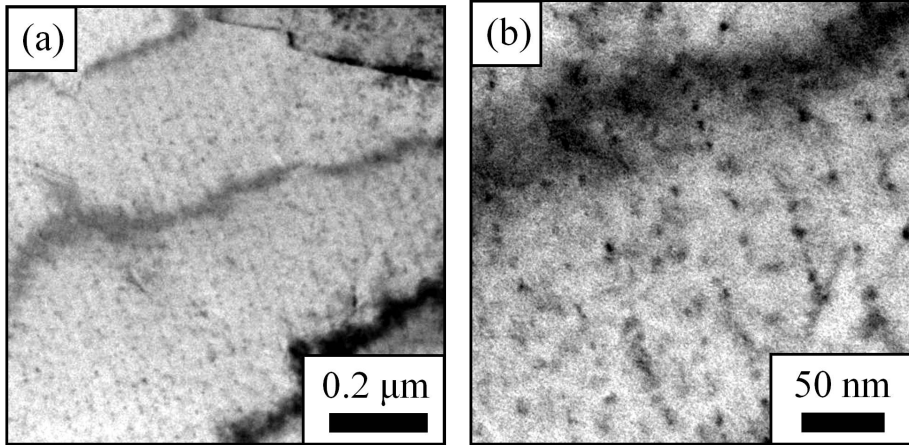


Figure 2.18: Bright field TEM images of Ti-Nb-Mo steel after isothermal holding at 700°C for 40 min with (a) lower and (b) higher magnification showing carbides.

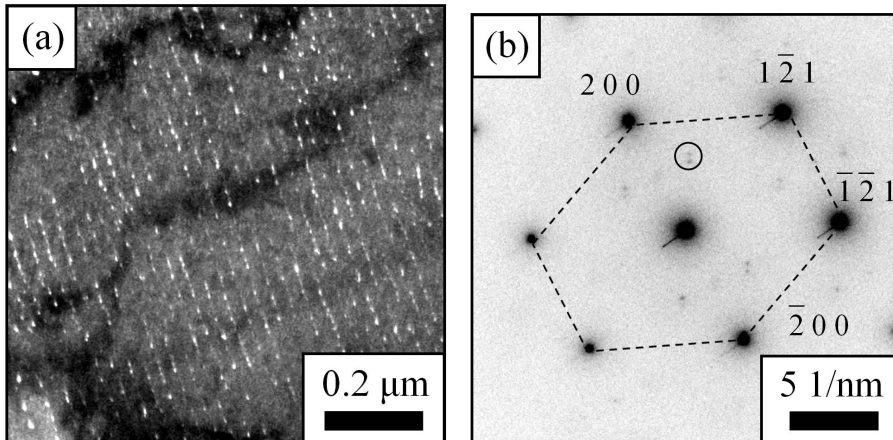


Figure 2.19: TEM images of Ti-Nb-Mo steel after isothermal holding at 700°C for 40 min . (a) Dark field image and (b) corresponding diffraction pattern with $[012]$ zone axis of ferrite.

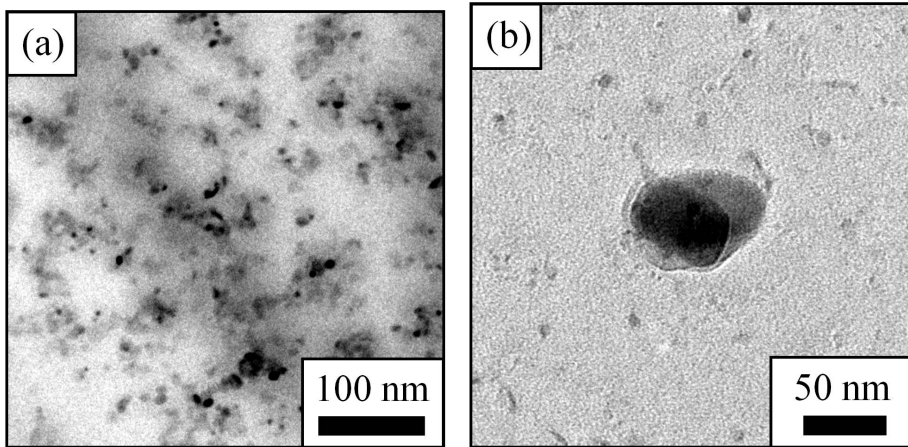


Figure 2.20: Carbon extraction replicas of Ti-Nb steel after isothermal holding at 700°C for 40 min showing the distribution of (a) small and (b) big (Ti,Nb,Mo)C.

particle radius of (Ti,Nb,Mo)C particles. The mean value and standard deviation of radius are 2.85 nm and 2.58 nm, respectively.

2.3.2 Prolonged Aging at 650°C for 24 h

Figs 2.23 and 2.24 present bright field TEM images of Ti-Nb-Mo steel after prolonged aging at 650°C for 24 h showing carbides which is obtained during interphase precipitation using with and without spherical aberration (Cs) corrected TEM, respectively. Fig 2.25 includes dark field images corresponds to the bright field image Fig. 2.24(a). The precipitation is shown to have a planar interphase precipitation with regular spacing with about 13 nm average distance.

Fig.2.26 shows carbon extraction replicas of Ti-Nb-Mo steel showing the distribution of smaller and bigger carbides. It can be observed to have two different size scale carbide with less than 10 nm radius and bigger than 50 nm. Fig 2.27 indicates the results of characteristic EDS spectra of the (Ti,Nb,Mo)C carbides with about 4 nm size and 24 nm

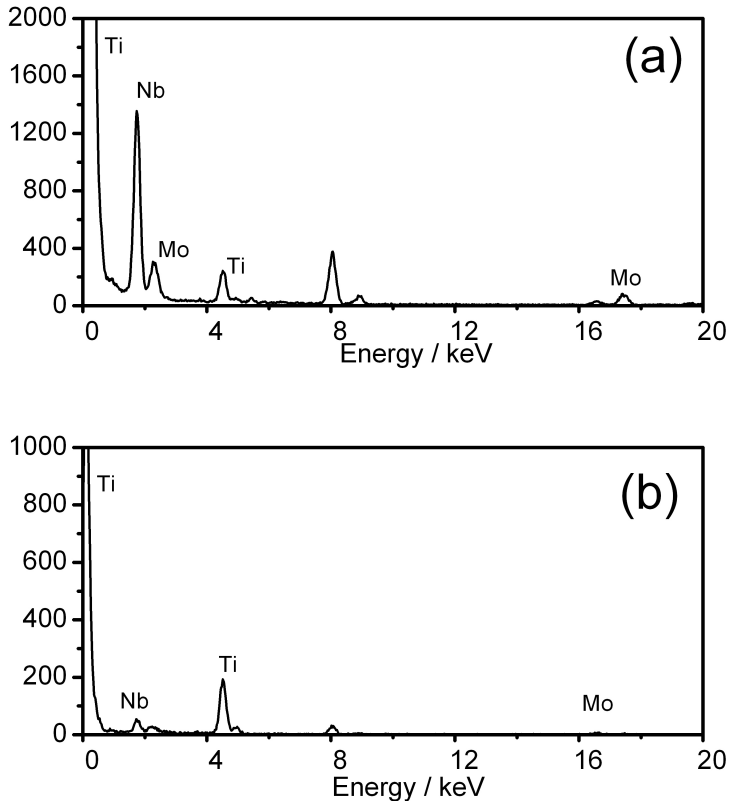


Figure 2.21: Characteristic EDS spectra of the (Ti,Nb,Mo)C carbides with about (a) 3 nm and (b) 26 nm size in the Ti-Nb-Mo steel after isothermal holding at 700°C for 40 min from thin foil sample. It is estimated to contain (a) 38(55 at%) \pm 1.6 wt% Ti and 14(10 at%) \pm 1.7 wt% Nb and 48(34 at%) \pm 1.8 wt% Mo, respectively. It is estimated to have (b) 88 wt%(93 at%) \pm 2.3 wt% Ti and 8 wt%(5 at%) \pm 1.9 wt% Nb and 4 wt%(2 at%) \pm 1.8 wt% Mo, respectively.

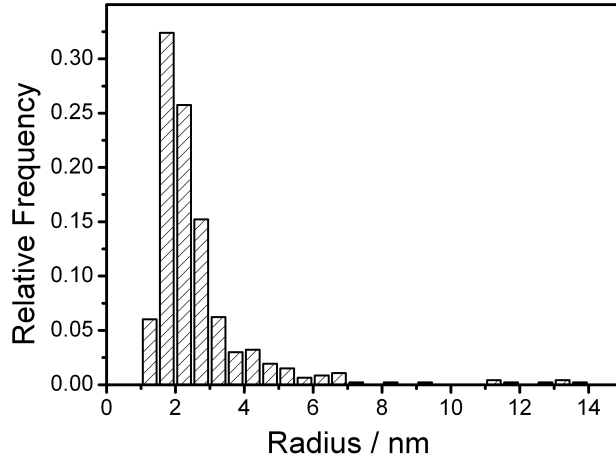


Figure 2.22: Relative frequency as a function of particle radius of (Ti,Nb,Mo)C particles in Ti-Nb-Mo steel after isothermal holding at 700°C for 40 min. The mean value and standard deviation of radius are 2.85 nm and 2.58 nm, respectively.

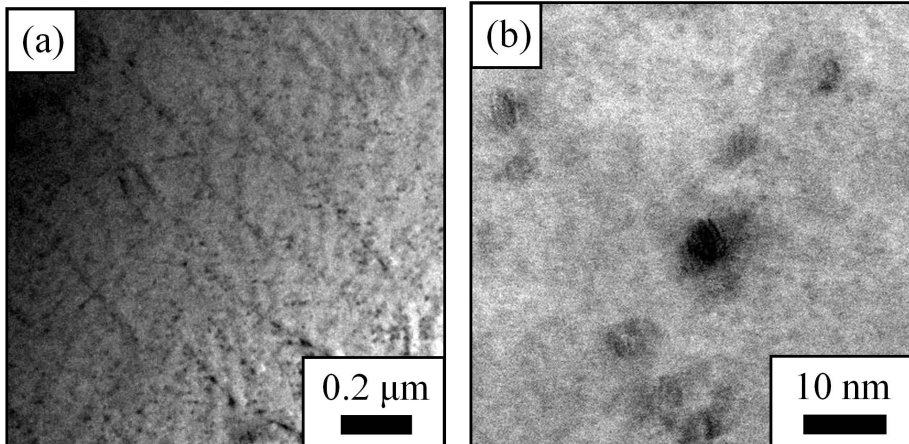


Figure 2.23: Bright field TEM images of Ti-Nb-Mo steel after prolonged aging at 650°C for 24 h with (a) lower and (b) higher magnification showing carbides.

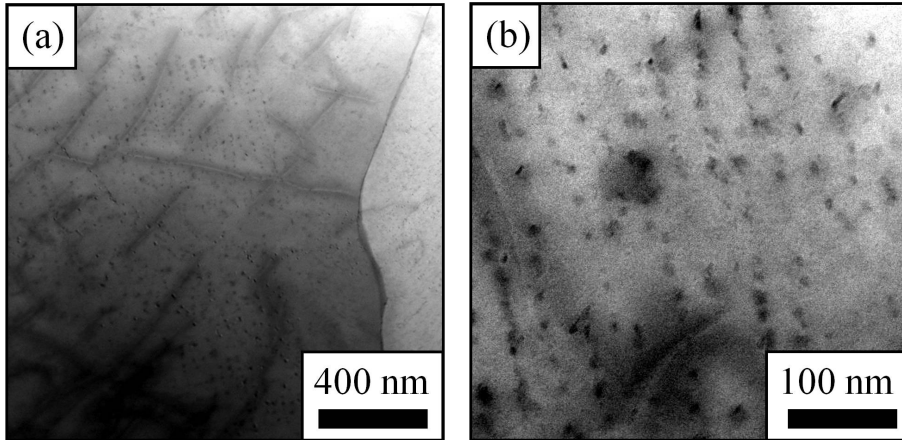


Figure 2.24: Bright field TEM images equipped with Cs corrector of Ti-Nb-Mo steel after prolonged aging at 650°C for 24 h with (a) lower and (b) higher magnification showing carbides.

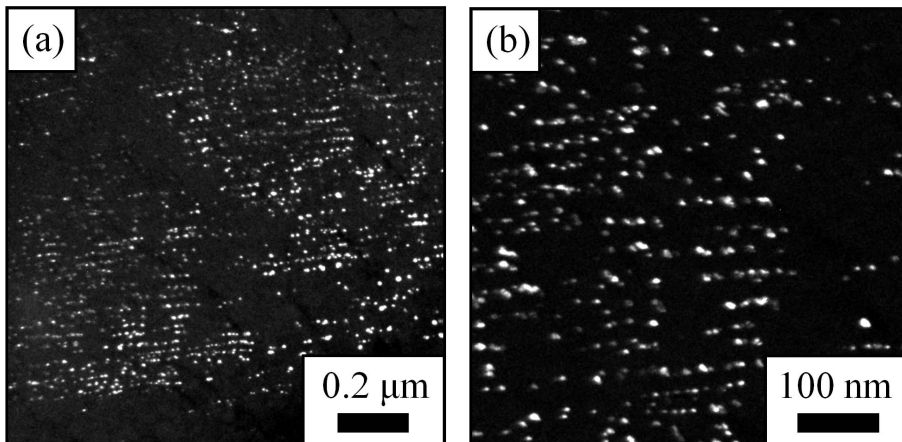


Figure 2.25: Dark field TEM images of Ti-Nb-Mo steel after prolonged aging at 650°C for 24 h with (a) lower and (b) higher magnification showing carbides.

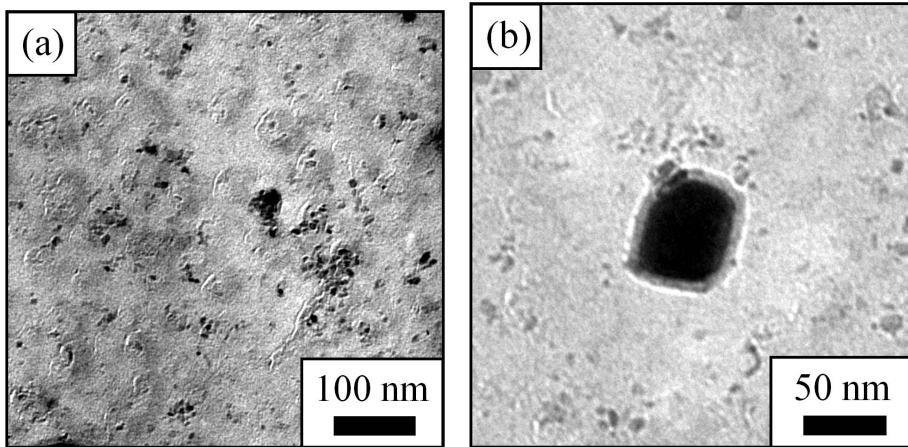


Figure 2.26: Carbon extraction replicas of Ti-Nb steel after prolonged aging at 650°C for 24 h showing the distribution of (a) small and (b) big (Ti,Nb,Mo)C.

size carbide shown in Fig. 2.26. The concentration of small particle is estimated to 25(39 at%) \pm 0.9 wt% Ti and 15(12 at%) \pm 1.4 wt% Nb and 60(48 at%) \pm 1.4 wt% Mo, respectively, which corresponds to 1.22 atomic ratio of Mo/Ti. The bigger particle contains 89(94 at%) \pm 2.5 wt% Ti and 7(4 at%) \pm 2.0 wt% Nb and 4(2 at%) \pm 1.7 wt% Mo, respectively. Fig. 2.28 shows relative frequency dependency on particle radius of (Ti,Nb,Mo)C particles in Ti-Nb-Mo steel. The mean value and standard deviation of radius are 2.84 nm and 2.82 nm, respectively.

2.3.3 Prolonged Aging at 700°C for 120 h

Fig. 2.29 presents bright field TEM images of Ti-Nb-Mo steels after prolonged aging at 700°C for 120 h showing two different size particles with less than 10 nm and bigger than 1 μ m. Fig. 2.30 shows carbon extraction replicas of Ti-Nb-Mo steel showing the distribution of smaller and bigger carbides. It can be observed to have two different size scales of carbides with less than 10 nm radius and bigger than 100 nm.

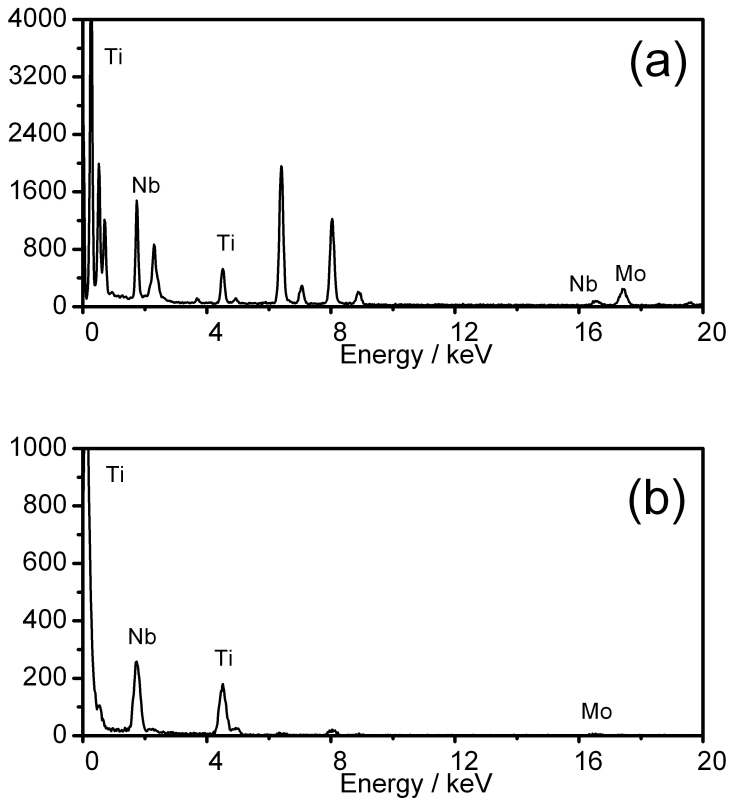


Figure 2.27: Characteristic EDS spectra of the (Ti,Nb,Mo)C carbides with about (a) 4 nm and (b) 23 nm size in the Ti-Nb-Mo steel after prolonged aging at 650°C for 24 h from carbon extraction replicas. It is estimated to contain (a) 25(39 at%) \pm 0.9 wt% Ti and 15(12 at%) \pm 1.4 wt% Nb and 60(48 at%) \pm 1.4 wt% Mo, respectively. It is estimated to have (b) 89(94 at%) \pm 2.5 wt% Ti and 7(4 at%) \pm 2.0 wt% Nb and 4(2 at%) \pm 1.7 wt% Mo, respectively.

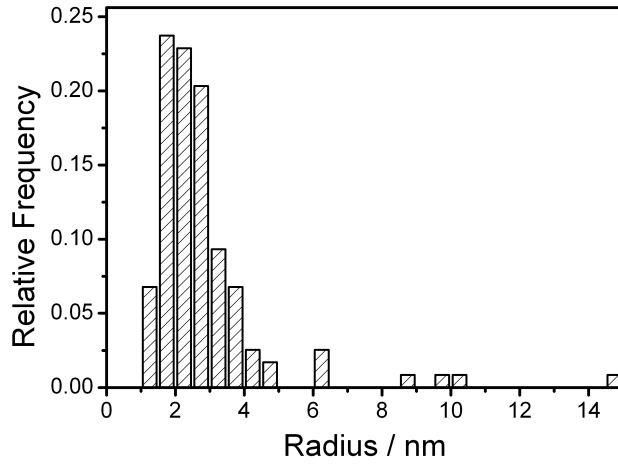


Figure 2.28: Relative frequency as a function of particle radius of (Ti,Nb,Mo)C particles in Ti-Nb-Mo steel after prolonged aging at 650°C for 24 h . The mean value and standard deviation of radius are 2.84 nm and 1.82 nm, respectively.

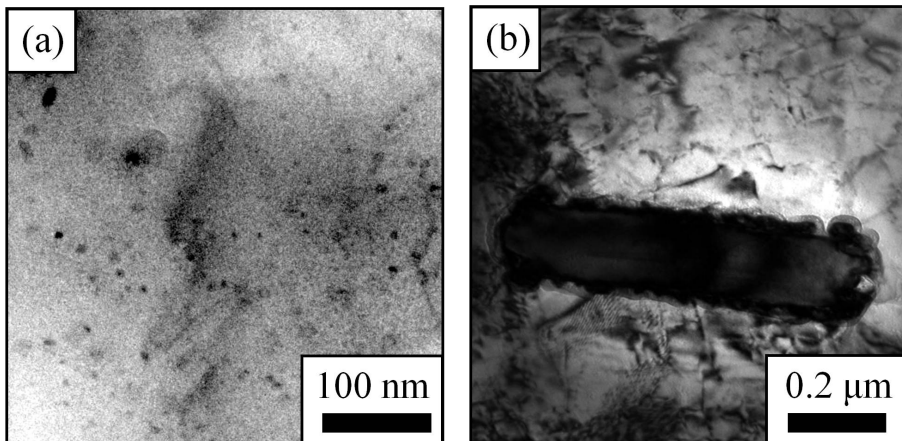


Figure 2.29: Bright field TEM images of Ti-Nb-Mo steel after prolonged aging at 700°C for 120 h with (a) small and (b) big (Ti,Nb,Mo)C carbides.

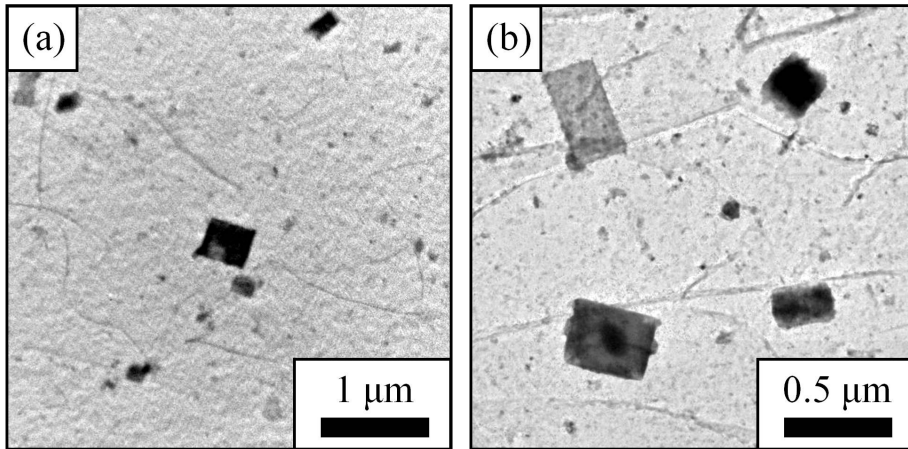


Figure 2.30: Carbon extraction replicas of Ti-Nb steel after prolonged aging at 700°C for 120 h showing the distribution with (a) lower and (b) higher magnification

Fig. 2.31 indicates the results of characteristic EDS spectra of the (Ti,Nb,Mo)C carbides with about 4 nm size and 30 nm size carbide shown in Fig. 2.30. The concentration of small particle is estimated to 36(53 at%) \pm 3.0 wt% Ti and 19(14 at%) \pm 3.4 wt% Nb and 45(33 at%) \pm 3.7 wt% Mo, respectively, which corresponds to 0.62 atomic ratio of Mo/Ti. The bigger particle contains 65(78 at%) \pm 7.1 wt% Ti and 14(9 at%) \pm 6.2 wt% Nb and 21(2 at%) \pm 6.5 wt% Mo, respectively.

Fig. 2.32 contains dark field images of 1 μ m size particle with its corresponding diffraction pattern with [011] zone axis of B1 structure carbide. In a diffraction pattern images, the different peaks are selected for dark field images, respectively. Fig. 2.33 indicates characteristic EDS mapping for titanium, niobium and molybdenum using scanning transmission electron microscope of Ti-Nb-Mo steel from thin foil sample. The dark field images and elemental mapping show that these particles contain two different types of carbide. B1 crystal structure titanium carbide locates at the center and molybdenum rich carbides exist surrounding the bigger

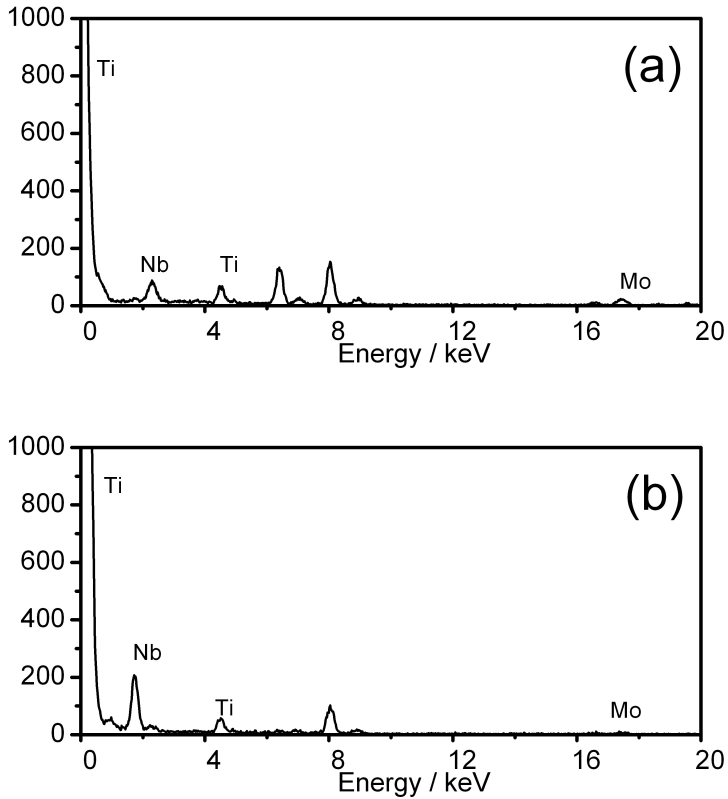


Figure 2.31: Characteristic EDS spectra of the (Ti,Nb,Mo)C carbides with about (a) 4 nm and (b) 30 nm size in the Ti-Nb-Mo steel after prolonged aging at 700°C for 120 h from carbon extraction replicas. It is estimated to contain (a) 36(53 at%) \pm 3.0 wt% Ti and 19(14 at%) \pm 3.4 wt% Nb and 45(33 at%) \pm 3.7 wt% Mo, respectively. It is estimated to have (b) 65(78 at%) \pm 7.1 wt% Ti and 14(9 at%) \pm 6.2 wt% Nb and 21(2 at%) \pm 6.5 wt% Mo, respectively.

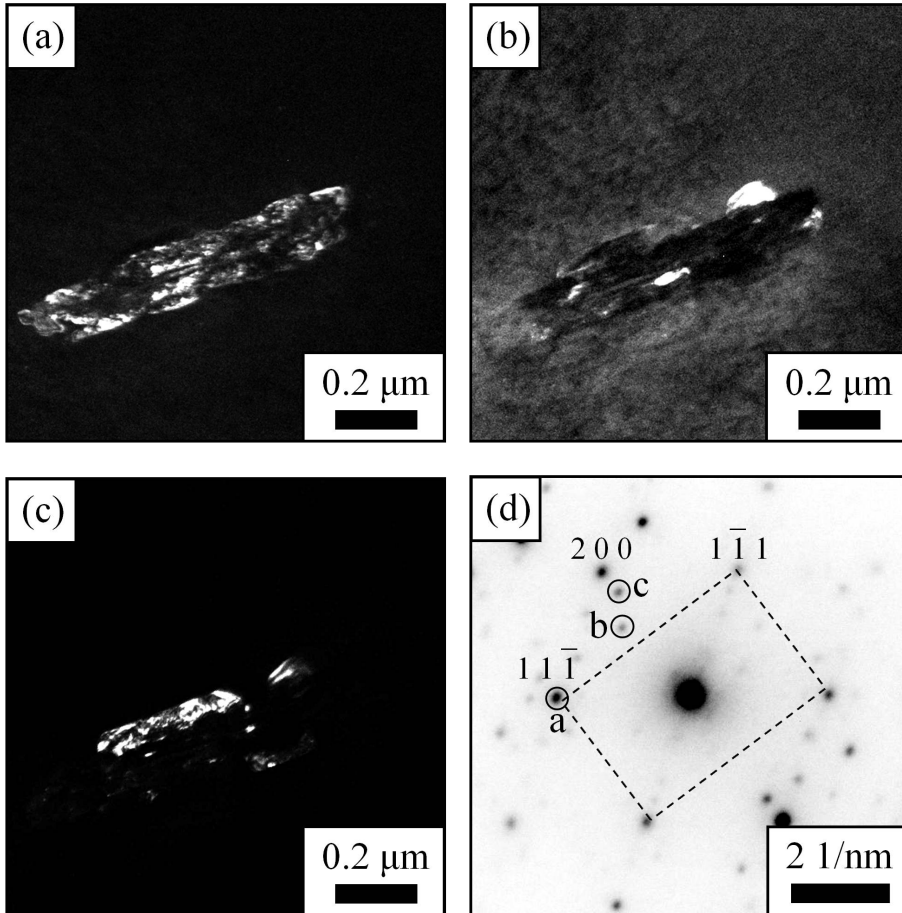


Figure 2.32: TEM images of Ti-Nb-Mo steel after prolonged aging at 700°C for 120 h from thin foil sample. (a) Dark field image correspond to diffraction pattern a, (b) diffraction pattern b (c) diffraction pattern c and (d) corresponding diffraction pattern with $[011]$ zone axis of B1 structure carbides.

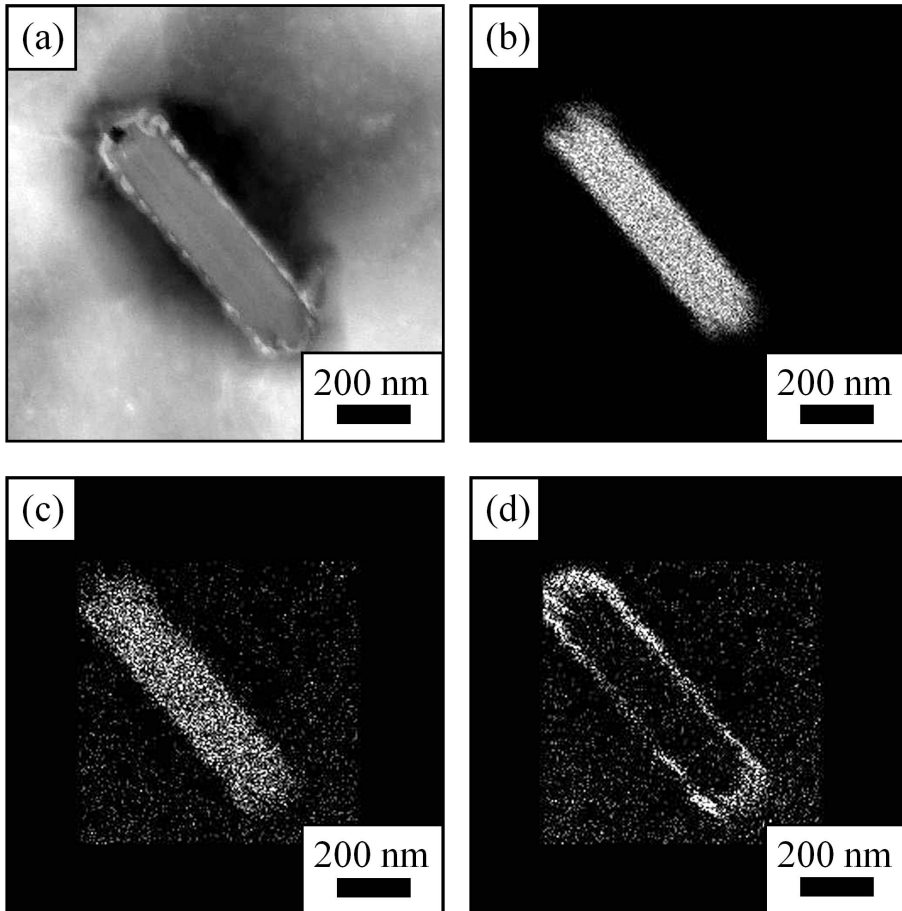


Figure 2.33: EDS mapping using STEM of Ti-Nb-Mo steel after prolonged aging at 700°C for 120 h from thin foil sample. (a) Bright field image and elements mapping of (b) Ti (c) Nb and (d) Mo, respectively.

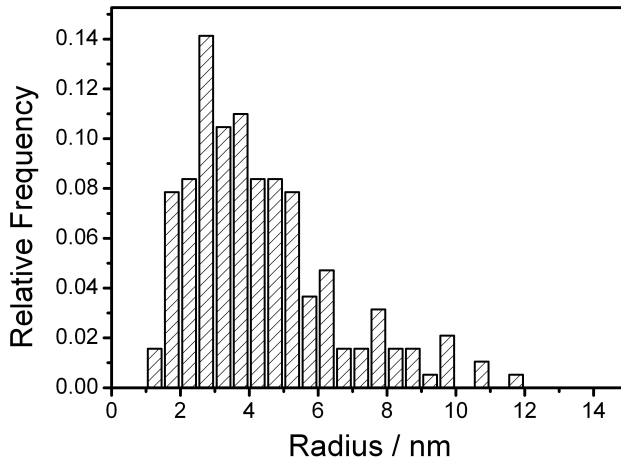


Figure 2.34: Relative frequency as a function of particle radius of (Ti,Nb,Mo)C particles in Ti-Nb-Mo steel after prolonged aging at 700°C for 120 h . The mean value and standard deviation of radius are 4.33 nm and 3.13 nm, respectively.

2.4. Hardness and Precipitate Size

particle.

Fig. 2.34 shows relative frequency dependency on particle radius of (Ti,Nb,Mo)C particles in Ti-Nb-Mo steel after prolonged aging at 700°C for 120 h. The mean value and standard deviation of radius are 4.33 nm and 2.13 nm, respectively.

2.4 Hardness and Precipitate Size

Hardness measurements were made on the ferrite grains in the corresponding optical samples, using a Vickers hardness tester with a load of 1 kg. The load was chosen in order to minimize the sizes of indentation within the ferrite grains so that the influence of other lower temperature structures, which is originated from the rapid cooling of untransformed austenite. The results are averaged using 30 sampling points. The hardness of Ti-Nb steels and Ti-Nb-Mo steels after isothermal holding at 700°C for 40 min are 191 and 196 HV, respectively. The hardness of Ti-Nb steels have decreased more rapidly than Ti-Nb-Mo steels during prolonged aging for 24 h and 120 h. The corresponding values for Ti-Nb alloy changes to 181 and 164 HV, while those for Ti-Nb-Mo alloy changes to 192 and 185 HV, respectively. The difference is about 17 and 11 HV for Ti-Nb alloy and Ti-Nb-Mo alloy during 120 h prolonged ageing.

These hardness measurements can be interpreted using the precipitation size analysis. The measured precipitate sizes above are projected values on 2 dimensional planes and can be converted to a 3 dimensional size by using following equation, which is used for carbon extraction replicas samples (Ashby & Ebeling, 1966).

$$\bar{d}_v = \frac{\bar{d}_s}{1 + \left(\frac{\sigma_s}{\bar{d}_s}\right)^2} \quad (2.1)$$

where \bar{d}_v and \bar{d}_s are the average sizes of precipitates with respect to 2 and 3 dimensions. σ_s is the standard deviation of \bar{d}_s . In this study, Eq. (2.1)

2.4. Hardness and Precipitate Size

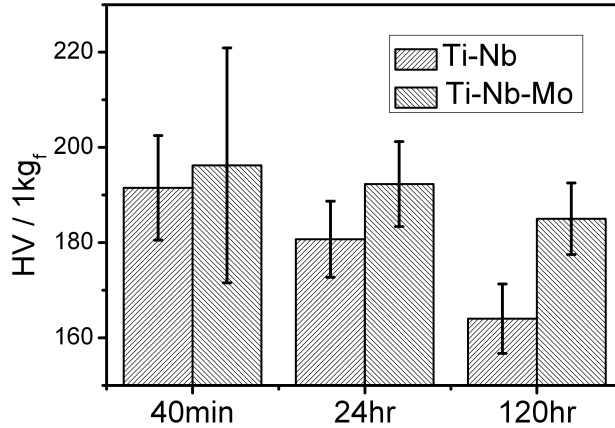


Figure 2.35: Hardness of Ti-Nb and Ti-Nb-Mo steel with different heat treatments.

is applied not only for replicas samples, but also for thin foil based on the assumption that the precipitates size distributions in thin foil are identical to that from replicas. Then the measured average sizes of Ti-Nb steels are converted to 3.46, 4.61 and 5.85 nm for after isothermal holding at 700°C for 40 min, after prolonged ageing 24 h and 120 h, respectively. The converted values of Ti-Nb-Mo steels are 1.56, 2.01 and 3.49 nm for after isothermal holding at 700°C for 40 min, after prolonged ageing 24 h and 120 h, respectively.

The precipitate size for Ti-Nb-Mo steels are relatively small compared with Ti-Nb steels during the heat-treatment. In addition the coarsening rate more rapid in Ti-Nb steels, the coarsening rate constant is proportional to the cube of average precipitation size by LSW theory (Lifshitz & Slyozov, 1961; Wagner, 1961). These experimental results indicate that a certain amount of molybdenum addition promotes interphase precipitation and reduces the particle coarsening rate for the same amount of

titanium concentration in alloys.

References

- ASHBY, M. & EBELING, R. (1966). On the determination of the number, size, spacing, and volume fraction of spherical second-phase particles from extraction replicas. *AIME MET SOC TRANS*, **236**, 1396–1404. [74](#)
- LIFSHITZ, I. & SLYOZOV, V. (1961). The kinetics of precipitation from supersaturated solid solutions. *Journal of Physics and Chemistry of Solids*, **19**, 35–50. [75](#)
- WAGNER, C. (1961). Theory of precipitate change by redissolution. *Electrochimie*, **65**, 581–591. [75](#)
- YANG, H. & BHADESHIA, H. (2007). Uncertainties in dilatometric determination of martensite start temperature. *Materials science and technology*, **23**, 556–560. [47](#)

Chapter 3

Stability of (Ti,M)C

A knowledge of the thermodynamics and interfacial energies of substitutional alloys including niobium, vanadium, molybdenum and tungsten in the (Ti, M)C phase is necessary for modeling precipitation kinetics. In this chapter, this has been achieved from first principles calculation and discrete lattice plane, nearest-neighbor broken-bond model. Suggestions from the calculation are validated by the characterization of precipitates in a series of steels containing Ti, Ti-Mo and Ti-W using transmission electron microscopy (TEM).

3.1 Formation Energy and Lattice Parameter

There has been significant progress with a variety of first principles calculation of thermodynamic parameters, some of which are used for calculation of phase diagrams (CALPHAD) approach. The purpose of the study presented here was to use first-principles calculations to characterize the effect of substitutional solutes on the stability of TiC carbide, where niobium, vanadium, molybdenum and tungsten atoms substitute for titanium. The lattice parameters, formation energies and bulk moduli of (Ti,M)C and M(C,Va) with the B1 crystal structure have been

3.1. Formation Energy and Lattice Parameter

investigated as a function of the substituted atoms.

3.1.1 Computational Model and Methods

The conventional unit cell of B1 structure TiC contains four titanium atoms and four carbon atoms in the nonmagnetic state. The initial calculations were based on the experimental lattice parameter $a_{TiC} = 4.32 \text{ \AA}$, which has been measured at room temperature (Teresiak & Kubisch, 1995). The crystal structures of (Ti,Nb)C, (Ti,V)C, (Ti,Mo)C and (Ti,W)C were simulated by substituting titanium atoms with Nb, V, Mo and W atoms with 1/8, 1/4, 3/4 and 7/8 site fractions, respectively. The Ti(C,Va), Nb(C,Va), V(C,Va), Mo(C,Va) and W(C,Va) are calculated using the structure in which 4, 3, 2 and 1 carbon atoms are substituted by vacancies, corresponding to 0, 12.5, 25 and 37.5 at% of carbon.

For the first-principles calculation, the total energy all-electron full-potential linearized augmented plane-wave (FLAPW) method was used with the local density approximation (LDA) and generalized gradient approximation (GGA) for the exchange-correlation potential (Perdew *et al.*, 1996; Weinert *et al.*, 1982; Wimmer *et al.*, 1981). The integrations over the three-dimensional Brillouin zone were calculated by the tetrahedron method over a $9 \times 9 \times 9$ Monkhorst-Pack mesh, which corresponds to 729 k -points for the TiC structure (Monkhorst & Pack, 1976). The linearized augmented plane-wave (LAPW) basis set was expanded to 21 Ry, which corresponds to 900 LAPW per k -point. The wave functions, the charge densities and the potential were expanded with $l \leq 8$ lattice harmonics inside each muffin-tin sphere. The radii of the muffin-tin spheres were 2.10 a.u. for Fe, 2.40 a.u. for Ti, Nb, V, Mo and W, and 1.30 a.u. for C atoms. The density and potential in the interstitial region were depicted using a star-function cutoff at 340 Ry. The total charge convergence criterion was 1.0×10^{-4} electrons a.u.⁻³ The sphere radii and K_{max} within the whole lattice spacing range were kept constant, to maintain the same degree of convergence for all the lattice constants studied.

3.1. Formation Energy and Lattice Parameter

The initial lattice parameters and the internal atomic positions of (Ti,M)C and M(C,Va) for M = Nb, V, Mo and W were adapted from experimental values of TiC. Seven distinct cubic lattice parameters a , ranging from -3% to 3% in 1% increments, were used to determine the equilibrium lattice parameters. A fourth-order polynomial fitting was used to find the minima. The internal atomic positions were fully relaxed using the total energy and force minimization scheme with the Broyden method to find the multidimensional zero (Mannstadt & Freeman, 1997). Atomic relaxation was achieved when the force on each atom was less than 2 mRy a.u.^{-1} and the displacement of an atom was less than $3 \times 10^{-3} \text{ a.u.}^{-1}$.

The reference states of the pure elements were nonmagnetic hexagonal close-packed (HCP) Ti, body-centered cubic (BCC) Nb, BCC V, BCC Mo, BCC W and graphite C, and ferromagnetic BCC Fe, respectively. The equilibrium lattice parameters were calculated using seven distinct points, ranging from -3% to 3% in 1% steps, for the cubic structures and 25 distinct combinations of the hexagonal lattice parameters a and c , ranging from -2% to 2% in 1% steps, for hcp Ti. The total energy of diamond C was calculated and correction of -17 meV was added for the total energy of graphite C, since it is well known that current exchange-correlation functional does not model graphite accurately (Ande & Sluiter, 2010).

3.1.2 Reference States

Tables 3.1 and 3.2 show calculated equilibrium lattice parameters and bulk moduli of the reference with respect to local density (LDA) and generalized gradient (GGA) approximation, respectively. The calculated lattice parameters at 0 K based on LDA are 2.758, 3.541, 3.265, 2.939, 3.121 and 3.149 Å for BCC Fe, diamond C, BCC Nb, BCC V, BCC Mo and BCC W, respectively, which are about $0.2\sim 2.7\%$ smaller than those of GGA results. The calculated results for HCP Ti are 2.862 and 4.639 Å for a and c direction, which are also 2.1% and 1.0% smaller than those of GGA.

3.1. Formation Energy and Lattice Parameter

Table 3.1: Calculated equilibrium lattice parameters of the reference materials of ferromagnetic BCC Fe, diamond C, HCP Ti, BCC Nb, BCC V, BCC Mo and BCC W based on local density (LDA) and generalized gradient approximation (GGA), respectively. The reference values are included for comparison (<http://www.webelements.com>).

/ Å	LDA	GGA	reference
BCC Fe	2.758	2.833	2.867
diamond C	3.541	3.575	3.57
HCP Ti	2.862(<i>a</i>) 4.639(<i>c</i>)	2.921(<i>a</i>) 4.686(<i>c</i>)	2.95(<i>a</i>) 4.69(<i>c</i>)
BCC Nb	3.265	3.301	3.30
BCC V	2.949	3.00	3.03
BCC Mo	3.121	3.159	3.147
BCC W	3.149	3.193	3.165

The bulk moduli were calculated from the partial derivative of pressure with respect to volume,

$$P = -\left(\frac{\partial E}{\partial V}\right) \quad (3.1)$$

$$B = -V\left(\frac{\partial P}{\partial V}\right). \quad (3.2)$$

The calculated bulk moduli are 232, 480, 121, 170, 195, 270, 313 GPa for BCC Fe, diamond C, HCP Ti, BCC Nb, BCC V, BCC Mo and BCC W, respectively, based on the LDA approximation, which are about 1.5%~25% bigger than referenced values, except for Nb. The differences are bigger than those from lattice parameters, because the second derivative of energy states are more sensitive than the minimum value. These results are consistent with the previous studies that the lattice parameters on LDA are a little smaller than GGA, and the bulk moduli on LDA are bigger than GGA (Csonka *et al.*, 2009; Lee & Martin, 1997; Steinle-Neumann *et al.*, 1999).

3.1. Formation Energy and Lattice Parameter

Table 3.2: Calculated bulk moduli of the reference materials of ferromagnetic BCC Fe, diamond C, HCP Ti, BCC Nb, BCC V, BCC Mo and BCC W based on local density (LDA) and generalized gradient approximation (GGA), respectively. The reference values are included for comparison (<http://www.webelements.com>).

/ GPa	LDA	GGA	reference
BCC Fe	232	211	170
diamond C	480	444	442
HCP Ti	121	110	110
BCC Nb	170	146	170
BCC V	186	155	160
BCC Mo	270	279	230
BCC W	313	309	310

3.1.3 (Ti,M)C Structure

Fig. 3.1 shows calculated formation energies versus lattice parameter of TiC with the data fitted to the fourth order polynomial. The calculated data show a good agreement with the corresponding fitting function, and the equilibrium lattice parameters and bulk moduli for TiC, NbC, VC, MoC and WC are calculated using the fitting results.

Table 3.3 shows the calculated equilibrium lattice parameters, the formation energies and the bulk moduli of TiC, NbC, VC, MoC and WC in the B1 crystal structure, with the experimental values for comparison. The first values for lattice parameters are calculated based on LDA and the second values are based on GGA for exchange-correlation potential. Formation energies and bulk moduli are calculated by LDA.

The calculated lattice parameters at 0 K based on LDA are $a_{TiC}=4.30 \text{ \AA}$, $a_{NbC}=4.48 \text{ \AA}$ and $a_{VC}=4.11 \text{ \AA}$, which are 0.5% smaller, 0.2% larger and 1.5% smaller than the experimental values at room temperature, respectively. With the exception of NbC, the agreement is reasonable, assuming that the calculated lattice parameters increase due to thermal expansion

3.1. Formation Energy and Lattice Parameter

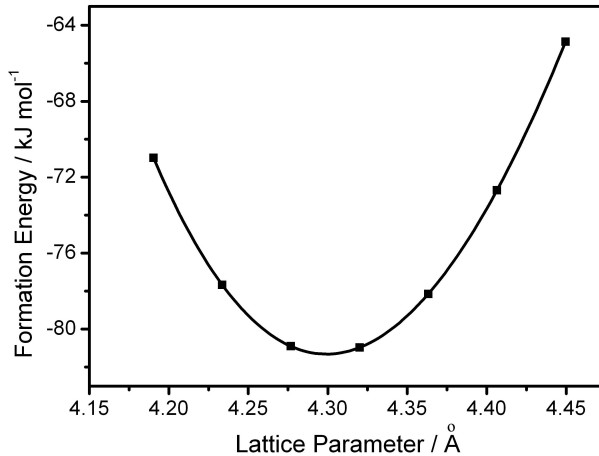


Figure 3.1: Calculated formation energies versus lattice parameter of TiC. The corresponding lines are fourth order polynomial fits.

Table 3.3: Calculated equilibrium lattice parameters, formation energy and bulk modulus. The first values for lattice parameters are calculated based on LDA and the second values are based on GGA for exchange-correlation potential. Formation energies and bulk moduli are calculated by LDA. The formation energies and bulk moduli of TiC, NbC, VC, MoC and WC are included in parenthesis for reference.

/	Lattice Parameter / Å	ΔU / kJ mol ⁻¹	Bulk Modulus / GPa
TiC	4.299(L) 4.367(G)	-81.9(-92 ^a)	243(240 ^b)
NbC	4.477(L) 4.528(G)	-47.4(-56 ^c)	318(301 ^b)
VC	4.113(L) 4.187(G)	-45.5(-59 ^a)	341(304 ^b)
MoC	4.360(L) 4.383(G)	17.0(10 ^c)	351(337 ^b)
WC	4.356(L) 4.387(G)	27.1	384(365 ^b)

^a(Teresiak & Kubsch, 1995), ^b(Isaev *et al.*, 2007), ^c (Hugosson *et al.*, 2001a)

3.1. Formation Energy and Lattice Parameter

up to room temperature. The calculated lattice parameters of MoC and WC are $a_{MoC}=4.35 \text{ \AA}$ and $a_{WC}=4.36 \text{ \AA}$, which are about 1% larger than that of TiC. Meanwhile, the experimentally measured lattice parameters of MoC and WC are 4.28 and 4.27 \AA , while are about 1% smaller than TiC. Even though the calculated lattice parameter is the value for 0 K and the measured one is for ambient temperature, this discrepancy is notable and it will be discussed later with the calculated results of the M(C,Va) structure.

The formation energies were calculated as the differences between the total energy of each phase and the sum of the energies of the stable states of the pure elements. The formation energy (ΔU) at 0 K of each system is defined,

$$\Delta U = E(MC) - E(M) - E(C) \quad (3.3)$$

where $E(MC)$ are the total energies MC type carbide with M for Ti, Nb, V, Mo and W. $E(M)$ and $E(C)$ are the total energies of the referenced states. The calculated formation energies of TiC, NbC, VC, MoC and WC are -81.9 , -47.4 , -45.5 , 17.0 and 27.1 kJ mol^{-1} , respectively. Compared with the measured ones at room temperature, the calculation results are smaller by 10%. The differences possibly come from the fact that the calculation considers the energy at 0 K.

Table 3.3 also shows the bulk moduli of the B1 crystal structure MC with $M = \text{Ti, Nb, V, Mo and W}$. The calculated bulk moduli are 243, 318, 341, 351 and 384 GPa for TiC, NbC, VC, MoC and WC, respectively, which are 1.3%, 5.6%, 12.2%, 4.2% and 5.2% larger than the referenced ones calculated by GGA (Isaev *et al.*, 2007). This agrees with the calculated results on the nitrides showing that LDA yields 1~2% smaller lattice constants but 10~20% larger bulk moduli than GGA (Stampfl *et al.*, 2001).

Figs 3.2 and 3.3 indicate the calculated formation energies and lattice parameters as a function of site fraction of alloying elements M in the

3.1. Formation Energy and Lattice Parameter

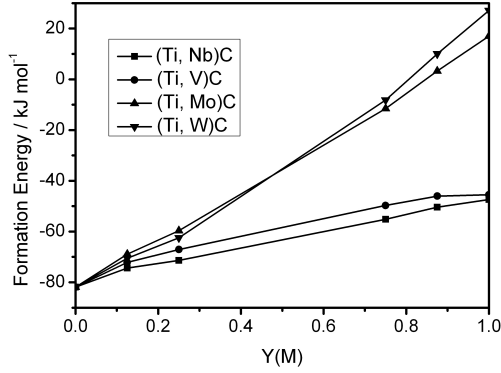


Figure 3.2: The calculated formation energies dependencies on site fraction of (Ti,M)C type B1 structure, with $M = \text{Nb, V, Mo and W}$. The rectangles, circles, triangles and inverted triangles represent the respective calculated results.

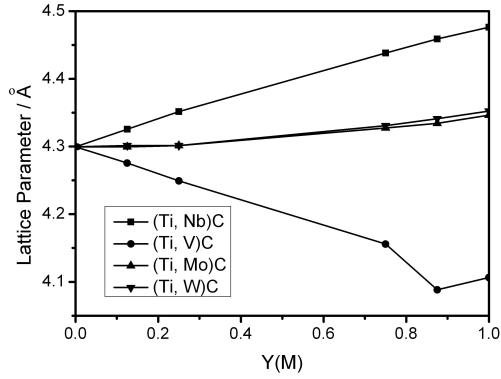


Figure 3.3: The calculated lattice parameters dependencies on site fraction of (Ti,M)C type B1 structure, with $M = \text{Nb, V, Mo and W}$. The rectangles, circles, triangles and inverted triangles represent the respective calculated results.

3.1. Formation Energy and Lattice Parameter

(Ti,M)C-type B1 structure. The formation energy (ΔU) at 0 K of super-cell system with 4 and 8 metal atoms are defined, with the integer x ,

$$\Delta U = \frac{E((\text{Ti}_{4-x}, \text{M}_x)\text{C}_4) - (4-x) \times E(\text{Ti}) - x \times E(\text{M}) - 4 \times E(\text{C})}{8} \quad (3.4)$$

$$\Delta U = \frac{E((\text{Ti}_{8-x}, \text{M}_x)\text{C}_8) - (8-x) \times E(\text{Ti}) - x \times E(\text{M}) - 8 \times E(\text{C})}{16} \quad (3.5)$$

where $E((\text{Ti}_{4-x}, \text{M}_x)\text{C}_4)$ and $E((\text{Ti}_{8-x}, \text{M}_x)\text{C}_8)$ are the total energies of $(\text{Ti}_{4-x}, \text{M}_x)\text{C}_4$ and $(\text{Ti}_{8-x}, \text{M}_x)\text{C}_8$ carbide with M for Ti, Nb, V, Mo and W. $E(\text{M})$ and $E(\text{C})$ are the total energies of the referenced states. The formation energies and lattice parameter changes show the linearity with respect to the site fraction of titanium replacement.

It shows that the partial replacements of Ti by Nb, V, Mo and W will increase the formation energies of (Ti,M)C particles. It is notable that Mo and W significantly increase the formation energy, which is expected, considering the instability of MoC and WC. The formation energies of solution states of metals in ferrite matrix are also necessary to know the stability of replacement of Ti in carbide lattice. The comparison illustrated schematically in Fig. 3.4. The formation energies of solution states are calculated using the super-cell doubled in 3 dimensions with conventional body centered cubic unit cell containing 16 iron atoms.

The formation energy (ΔU) at 0 K of solution system with 15 iron atoms and 1 metal atoms are defined

$$\Delta U = \frac{E(\text{Fe}_{15}\text{M}) - 15 \times E(\text{Fe}) - E(\text{M})}{16} \quad (3.6)$$

where $E(\text{Fe}_{15}\text{M})$ are the calculated total energies of super-cell replaced by M=Ti, Nb, V, Mo and W, respectively. $E(\text{Fe})$ and $E(\text{M})$ are the total energies of the referenced states. The formation energies of solution states in ferrite matrix are calculated as -4.23 , 3.02 , -3.64 , 2.82 and 2.49 kJ mol⁻¹ for Ti, Nb, V, Mo and W, respectively. In Fig. 3.3, the val-

3.1. Formation Energy and Lattice Parameter

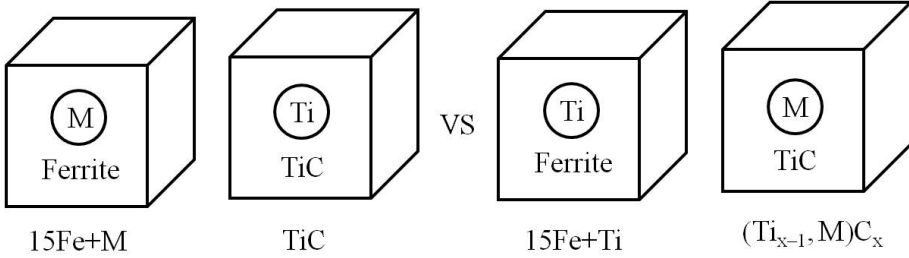


Figure 3.4: Schematic diagrams showing the stability of replacement of metal atoms at the lattice site of TiC with respect to solid solution in ferrite matrix.

Table 3.4: Calculated formation energies with kJ mol^{-1} units of Fe_{15}M and $(\text{Ti}_7, \text{M})\text{C}_8$ structure with the values for comparison.

M	Fe_{15}M	$(\text{Ti}_7, \text{M})\text{C}_8$	$\text{Fe}_{15}\text{M} + \text{TiC}$	$\text{Fe}_{15}\text{Ti} + (\text{Ti}_7, \text{M})\text{C}_8$
Ti	-4.2	-81.9	-	-
Nb	3.0	-74.4	-78.9	-83.1
V	-3.6	-72.2	-85.5	-76.4
Mo	2.8	-68.9	-79.1	-73.1
W	2.5	-70.5	-79.4	-74.7

ues corresponds to $1/8$ site fraction can be used to compare the solution states, since those structures contains $1/16$ mole fraction of replacement metal atoms. These values are listed in Table 3.4. It shows that the partial replacement of Ti by V, Mo and W will increase the summation of formation energies $(\text{Ti}, \text{M})\text{C}$ particles and ferrite solution, while that of Nb will decrease. This means the introduction of V, Mo and W atom into TiC lattice is energetically unfavorable.

3.1. Formation Energy and Lattice Parameter

3.1.4 M(C,Va) Structure

As mentioned, the calculated lattice parameters of MoC and WC in the B1 crystal structure are larger than that of TiC, which does not match well with experimental observations. However, it has been noted that the introduction of vacancies at carbon positions in the B1 crystal structure increases the stability of certain carbides (Hugosson *et al.*, 2001b). Since the replacement of carbon by a vacancy will cause the lattice to contract, it possibly has an influence on the lattice parameter. Figs 3.5 and 3.6 show the calculated formation energies and the equilibrium lattice parameter of M(C,Va)-type carbides in the B1 crystal structure for M = Ti, Nb, V, Mo and W with different atomic percentages of carbon based on LDA. The formation energy (ΔU) at 0 K of each system is defined, with the integers x ,

$$\Delta U = \frac{E(M_4, (C_{4-x}, Va_x)) - 4 \times E(M) - (4 - x) \times E(C)}{8 - x} \quad (3.7)$$

where $E(M_4, (C_{4-x}, Va_x))$ is the total energy of $M_4, (C_{4-x}, Va_x)$ with M for Ti, Nb, V, Mo and W. $E(M)$ and $E(C)$ are the total energies of the referenced states.

Here, C = 0 at% corresponds to a face-centered cubic (fcc) structure without interstitial atoms and C = 50 at% represents a perfect B1 crystal structure. It is seen that TiC, NbC and VC have the lowest formation energies with a structure without vacancies, whereas MoC and WC are more stable structure when approximately 50% of carbon in the lattice is substituted with vacancies. This implies that MoC_{0.5} and WC_{0.5} are more stable than MoC and WC for the B1 crystal structure. With half of the carbon atoms being replaced by vacancies, the lattice parameters of MoC and WC are evaluated to be $a_{MoC}=4.21 \text{ \AA}$ and $a_{WC}=4.22 \text{ \AA}$. Consistent with the experimental data, these are approximately 2 % smaller than that of TiC. This implies that complete substitution of Ti in TiC lattice by Mo with the introduction of vacancies to half of the carbon positions

3.1. Formation Energy and Lattice Parameter

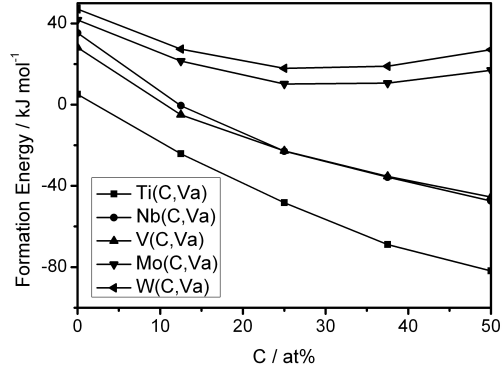


Figure 3.5: The calculated formation energies of $M(C,Va)$ type B1 structure carbides with $M = Ti, Nb, V, Mo$ and W . The solid rectangles, circles, triangles, inverted and left-pointing triangles represent the calculated results for Ti, Nb, V, Mo and W, carbides, respectively.

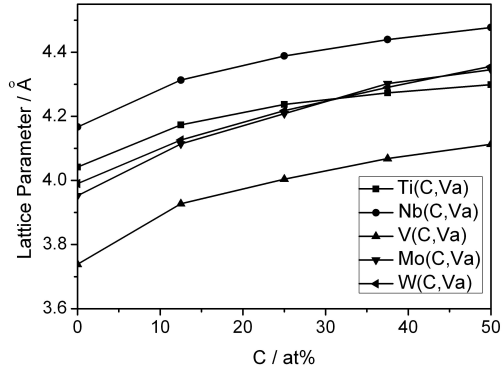


Figure 3.6: The calculated lattice parameters of $M(C,Va)$ type B1 structure carbides with $M = Ti, Nb, V, Mo$ and W . The solid rectangles, circles, triangles, inverted and left-pointing triangles represent the calculated results for Ti, Nb, V, Mo and W, carbides, respectively.

will reduce the misfit between ferrite and MC carbide from 5.6 % to 3.6 %.

3.2 Interfacial Energy

A theory based on calculation of phase equilibrium or precipitation kinetics including nucleation, growth and coarsening process was developed that incorporates Gibbs-Thomson effect (Aronson *et al.*, 1978; Christian, 2002; Zener, 1949). In these models, the effect of interfacial energy is included in energy shift of alloys and phases and there have been many studies to determine the interfacial energy experimentally. These experimental values of interfacial energy of precipitates are scattered over a wide range (Shahandeh & Nategh, 2007). Most of the mentioned data are obtained from coarsening experiments by relating their size distribution to ageing time and use of Lifshitz-Slyozov-Wagner (LSW) theory. Besides the unavoidable experimental errors in estimation of the size distribution of the precipitates, the diffusivity of the atoms in the system also results in uncertain values for interfacial energy. In this chapter, the interfacial energy between ferrite and MC type carbide with Baker-Nutting orientation relationship has been determined using first principles calculations and discrete-lattice plane, nearest-neighbor broken-bond (DLP/NNBB) method.

3.2.1 First-Principles Calculations

The atomic configuration at the interface between BCC ferrite and B1 type carbide have the Baker-Nutting orientation relationship was considered using the unit cell illustrated in Fig. 3.7. The interface structures assume that the locations of Ti atoms correspond to the positions of Fe atoms in the body-centered cubic structure and C atoms are located on the corresponding octahedral interstitial sites. This cell contains eight iron atoms, four metal atoms and four carbon atoms.

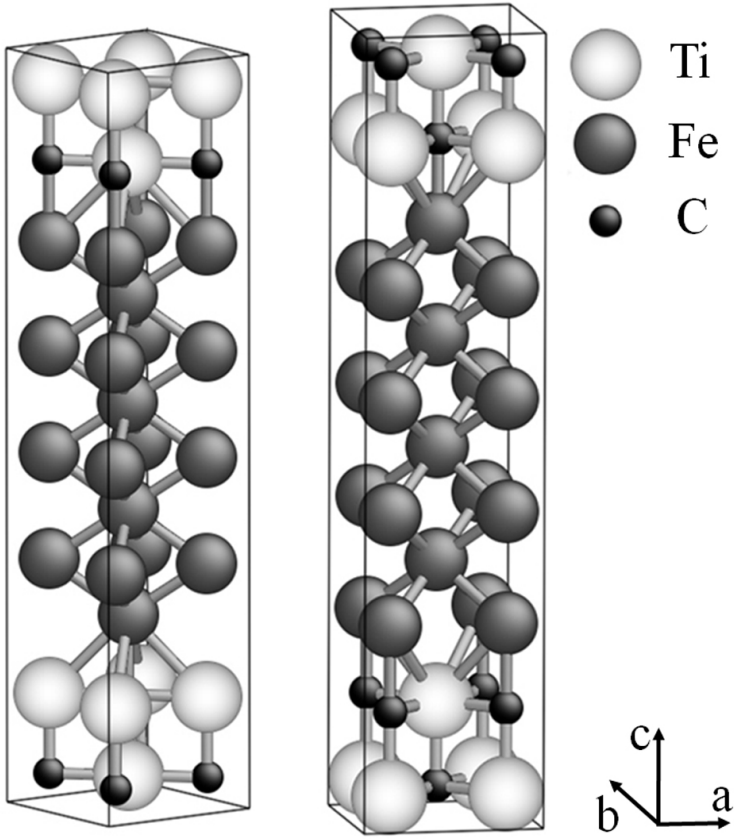


Figure 3.7: Conventional unit cells showing the Fe-TiC interface structure with a Baker-Nutting orientation relationship. This cell contains eight Fe atoms, four Ti atoms and four C atoms.

3.2. Interfacial Energy

The lattice parameters of this unit cell are determined by the points which have the same elastic strain energy between the ferrite and the carbides. Since both ferrite and carbides are strained biaxially at the interface, their structures will change into tetragonal. The lattice parameters of ferrite and carbides under the constraint of the interface were calculated using 25 distinct combinations of the tetragonal lattice parameters in a and c directions between -2% to 2% in 1% steps. The lattice spacing at the interface between ferrite and carbides was determined using seven distinct points from -3% to 3% in 1% steps, based on the average lattice spacing of ferrite and MC carbides.

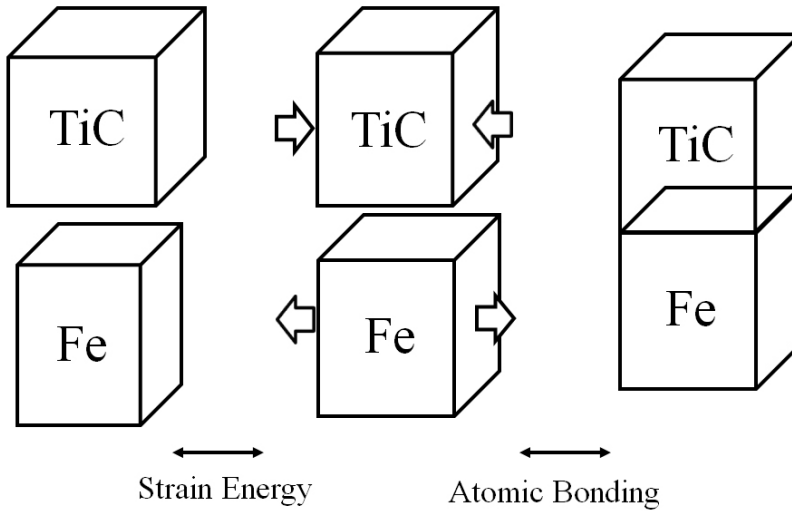


Figure 3.8: Schematic diagram illustrating the factors contribute to interfacial energy. The first term is the elastic strain energy which is necessary to achieve coherent matches at the interface. The second part is the energy difference induced from the change of atomic bonding.

In this study, it is assumed that the interfacial energy is composed of elastic strain energy and energy related with the broken bonding at

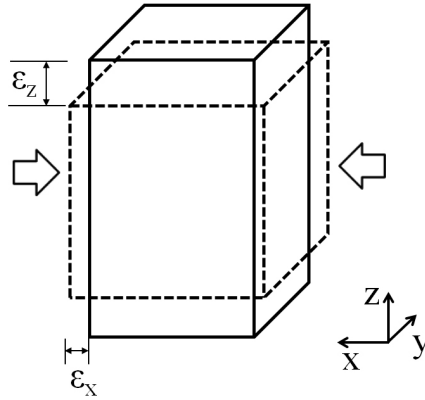


Figure 3.9: Schematic diagram illustrating the change of cubic structure of MC carbide and ferrite induced from the strain at interface. Contraction of lattice parameter in two dimensions along the interface and extraction along the normal direction of interface will occur.

the interface as illustrated in Fig. 3.8. As mentioned, the cubic structures of ferrite matrix and MC carbide will have tetragonality at the interface because the ferrite lattice should be stretched and that of MC carbide has to shrink at the interface to achieve a match like Fig. 3.9. The equilibrium lattice parameters of tetragonal structure have been achieved by using 25 distinct combinations in a and c -direction between -2% to 2% in steps of 1% .

The elastic strain associated with the coherent interface can be estimated from the intersection point of the lattice parameter that generates the same elastic strain energy in ferrite and carbide lattice as shown in Fig. 3.10. Since a contraction of the lattice parameter of TiC is desirable for better coherency with ferrite, the partial replacement of Ti by Mo or W during the formation of TiC particles can help to decrease the strain energy and keep the interface coherent with a Baker-Nutting orientation relationship.

3.2. Interfacial Energy

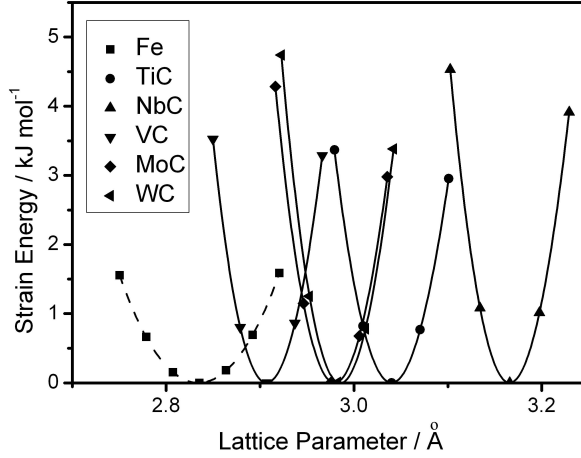


Figure 3.10: The calculated elastic strain energy dependencies on lattice parameters of B1 structure TiC, NbC, VC, MoC_{0.5} and WC_{0.5} with BCC ferromagnetic ferrite. To comparison with ferrite, the lattice parameters of MC carbides are divided by $\sqrt{2}$. The solid and dashed lines show fitted line to find the equilibrium lattice parameters and intersection point with ferrite.

Table 3.5: Calculated lattice parameters and strain energy. The first values for lattice parameters in a and c directions are the values for BCC Fe and second values are for MC-type carbide.

	a / Å(Fe, MC)	c / Å(Fe, MC)	Strain Energy / kJ mol ⁻¹
Fe-TiC	2.972, 4.203	2.687, 4.341	4.10
Fe-NbC	3.064, 4.333	2.584, 4.532	11.40
Fe-VC	2.885, 4.080	2.779, 4.123	0.54
Fe-MoC _{0.5}	2.935, 4.151	2.727, 4.200	2.16
Fe-WC _{0.5}	2.941, 4.159	2.721, 4.229	2.43

3.2. Interfacial Energy

Table 3.5 shows the calculated lattice parameters in a and c -directions, and the strain energy. The lattice parameters in the a -direction where ferrite intersects with TiC, NbC, VC, MoC_{0.5} and WC_{0.5} are 2.972, 3.064, 2.885, 2.935 and 2.941 Å, respectively. This means that the ferrite lattice should be stretched parallel to the interface by approximately 4.8%, 8.1%, 1.8%, 3.5% and 3.7%, respectively, to form a coherent interface with each carbide particle. Assuming that the elastic strain energy will be proportional to the square of the misfit strain, the strain energy associated with the coherent interface between the TiC and the ferrite matrix will be twice as much as those from MoC_{0.5} or WC_{0.5}. The strain energy contributions in the interfacial energy can be converted as 154, 403, 22, 83 and 93 J m⁻² on the assumption that the strain energy is localized to one atomic layer of ferrite and MC type structure, respectively.

$$\sigma_s = \frac{2 \times E_s}{a_\alpha^2 \times N_A} \quad (3.8)$$

where σ_s is the strain energy contribution for the interfacial energy, E_s is the strain energy in Table 3.5 and a_α is the lattice parameter of ferrite. N_A is the Avogadro's constant.

Meanwhile, the energy of coherent interface will be affected by the species of atoms having chemical bonds across the interface, as well as by the strain energy. The contribution from the chemical bonding can be calculated from following equation:

$$\sigma_c = \frac{E_{\alpha/MC} - E_{\alpha,Strained} - E_{MC,Strained}}{2A} \quad (3.9)$$

where $E_{\alpha/MC}$ represents the total energy of a unit cell, which consists of tetragonal ferrite and MC carbide and their interface. $E_{\alpha,Strained}$ and $E_{MC,Strained}$ are those of the tetragonal structure ferrite and the tetragonal MC carbides, respectively. A indicates the area of their interface. Table 3.6 lists the contributions of chemical bonding to the interfacial

3.2. Interfacial Energy

Table 3.6: Calculated equilibrium lattice distance and contribution of chemical term to interfacial energy. The distances are for the distance between BCC Fe and MC-type carbide layer. The interfacial energies of TiC are included in parenthesis for reference. (Jung *et al.*, 2008)

	Distance / Å	σ_c / mJ m ⁻²	σ_s / mJ m ⁻²
Fe-TiC	1.838	339(263)	154
Fe-NbC	1.859	-236	403
Fe-VC	1.811	199	22
Fe-MoC _{0.5}	1.769	256	83
Fe-WC _{0.5}	1.771	197	93

energy and the equilibrium distance between (001) _{α} and (001)_{MC} planes at the interface.

Table 3.6 lists the calculated equilibrium lattice distance and chemical and strain contributions to interfacial energy. The contributions of chemical bonding are about 339, -236, 199, 256 and 197 mJ m⁻². The calculated value between ferrite and TiC is larger compared to that in reference, possibly because the present calculation was done with only lattice parameter optimization, without atomic position relaxation. The chemical bonding component of the interfacial energy of MoC_{0.5} and WC_{0.5} gives 40% and 42% smaller values than that of TiC, respectively.

Even though the exact calculations of the interfacial energies depend on the spread over which the interface is defined, the calculated results of the contributions from both the strain energy and the chemical bonding imply that the partial substitution of Ti by Mo or W will have a beneficial effect in reducing the interface energies. This is consistent with the experimental observation that (Ti,M)C precipitates with a high concentration of Mo were observed at the initial stage of precipitation, when the contribution of interfacial energy is critical to encourage nucleation (Seto *et al.*, 2007). It is noted that the chemical contribution of the interfacial energy for the ferrite and NbC interfaces are calculated to be negative,

which is consistent with other reports using first-principles calculation or the nearest-neighbor broken-bond model (Chung *et al.*, 2006).

3.2.2 Discrete-Lattice Plane, Nearest-Neighbor Broken-Bond Model

B1-type carbides and nitrides are reported to have a Baker-Nutting relationship with ferrite. Not only the structural energy, but also the chemical energy of these compounds gives a major contribution to interfacial energy. A discrete-lattice plane, nearest-neighbor broken-bond (DLP/NNBB) model with constant bond energies had been used to calculate the energy of coherent interphase boundaries in substitutional binary alloys (Dregia & Wynblatt, 1991; Ramanujan *et al.*, 1992; Yang & Enomoto, 2001, 2002). This method was originated from Becker's model, and a convenient approach of counting the number of nearest neighbor bonds on several atom planes was studied (Becker, 1938; Mackenzie *et al.*, 1962). In this study, DLP/NNBB model was applied to a ternary substitutional-interstitial system to study the chemical interfacial energy between ferrite and B1 type MC-carbide. The bond energies of substitutional atoms and the difference of bond energies between Fe-C atoms and M-C atoms are evaluated using *ThermoCalc* based on *TCFE6.2* database and first-principles calculations.

Fig 3.7 illustrates the crystal lattices of Baker-Nutting related B1 carbide and ferrite. The solubility of C atoms in ferrite is very small, and the concentration of Fe atoms in the B1 carbide is also assumed to be small. After the B1 lattice is contracted $1/\sqrt{2}$ times along the [001] direction and a few percent along [100] and [010] directions, it is perfectly coherent with the ferrite lattice. The entropy term was unlikely to have a sizable contribution to the total interfacial energy with ferrite (Yang & Enomoto, 1999). This implies that the concentration of solute atoms can be regarded as constant up to the interfacial plane and the interfacial energy is calculated only from the difference in cohesive energy between

3.2. Interfacial Energy

the interfacial region and the bulk as,

$$\sigma = E_{\alpha/\text{MC}} - \frac{1}{2}(E_{\alpha/\alpha} - E_{\text{MC}/\text{MC}}) \quad (3.10)$$

where $E_{\alpha/\text{MC}}$ is the sum of bond energies across the ferrite-MC carbide interface, and $E_{\alpha/\alpha}$ and $E_{\text{MC}/\text{MC}}$ are the sum of the bond energies across the planes parallel to the interface in the ferrite and MC carbide, respectively.

For an $(001)_{\alpha} || (001)_{\text{MC}}$ interface with Baker-Nutting orientation relationship, the cohesive energy on the assumption that the bonds within second nearest distance only can contribute to the energy are expressed as

$$E_{\alpha/\text{MC}} = n_M \sum_{n=1}^2 \{Z_{\text{Fe-M}}^n e_{\text{Fe-M}}^{\sigma(n)} + Z_{\text{Fe-C}}^n e_{\text{Fe-C}}^{\sigma(n)}\} \quad (3.11)$$

$$E_{\alpha/\alpha} = n_M \sum_{n=1}^2 Z_{\text{Fe-Fe}}^n e_{\text{Fe-Fe}}^{\alpha(n)} \quad (3.12)$$

$$E_{\text{MC}/\text{MC}} = n_M \sum_{n=1}^2 Z_{\text{M-M}}^n e_{\text{M-M}}^{\text{MC}(n)} + (n_M + n_C) \sum_{n=1}^2 Z_{\text{M-C}}^n e_{\text{M-C}}^{\text{MC}(n)} \quad (3.13)$$

where n_M and n_C are the number of metal and carbon atom sites per unit area of interfaces, respectively. $Z_{\text{Fe-M}}^n$ and $Z_{\text{M-C}}^n$ is the coordination number, where the superscript $n(= 1, 2)$ designates the first and second nearest neighbor atoms across interface between substitutional atoms, and between substitutional and carbon atoms, respectively. $Z_{\text{Fe-Fe}}^n$ and $Z_{\text{M-M}}^n$ can be assumed to be same with $Z_{\text{Fe-M}}^n$. $e_{\text{A-B}}^{\text{p}(n)}$ are the bond energies between A and B in the phase p.

The values of n_M and n_C can be evaluated from the relationship, $n_M = n_1 d_{hkl}$ and $n_C = n_2 d_{hkl}$ where $n_1 = n_2 = 4/a_{\text{MC}}^3$ are the number of metal and carbon atom site per unit volume for a lattice parameter a_{MC} , respectively. For a $d_{002} = \frac{1}{2}a_{\text{MC}}$, $n_M = n_C = 2/a_{\text{MC}}^2$. Substitution of

3.2. Interfacial Energy

Eqs (3.11)–(3.13) into Eq. (3.10), the following equation can be obtained.

$$\sigma = n_M \sum_{n=1}^2 \{Z_{\text{Fe-M}}^n \Delta e_{\text{Fe-M}}^n + Z_{\text{M-C}}^n \Delta e_{\text{M-C}}^n\} \quad (3.14)$$

where $\Delta e_{\text{Fe-M}}^n$ and $\Delta e_{\text{M-C}}^n$ are defined by

$$\Delta e_{\text{Fe-M}}^n = e_{\text{Fe-M}}^{\sigma(n)} - \frac{1}{2}(e_{\text{Fe-Fe}}^{\alpha(n)} + e_{\text{M-M}}^{\text{MC}(n)}) \quad (3.15)$$

$$e_{\text{M-C}}^n = e_{\text{Fe-C}}^{\sigma(n)} - e_{\text{M-C}}^{\text{MC}(n)} \quad (3.16)$$

Therefore, Eq. (3.14) can be rewritten as

$$\sigma = n_M \{(Z_{\text{Fe-M}}^1 + pZ_{\text{Fe-M}}^2) + Z_{\text{M-C}}^1 \Delta e_{\text{M-C}}\} \quad (3.17)$$

on the assumption that $\Delta e_{\text{Fe-M}}^1 = \Delta e_{\text{Fe-M}}$, $\Delta e_{\text{Fe-M}}^2 = p\Delta e_{\text{Fe-M}}$, $\Delta e_{\text{M-C}}^1 = \Delta e_{\text{M-C}}$ and $\Delta e_{\text{M-C}}^2 = 0$.

The interfacial coordination number of metal and carbon atoms to a Fe atom across the ferrite-carbide interface can be determined as $Z_{\text{Fe-M}}^1 = 4$, $Z_{\text{Fe-M}}^2 = 1$ and $Z_{\text{M-C}}^1 = 1$ from Fig. 3.7. In this study, $\Delta e_{\text{Fe-M}}$ was evaluated from the regular solution constants in face-centered cubic (FCC) structure based on the assumption that $e_{\text{A-B}}^{\sigma(n)} = e_{\text{A-B}}^{\alpha(n)} = e_{\text{A-B}}^{\text{MC}(n)}$. These assumptions are acceptable, because the nearest bond length of ferrite is 2.485 Å, which is only about 2% smaller than that of austenite using the experimentally measured lattice parameter of $a_\alpha = 2.86$ Å and $a_\gamma = 3.6$ Å (Onink *et al.*, 1993). Whereas the reported regular-solution constants are usually temperature dependent, the magnitude of the dependence is not significant (Yang & Enomoto, 2001). Therefore, the Fe-M bond energies can be evaluated using mixing enthalpy of regular solution model of FCC structure as

$$\Delta H_{\text{mix}} = N_A Z x(1-x) \Delta e_{\text{Fe-M}} \quad (3.18)$$

3.2. Interfacial Energy

where N_A is the Avogadro's number, $Z = 12$ is the bulk coordination number of metal atom in the FCC structure, x is the atomic fraction of solutes.

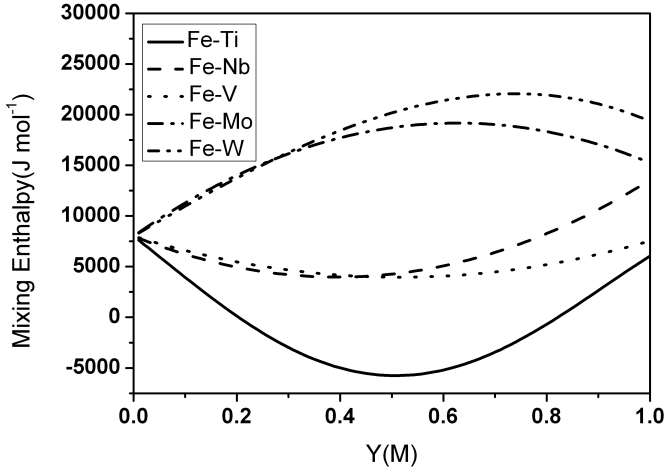


Figure 3.11: The calculated enthalpy of mixing of austenite at 300 K versus atomic fraction of Ti, Nb, V, Mo and W, respectively. The values corresponds to 0.0 represents FCC Fe. The values at 1.0 represent FCC Ti, Nb, V, Mo and W, respectively.

Fig. 3.11 shows the system enthalpy dependency of FCC structure Fe with respect to atomic fraction of Nb, V, Mo and W calculated by *ThermoCalc* using *TCFE6.2* database. The mixing enthalpies are evaluated at the 0.5 atomic fraction.

$$\Delta H_{mix}(0.5) = H(0.5) - \frac{1}{2}\{H(0.0) + H(1.0)\} \quad (3.19)$$

where $H(x)$ represents system enthalpy corresponds to atomic fraction x . The calculated $H_{mix}(0.5)$ are -12781 , -6520 , -3821 , 7085 and 6493 J mol⁻¹ for Ti, Nb, V, Mo and W solutions, respectively. These values

3.2. Interfacial Energy

corresponds to -0.707×10^{-20} , -0.211×10^{-20} , -0.361×10^{-20} , 0.392×10^{-20} and 0.359×10^{-20} J for $\Delta e_{\text{Fe-Ti}}$, $\Delta e_{\text{Fe-Nb}}$, $\Delta e_{\text{Fe-V}}$, $\Delta e_{\text{Fe-Mo}}$ and $\Delta e_{\text{Fe-W}}$, respectively. The bonding energies are positive in the case of Fe-Mo and Fe-W solution, while those are negative in the case of Fe-Ti, Fe-Nb and Fe-V solutions.

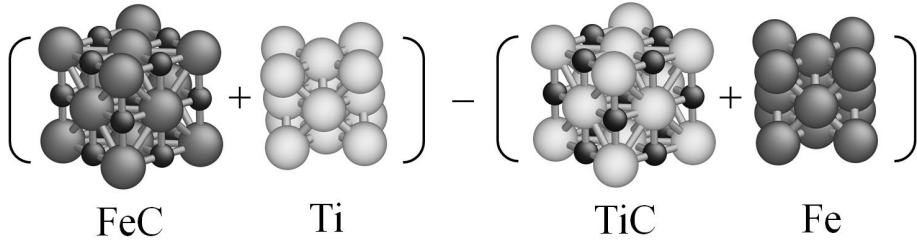


Figure 3.12: Schematic illustration for the evaluation of bond energy between Fe-C interaction and Ti-C interaction. The system energies are evaluated using *ThermoCalc* program with *TCFE6.2* database and first principles calculation.

The bond energies between C and M atoms were calculated from the formation enthalpy of the compounds using *TCFE6.2* database and first principles calculation, respectively. Fig. 3.12 shows the schematic illustration for the evaluation of bond energy between Fe-C interaction and M-C interaction. The energies are evaluated from the difference of two systems with the same number of Fe and Ti atoms. The first system is the system of combination with B1 structure FeC and FCC Ti, where all carbon atoms makes bonding with Fe atoms are calculated. The second one is the summation of the system energy of B1 structure TiC and nonmagnetic FCC Fe, where carbon atoms bonds with Ti atoms.

The atomic bond energies are evaluated as

$$\Delta H_{\text{Fe,C-M,C}} = NZ\Delta e_{\text{M-C}} \quad (3.20)$$

3.2. Interfacial Energy

Table 3.7: Calculated atomic bonding energies of $\Delta e_{\text{Fe-M}}$ and Δe_{MC} for $M = \text{Ti, Nb, V, Mo}$ and W . The first values for $\Delta e_{\text{M-C}}$ are calculated using *TCFE6.2* database and the second values are based on first principles calculation with LDA for exchange-correlation potential. The bonding energies are included in parenthesis for reference (Yang & Enomoto, 2002). The interfacial energy is calculated assumed value $p = 0.5$.

	$\Delta e_{\text{Fe-M}} / 10^{-20} \text{ J}$	$\Delta e_{\text{M-C}} / 10^{-20} \text{ J}$	$\sigma / \text{mJ m}^{-2}$
Ti	-0.707(-0.89)	7.150(T) 7.114(F) (6.2)	425
Nb	-0.361(0.02)	6.204(T) 6.039(F) (12.6)	506
V	-0.211(-0.20)	4.946(T) 5.732(F) (5.4)	445
Mo	0.392	2.843(T) 2.654(F)	374
W	0.359	2.467(T) 2.235(F)	334

where N is the number of Fe atoms in the system, $Z = 6$ is the coordination number of C atoms with nearest metal atoms. The values of $\Delta H_{\text{Fe,C-M,C}}$ for one mole of Fe and M are calculated to 258, 224, 179, 103 and 89 kJ per 1 mole of Fe and metal atoms using *TCFE6.2* database for $M = \text{Ti, Nb, V, Mo}$ and W , respectively. The molar enthalpy of MC phase has been doubled in these calculation, because the atomic fraction of metal atoms is 0.5. These values corresponds to 7.150×10^{-20} , 6.204×10^{-20} , 4.946×10^{-20} , 2.843×10^{-20} and 2.467×10^{-20} J for $\Delta e_{\text{Ti-C}}$, $\Delta e_{\text{Nb-C}}$, $\Delta e_{\text{V-C}}$, $\Delta e_{\text{Mo-C}}$ and $\Delta e_{\text{W-C}}$, respectively. The first principles calculations give 7.114×10^{-20} , 6.039×10^{-20} , 5.732×10^{-20} , 2.654×10^{-20} and 2.235×10^{-20} J for $\Delta e_{\text{Ti-C}}$, $\Delta e_{\text{Nb-C}}$, $\Delta e_{\text{V-C}}$, $\Delta e_{\text{Mo-C}}$ and $\Delta e_{\text{W-C}}$, respectively. The results from *TCFE6.2* database and first-principles calculation give a good agreement within 15% difference. The results are summarized in Table 3.7 with the referenced values.

The ratio of the first and second bond energies p is estimated to be between $3/4$ and 1 for BCC crystals (Nicholas, 1968). The values usually relatively small for FCC structure, because the bond energy is highly dependent on the separation between two atoms. Table 3.7 also also in-

3.2. Interfacial Energy

cludes the estimated values of interfacial energy with $p = 0.5$. The contribution of $\Delta e_{\text{M-C}}$ for the interface between ferrite and $\text{MoC}_{0.5}$ or $\text{WC}_{0.5}$ has been reduced to half since the carbon atomic fraction is 0.5. The estimated interfacial energies are 481, 556, 485, 386 and 346 mJ m^{-2} for TiC, NbC, VC, $\text{MoC}_{0.5}$ and $\text{WC}_{0.5}$, respectively. These values contain not only chemical bonding, but also structural strain energy, since the thermodynamic databases are obtained from experimental observation. The first-principles calculation results are 493, 339 and 280 mJ m^{-2} for TiC, $\text{MoC}_{0.5}$ and $\text{WC}_{0.5}$, respectively, assumed that the interfacial energy are evaluated from the direct sum of σ_s and σ_c . These are matched well with results from thermodynamic databases. However, the values for NbC and VC are different from the first-principles calculations since the contribution of σ_s do not need to be identical for all carbides. Another important point is that the thermodynamic data are based on enclosed particles whereas the first-principles calculations on just one plane.

3.2.3 (Ti,Mo)C Coarsening

The results from the present calculation combined with the theory describing coarsening of particles suggest a possible effect of molybdenum on retarding the coarsening of TiC particles. According to Ostwald's ripening theory:

$$\bar{r}(t)^n - \bar{r}(0)^n = \frac{8 \sigma V_m^2 DC}{9 RT} t \quad (3.21)$$

where t is time, \bar{r} is the average radius of all the particles, σ is interfacial energy per unit area between particles and matrix, D is diffusion coefficient of the particle element which controls coarsening process and V_m is the molar volume of the particle (Wagner, 1961).

Even with the positive influence of Mo on the nucleation of (Ti,Mo)C precipitates regarding the interface energy, its presence in (Ti,Mo)C is not energetically favorable in terms of the formation energy. As mentioned, this suggests that Mo atoms participate in the precipitation of (Ti,Mo)C

carbide only during the very early stages of evolution through its role in reducing interfacial energy, when the surface to volume ratio of particle is considerable, but subsequent coarsening should be controlled by the diffusion of Ti atoms. This interpretation accords with a previous report that the Mo concentration in (Ti,Mo)C decreased as the particles grew during the subsequent process (Seto *et al.*, 2007). Then the partial replacement of Ti by Mo in alloy design will reduce the equilibrium concentration of Ti in the ferrite matrix at the commencement of coarsening. In the same context, a similar effect is expected for W substitution for Ti because the W atom in TiC will reduce the lattice mismatch between the precipitate and the matrix, but increase the formation energy.

3.3 Model Alloys

First-principles calculation and interfacial energy calculation results in the present study show the influence of replacement of Ti by M on the formation and lattice parameter of (Ti,M)C carbides. This suggests that the thermal stability of (Ti,Mo)C against coarsening is possibly attributed to the reduction in misfit strain at the interface with the ferrite matrix, which encourages the participation of Mo with the precipitate at an earlier stage, even with an unfavorable effect regarding the formation energy, as well as a decrease in the Ti content in the matrix, of which diffusion is believed to be critical for coarsening. The calculation implies that W will play a similar role to Mo. Here, micro-structural characterization is conducted in Ti-, Ti-Mo- and Ti-W-bearing steels to validate the calculation results.

3.3.1 Experimental Procedures

The chemical compositions of the investigated alloys are presented in Table 3.8. Based on the 0.04C-0.2Ti alloy, where the ratio of Ti to C is intended to consume most of the carbon to form TiC, half of the Ti is

3.3. Model Alloys

Table 3.8: Chemical composition of 0.1Ti, 0.2Ti, 0.1Ti+Mo and 0.1Ti+W steels (in wt%).

type	C	Mn	Al	Ti	Mo	W
0.1Ti	0.041	1.98	0.030	0.080	-	-
0.2Ti	0.034	2.00	0.024	0.207	-	-
0.1Ti+Mo	0.039	1.99	0.022	0.084	0.2	-
0.1Ti+W	0.040	2.01	0.024	0.095	-	0.39

Table 3.9: Calculated equilibrium phase mole fraction for ferrite(BCC), cementite and MC-type carbide at 630°C. c_M^{MC} indicates the atomic fraction of Mo or W in (Ti,M)C carbide. Carbon atomic fraction in cementite and MC carbide are included in the parenthesis.

type	BCC	cementite / $\times 10^{-3}$	MC / $\times 10^{-3}$	c_M^{MC}
0.1Ti	0.9948	3.342(0.25)	1.860(0.496)	-
0.2Ti	0.9966	-	3.383(0.466)	-
0.1Ti+Mo	0.9955	2.391(0.25)	2.162(0.494)	0.049
0.1Ti+W	0.9961	0.768(0.25)	3.092(0.495)	0.145

reduced or replaced with Mo and W to form 0.04C-0.1Ti, 0.04C-0.1Ti-0.2Mo and 0.04C-0.1Ti-0.4W alloys, according to the stoichiometry. The calculated equilibrium mole fraction of ferrite, cementite and MC-type carbide at 630°C are listed in Table 3.9 using *ThermoCalc* software with *TCFE6.2* database. In 0.2Ti alloy, all the carbon atoms are consumed to form TiC carbide, hence no cementite are formed. The equilibrium atomic fraction of Mo and W in (Ti,M)C are smaller than the Ti atomic fraction, though the amount of total Mo or W in the whole system are larger than those of Ti.

The alloy were prepared as 30 kg ingots by vacuum induction melting, then hot rolled into 20 mm plates. Cylindrical specimens with a diameter of 5 mm and a length of 10 mm were machined and subjected to the heat

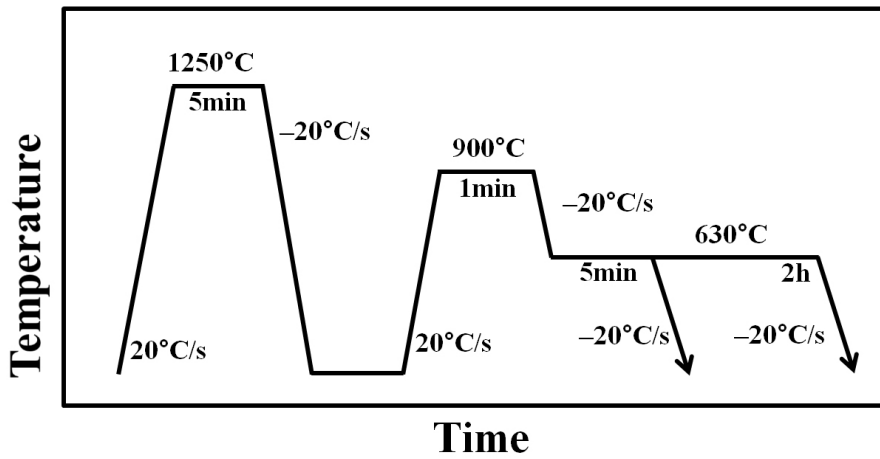


Figure 3.13: Schematic diagram showing the two-step heat-treatment. The first heating temperature, 1250°C , is determined to resolve TiC precipitation and the second heating temperature and time are determined to control the austenite grain size. The ageing temperature, 630°C , is the temperature which corresponds to the ferrite transformation nose. Prolonged ageing time is designed to check the effect of the coarsening process.

treatment cycle in Fig. 3.13 using a quench dilatometer. The specimens were heated to 1250°C for 300 s to dissolve pre-existing precipitation, followed by rapid cooling to ambient temperature. In the second heating, the specimens were austenitized at 900°C for 60 s to control the austenite grain size, then cooled to 630°C, which corresponds to the nose temperature of ferrite transformation. The nose temperature was determined by dilatometric experiments in the temperature range from 600°C to 700°C, with 10°C intervals. The transformation from austenite to ferrite was completed within 300 s at the nose temperature for all specimens. A prolonged ageing for 2 h was performed to examine the coarsening of (Ti,M)C carbide.

A cross section along the longitudinal direction of the dilatometric specimen was observed using a light microscope with 2% nital solution. The detailed microstructure of the (Ti,M)C precipitates was analyzed by TEM using a microscope equipped for energy-dispersive X-ray spectroscopy (EDS). The quantification of titanium, molybdenum and tungsten fraction in carbides has been conducted without allowing for carbon in EDS results. For the preparation of thin foil specimens, the standard method of mechanical polishing and electrolytic thinning with 5% perchloric acid 95% acetic acid solution followed by a precision ion milling was adopted. The hardness of the specimen was measured by the Vickers hardness test with a load of 3 kg.

3.3.2 Optical Microscopy

Figs 3.14 and 3.15 present optical micrographs of investigated alloys after 5 min and 2 h of ageing at 630°C, respectively. At the resolution level of the optical microscope, the microstructure of the 0.2Ti alloy is seen to be single-phase ferrite. However, it is interesting to note that the microstructures of the 0.1Ti, 0.1Ti+Mo and 0.1Ti+W alloys consist of ferrite matrix with a little cementite. This indicates that the carbon is fully consumed to form a precipitate in the 0.2Ti alloy but not in the

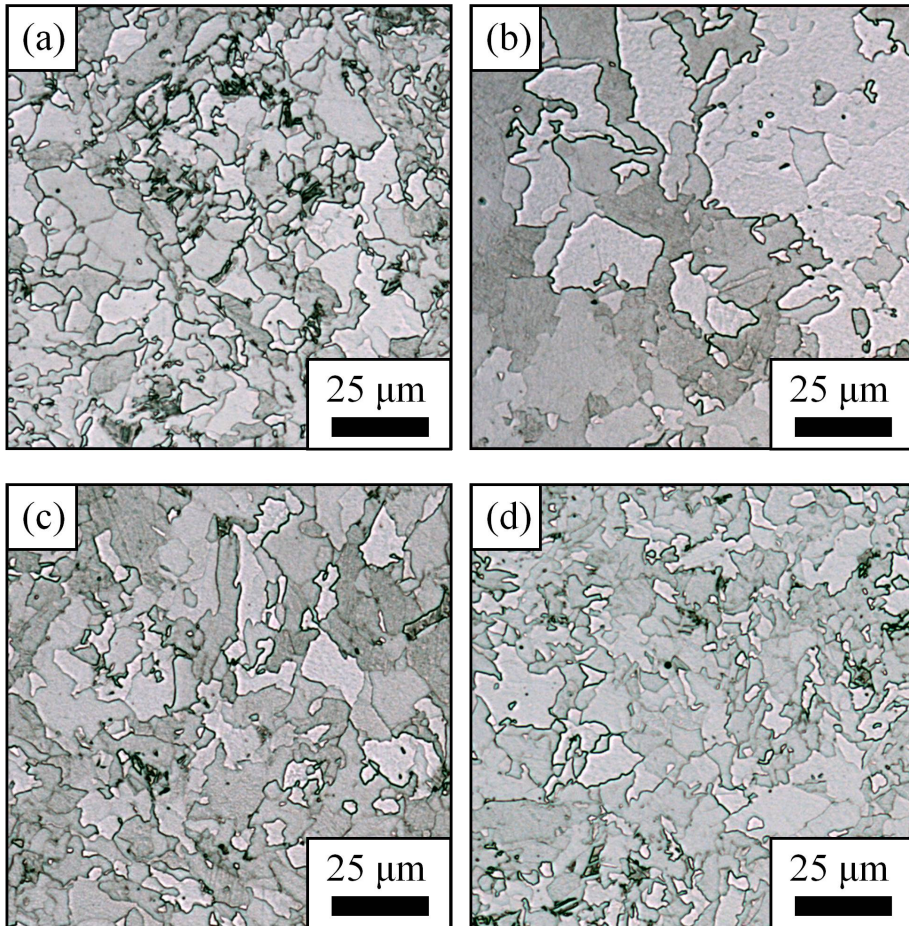


Figure 3.14: Optical microscopy images for the samples after 5 min of ageing of (a) 0.1Ti (b) 0.2Ti (c) 0.1Ti+Mo and (d) 0.1Ti+W. The samples were etched for about 20 s with a 2% nital solution. The samples are a mixture of ferrite matrix and cementite while 0.2Ti contains almost all ferrite matrix.

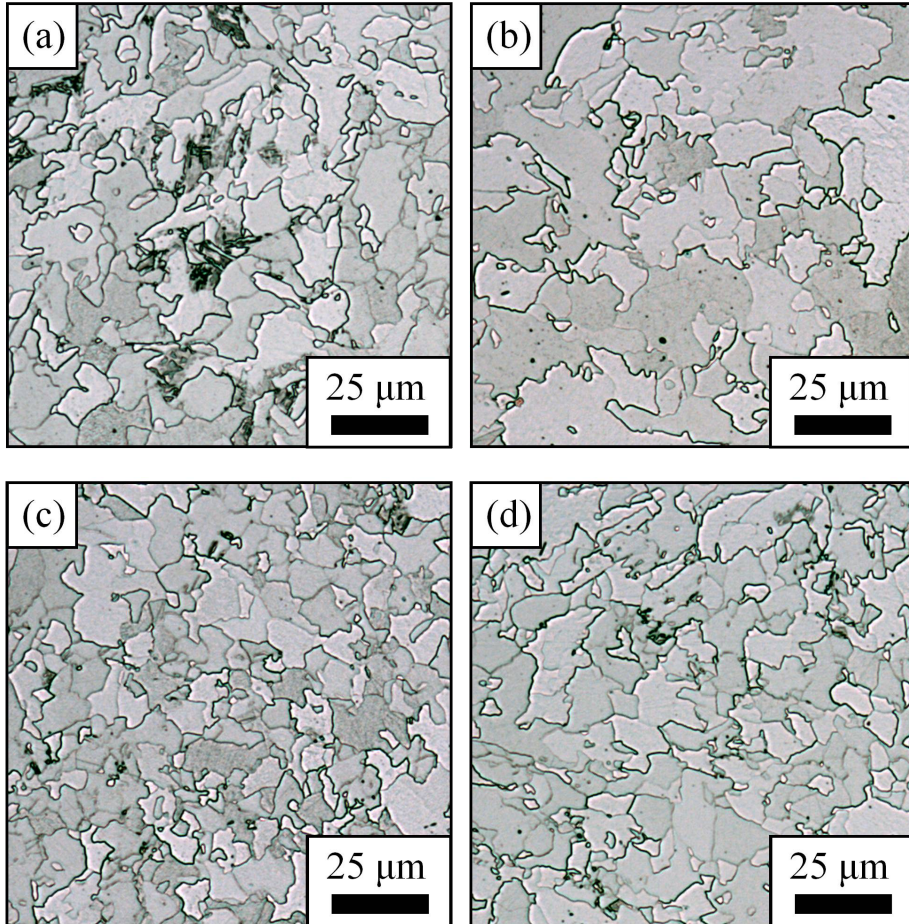


Figure 3.15: Optical microscopy images for the samples after 2 h of ageing of (a) 0.1Ti (b) 0.2Ti (c) 0.1Ti+Mo and (d) 0.1Ti+W. The samples were etched for about 20 s with a 2% nital solution. The samples are a mixture of ferrite matrix and cementite while 0.2Ti contains almost all ferrite matrix.

0.1Ti, 0.1Ti+Mo and 0.1Ti+W alloys. This is actually in accord with the first-principles calculation indicating that MoC and WC with a B1 structure favor the introduction of a certain fraction of vacancies into the carbon position.

Even though the precipitates in the 0.1Ti+Mo and 0.1Ti+W alloys are (Ti,Mo)C and (Ti,W)C carbides, the Mo or W in the (Ti,M)C carbides is likely to favor the partial replacement of carbon with vacancies, leading to an increase in solute carbon concentration to form cementite. However, it is also possible that the presence of cementite originates from the disadvantage regarding the formation energy of (Ti,Mo)C of (Ti,W)C, which leads to insufficient precipitation in 0.1Ti+Mo and 0.1Ti+W alloys to exhaust the solute carbon.

3.3.3 0.1Ti Alloy

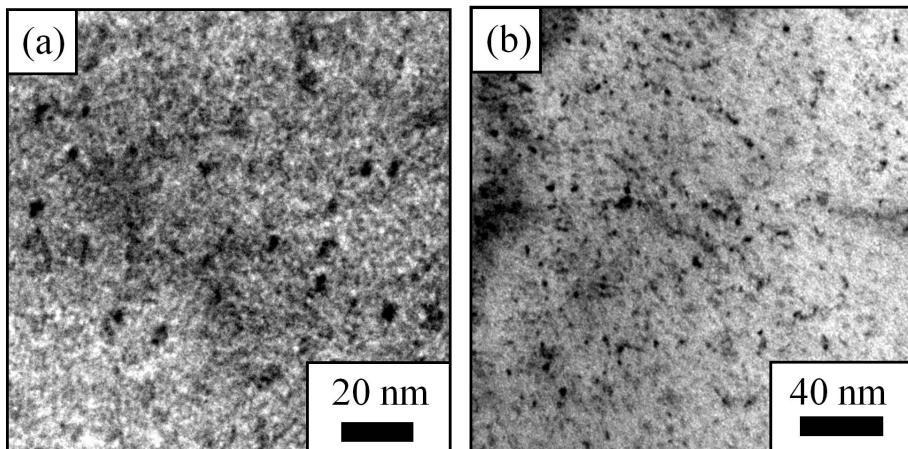


Figure 3.16: TEM bright filed images of 0.1Ti steel after 2 h ageing with (a) high and (b) low magnification showing carbides.

Figs 3.16 and 3.17 present TEM and annular dark field scanning TEM (STEM) images of the precipitates in the 0.1Ti alloys after 2 h

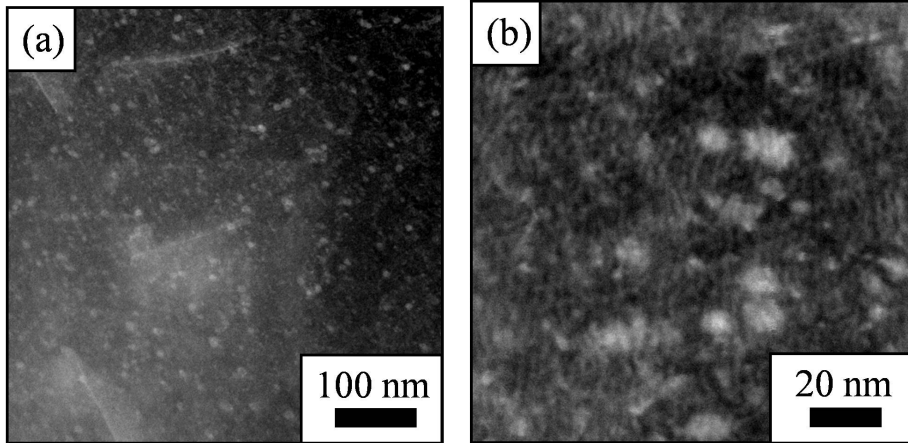


Figure 3.17: Annular dark field STEM images of the 0.1Ti samples after for 2 h with (a) low and (b) high magnification showing carbides.

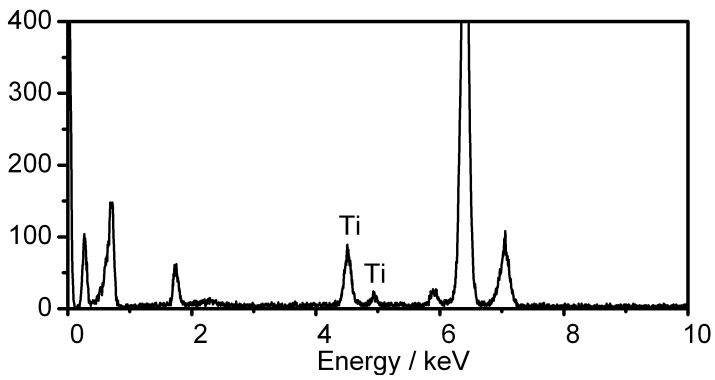


Figure 3.18: Characteristic EDS spectra of the TiC carbides of 0.1Ti steels in Fig. 3.17(b) after 2 h ageing.

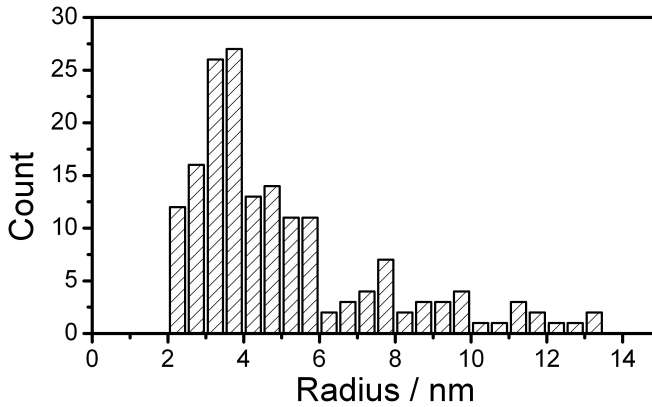


Figure 3.19: Relative frequency as a function of particle radius of TiC particles in 0.1Ti steel after 2 h ageing measured using Fig. 3.17(a). The mean value and standard deviation of radius are 5.5 nm and 3.8 nm, respectively.

ageing. Fig. 3.18 is the result of characteristic EDS spectra of TiC carbides with about 5 nm radius shown in Fig. 3.17(b). The other peaks without indexing come from matrix. Fig. 3.19 shows the distribution of particle radii for TiC particles, as obtained from annular dark field STEM image. The measured mean values and standard deviations of particle radius are 5.5 nm and 3.8 nm, respectively.

3.3.4 0.2Ti Alloy

Fig 3.20 shows bright field and annular dark field (STEM) images of the TiC carbides in the 0.2Ti alloys after 2 h ageing. Fig 3.21 is the results of characteristic EDS spectra of TiC carbides with about 6 nm radius shown in Fig. 3.20(b). Fig. 3.22 shows the distribution of particle radii for TiC particles, as obtained from the annular dark field STEM image. The measured mean values and standard deviations of particle radius are 6.4 nm and 4.0 nm, respectively. Fig. 3.23 represents high

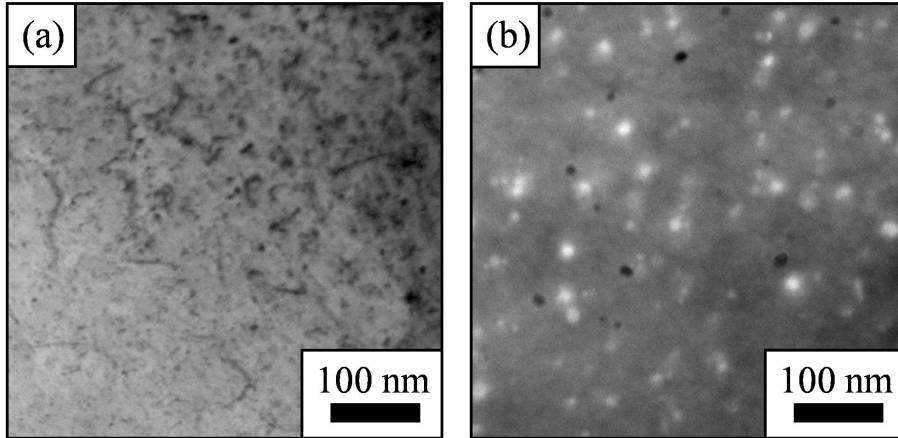


Figure 3.20: (a) Bright field and (b) annular dark field STEM images of the 0.2Ti samples after for 2 h showing carbides.

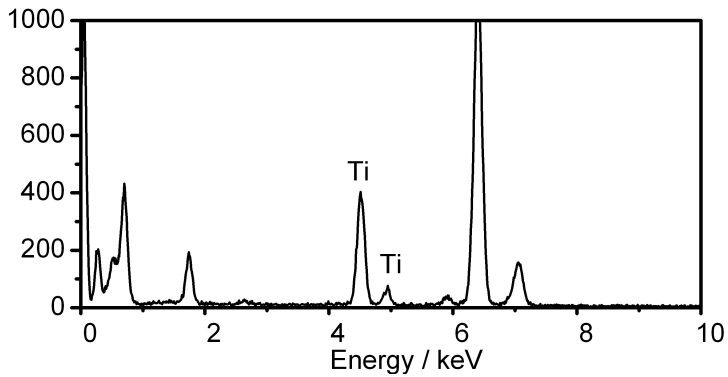


Figure 3.21: Characteristic EDS spectra of the TiC carbides in Fig. 3.20(b) of 0.2Ti steels after 2 h ageing.

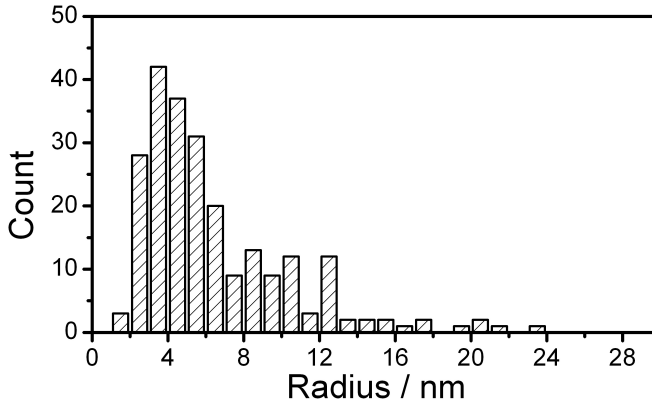


Figure 3.22: Relative frequency as a function of particle radius of TiC particles in 0.2Ti steel after 2 h ageing measured using Fig. 3.20(b). The mean value and standard deviation of radius are 6.4 nm and 4.0 nm, respectively.

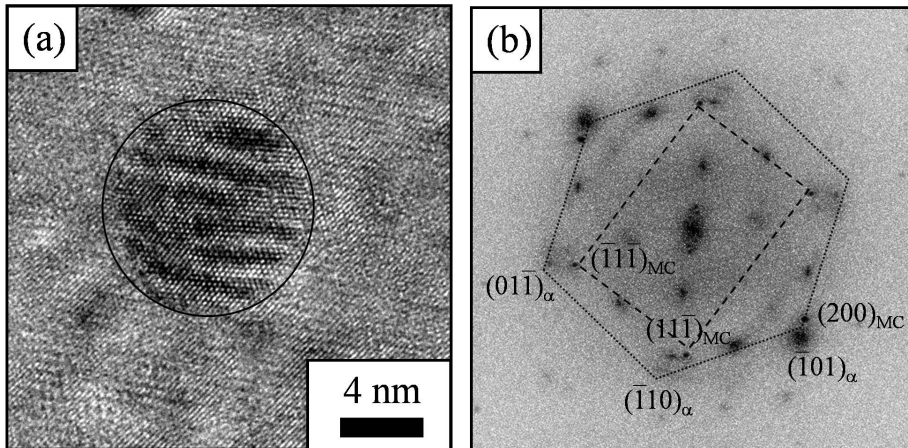


Figure 3.23: (a) HRTEM image of a 0.2Ti sample showing TiC carbide and (b) its fast Fourier transform image along the $[111]_{\alpha}$ and $[011]_{MC}$ zone axis, which corresponds to the Baker-Nutting orientation relationship.

resolution TEM (HRTEM) image of a 0.2Ti sample showing TiC carbide and its fast Fourier transform image along the $[111]_{\alpha}$ and $[011]_{MC}$ zone axes, which corresponds to the Baker-Nutting orientation relationship. The lattice misfit between the TiC particles and the ferrite matrix along the interface are measured to be 6.9%. The lattice misfit was evaluated measuring the lattice distance with $[\bar{1}01]_{\alpha}$ and $[200]_{MC}$ directions.

3.3.5 0.1Ti+Mo Alloy

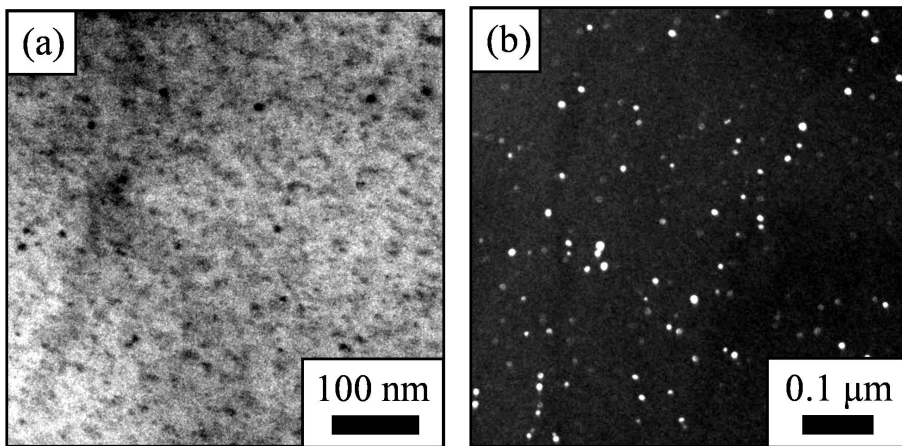


Figure 3.24: (a) Bright field and (b) dark field TEM images of 0.1Ti+Mo steel after 2 h ageing showing carbides.

Fig. 3.24 presents bright field and dark field TEM images showing (Ti,Mo)C carbides in the 0.1Ti+Mo alloys after 2 h ageing. Fig. 3.25 shows the bright field STEM images. Fig. 3.26 is the results of characteristic EDS spectra of (Ti,Mo)C carbides with about 5 nm radius shown in Fig. 3.25(b). It is estimated to contain 42 ± 4.7 wt% Ti and 58 ± 4.7 wt% Mo, respectively. Fig. 3.27 includes the distribution of particle radii for (Ti,Mo)C particles, as obtained from dark field TEM image. The measured mean values and standard deviations of particle radius are 4.3 nm

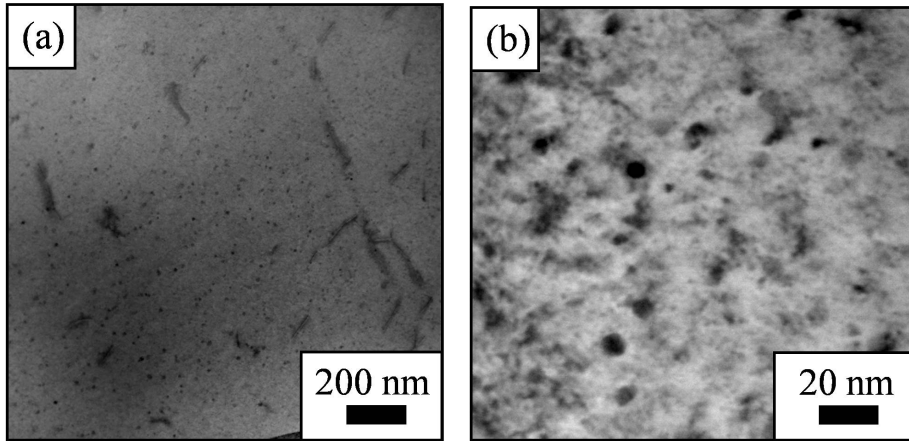


Figure 3.25: Bright field STEM images of the 0.1Ti+Mo samples after for 2 h with (a) low and (b) high magnification showing (Ti,Mo)C carbides.

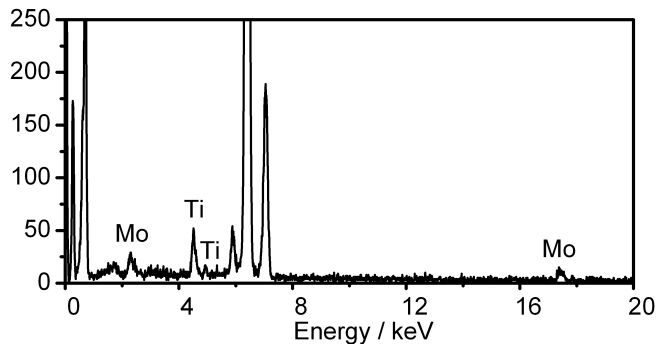


Figure 3.26: Characteristic EDS spectra of the (Ti,Mo)C carbides in Fig. 3.25(b) of 0.1Ti+Mo steels after 2 h ageing. It is estimated to contain 42(60 at%) \pm 4.7 wt% Ti and 58(40 at%) \pm 4.7 wt% Mo, respectively.

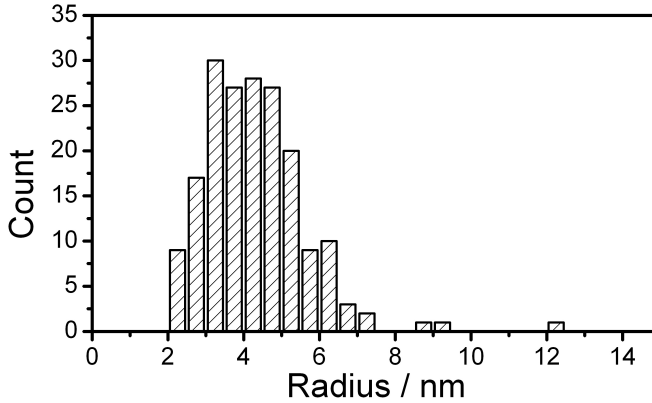


Figure 3.27: Relative frequency as a function of particle radius of (Ti,Mo)C particles in 0.1Ti+Mo steel after 2 h ageing measured using Fig. 3.24(b). The mean value and standard deviation of radius are 4.3 nm and 1.5 nm, respectively.

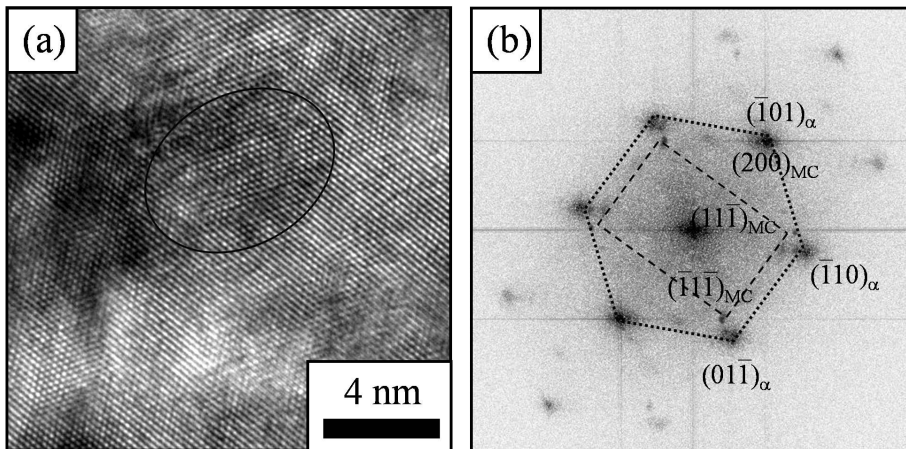


Figure 3.28: (a) HRTEM image of 0.1Ti+Mo sample showing (Ti,Mo)C carbide and (b) its fast Fourier transform image along the $[111]_{\alpha}$ and $[011]_{MC}$ zone axis, which corresponds to the Baker-Nutting orientation relationship.

and 1.5 nm, respectively. Fig. 3.28 represents HRTEM image of 0.1Ti+Mo sample showing carbide and its fast Fourier transform image along the $[111]_{\alpha}$ and $[011]_{MC}$ zone axis. The lattice misfit between the (Ti,Mo)C particles and the ferrite matrix along $(101)_{\alpha}$ and $(200)_{MC}$ directions was measured to be 4.8%.

3.3.6 0.1Ti+W Alloy

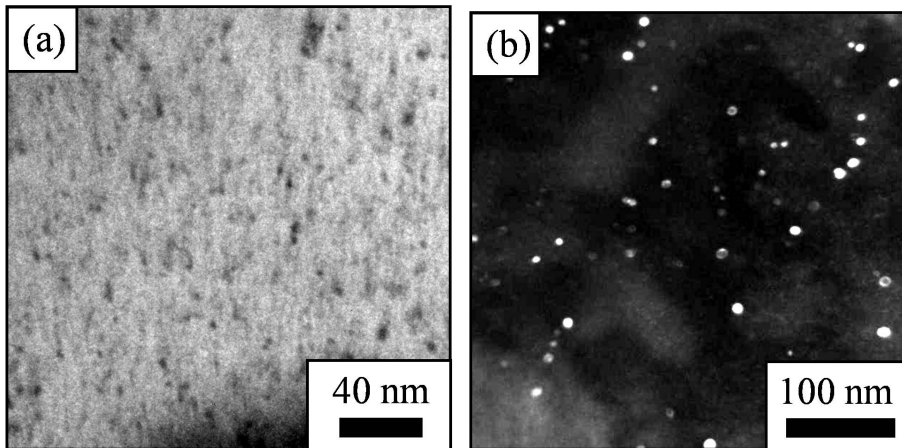


Figure 3.29: (a) Bright field and (b) dark field TEM images of 0.1Ti+W steel after 2 h ageing showing carbides.

Fig. 3.29 presents bright field and dark field TEM images showing (Ti,W)C carbides in the 0.1Ti+W alloys after 2 h ageing. Fig. 3.30 shows the bright field and annular dark field STEM images. Fig. 3.31 is the results of characteristic EDS spectra of (Ti,W)C carbides with about 5 nm radius shown in Fig. 3.30(a). It is estimated to contain 33 ± 2.4 wt% Ti and 66 ± 2.4 wt% W, respectively. The distribution of particle radii for (Ti, W)C particles, as obtained from dark field TEM image, is presented in Fig. 3.32. The measured mean values and standard deviations of particle radius are 4.8 nm and 2.4 nm, respectively. Fig. 3.33 represents HRTEM

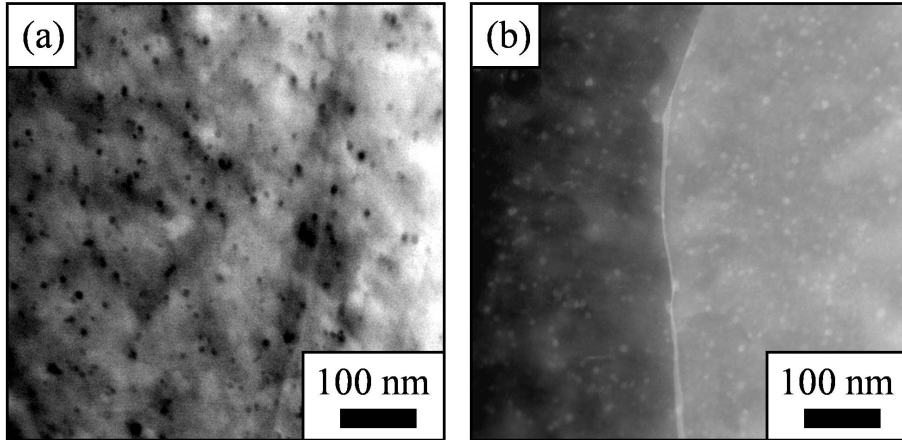


Figure 3.30: (a) Bright field and (b) annular dark field STEM images of the 0.1Ti+W samples after for 2 h showing (Ti,W)C carbides

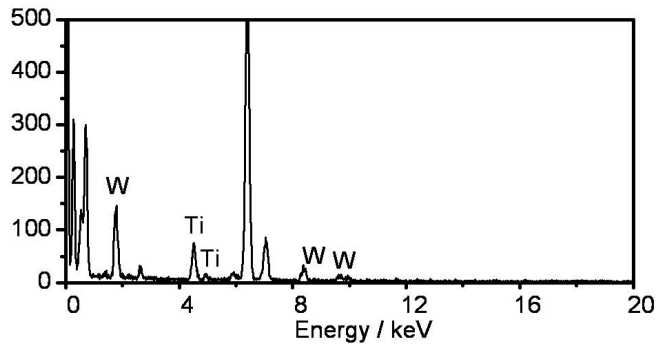


Figure 3.31: Characteristic EDS spectra of the (Ti,W)C carbides in Fig. 3.30(a) of 0.1Ti+W steels after 2 h ageing. It is estimated to contain 33(67 at%) \pm 2.4 wt% Ti and 66(33 at%) \pm 2.4 wt% W, respectively.

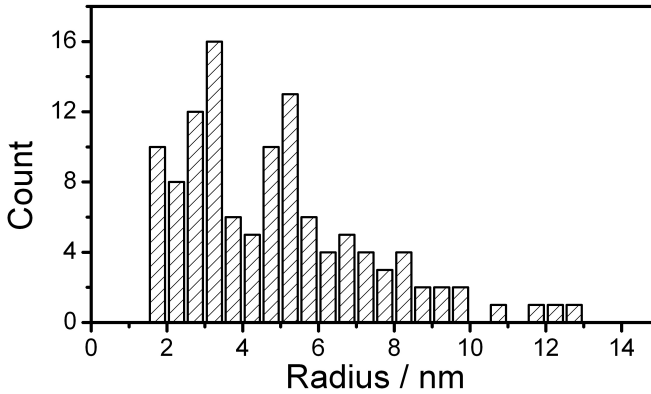


Figure 3.32: Relative frequency as a function of particle radius of (Ti,W)C particles in 0.1Ti+W steel after 2 h ageing measured using Fig. 3.29(b). The mean value and standard deviation of radius are 4.8 nm and 2.4 nm, respectively.

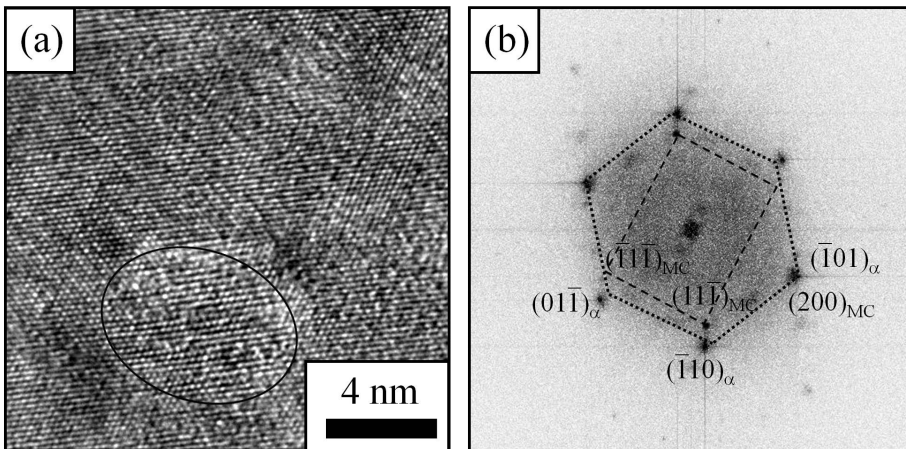


Figure 3.33: (a) HRTEM image of 0.1Ti+W sample showing (Ti,W)C carbide and (b) its fast Fourier transform image along the $[111]_{\alpha}$ and $[011]_{MC}$ zone axis, which corresponds to the Baker-Nutting orientation relationship.

image of 0.1Ti+W sample showing carbide and its fast Fourier transform image along the $(101)_\alpha$ and $(200)_{MC}$ directions was measured to be 5.2%.

3.3.7 Comparison

The particle size of 0.2Ti alloy is 18%, 48% and 33% bigger than that of 0.1Ti, 0.1Ti+Mo and 0.1Ti+W alloys, respectively. This reflects the effect of Mo on the retardation of coarsening of nano-sized carbide reported elsewhere (Seto *et al.*, 2007). It should also be noted that there is comparable effect of tungsten on the coarsening kinetics, as predicted by first-principles calculation.

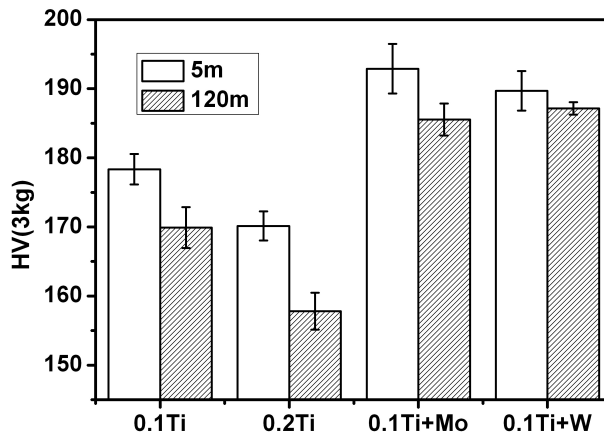


Figure 3.34: Vickers hardness results for 0.1Ti, 0.2Ti, 0.1Ti+Mo and 0.1Ti+W after ageing for 5 and 120 min, respectively. The hardness was measured using 3 kg loads.

Fig. 3.34 summarizes the Vicker's hardness of the 0.1Ti, 0.2Ti, 0.1Ti+Mo and 0.1Ti+W alloys subjected to ageing for 5 and 120 min. The hardness of the alloys decreases with prolonged ageing, the decrements being 8, 12, 6 and 2 HV for the 0.1Ti, 0.2Ti, 0.1Ti+Mo and 0.1Ti+W alloys, respec-

tively. As expected from the size of the precipitates, the decrement in the hardness of the 0.2Ti alloy is the most remarkable, being more than twice as large as those of the 0.1Ti+Mo and 0.1Ti+W alloys. On the other hand, the influence of prolonged ageing on the change in hardness is the least in the 0.1Ti+W alloy, suggesting that the addition of W effectively suppress the deterioration in strength mainly caused by the coarsening of the nano-sized precipitates.

The hardness of the 0.1Ti+Mo and 0.1Ti+W alloys is higher than that of 0.2Ti alloy even with only 5 min of ageing. Given that the fine precipitation contributes primarily to the strength of this class of alloy, this suggests the precipitation hardening in the 0.1Ti+Mo and 0.1Ti+W alloys is comparable to that in the 0.2Ti alloy. This implies that the deficient precipitation due to the unfavorable formation energy of (Ti,Mo)C and (Ti,W)C will have a minor effect on the presence of cementite in the 0.1Ti+Mo and 0.1Ti+W alloys as shown in Figs 3.14 and 3.15.

Figs. 3.28 and 3.33 show HRTEM images of approximately 3 nm sized (Ti,M)C particles in 0.1Ti+Mo and 0.1Ti+W alloys. Their fast Fourier transformed patterns, indexed with $[111]_{\alpha}$ and $[011]_{MC}$ zone axis, indicate a Baker-Nutting orientation relationship with $(\bar{1}01)_{\alpha} || (200)_{MC}$. The lattice misfits between the (Ti,Mo)C and (Ti,W)C carbide particles and the ferrite matrix along the interface are measured to be 4.8 and 5.2%, respectively. For TiC precipitations, the measured misfit is about 6.9%.

These corresponds to lattice parameters of 4.254, 4.270 and 4.338 Å for (Ti,Mo)C, (Ti,W)C and TiC by adopting a fixed lattice parameter of ferrite as 2.87 Å. The observed lattice parameter of (Ti,Mo)C particle matches well with that found in a previous study, which was reported as 4.23 ~ 4.30 Å (Yen *et al.*, 2009). Even though a few precipitates were analyzed in the present study, the observations from three investigated alloys shows that the lattice mismatch between carbide and ferrite matrix can be relaxed by substitution of Ti by Mo or W in (Ti,M)C carbide. As mentioned, this will be desired in the early stage of precipitation when

the surface to volume ratio is high to compensate the disadvantage with respect to the formation energy.

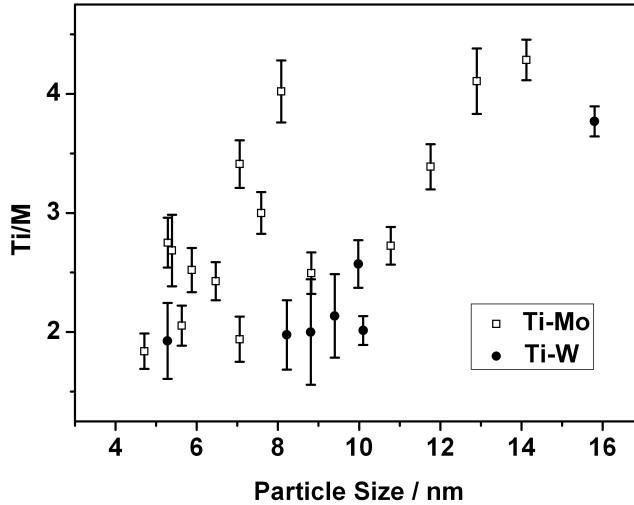


Figure 3.35: Substitutional site fraction dependency on precipitation size in (Ti,M)C. The precipitation sizes are measured using STEM images and chemical compositions are obtained using an EDS system. The blank rectangles and solid circles represent the Ti/Mo and Ti/W site fractions, respectively.

Finally, Fig. 3.35 shows the atomic ratio of Ti to Mo or W in (Ti,M)C particles as a function of the diameter. The rectangles and solid circles represent Ti/Mo and Ti/W fraction, respectively. It can be seen that the atomic fraction of Ti gradually increases in both the (Ti,Mo)C and (Ti,W)C precipitates. A similar trend is reported in an earlier study for (Ti,Mo)C particles (Seto *et al.*, 2007). This suggests that it is the diffusion of Ti that mainly controls the coarsening process and that Mo or W have more passive contributions during the coarsening itself.

References

- AARONSON, H., LEE, J. & RUSSELL, K. (1978). Precipitation processes in solids. In *Conference Proceeding of the Metallurgical Society of AIME, Warrendale, PA*, 31. 89
- ANDE, C. & SLUITER, M. (2010). First-principles prediction of partitioning of alloying elements between cementite and ferrite. *Acta Materialia*, **58**, 6276–6281. 79
- BECKER, R. (1938). Die keimbildung bei der ausscheidung in metallischen mischkristallen. *Annalen der Physik*, **424**, 128–140. 96
- CHRISTIAN, J. (2002). *The Theory of Transformations in Metals and Alloys: Part I+ II.* Elsevier. 89
- CHUNG, S., HA, H., JUNG, W. & BYUN, J. (2006). An ab initio study of the energetics for interfaces between group V transition metal carbides and bcc iron. *ISIJ International*, **46**, 1523–1531. 96
- CSONKA, G., PERDEW, J., RUZSINSZKY, A., PHILIPSEN, P., LEBÈGUE, S., PAIER, J., VYDROV, O. & ÁNGYÁN, J. (2009). Assessing the performance of recent density functionals for bulk solids. *Physical Review B*, **79**, 155107. 80
- DREGIA, S. & WYNBLATT, P. (1991). Equilibrium segregation and interfacial energy in multicomponent systems. *Acta Metallurgica et Materialia*, **39**, 771–778. 96
- HUGOSSON, H., ERIKSSON, O., JANSSON, U. & JOHANSSON, B. (2001a). Phase stabilities and homogeneity ranges in 4d-transition-metal carbides: A theoretical study. *Physical Review B*, **63**, 134108. 82
- HUGOSSON, H., JANSSON, U., JOHANSSON, B. & ERIKSSON, O. (2001b). Phase stability diagrams of transition metal carbides, a theoretical study. *Chemical Physics Letters*, **333**, 444–450. 87

REFERENCES

- ISAEV, E., SIMAK, S., ABRIKOSOV, I., AHUJA, R., VEKILOV, Y., KATSNELSON, M., LICHTENSTEIN, A., JOHANSSON, B. *et al.* (2007). Phonon related properties of transition metals, their carbides, and nitrides: A first-principles study. *Journal of applied physics*, **101**, 123519–123519. [82](#), [83](#)
- JUNG, W., LEE, S. & CHUNG, S. (2008). Energetics for interfaces between group IV transition metal carbides and bcc iron. *ISIJ International*, **48**, 1280–1284. [95](#)
- LEE, I. & MARTIN, R. (1997). Applications of the generalized-gradient approximation to atoms, clusters, and solids. *Physical Review B*, **56**, 7197. [80](#)
- MACKENZIE, J., MOORE, A. & NICHOLAS, J. (1962). Bonds broken at atomically flat crystal surfaces I: Face-centred and body-centred cubic crystals. *Journal of Physics and Chemistry of Solids*, **23**, 185–196. [96](#)
- MANNSTADT, W. & FREEMAN, A. (1997). Dynamical and geometrical aspects of NO chemisorption on transition metals: Rh, Pd, and Pt. *Physical Review B*, **55**, 13298. [79](#)
- MONKHORST, H. & PACK, J. (1976). Special points for Brillouin-zone integrations. *Physical Review B*, **13**, 5188–5192. [78](#)
- NICHOLAS, J. (1968). Calculation of surface energy as a function of orientation for cubic crystals. *Australian Journal of Physics*, **21**, 21–34. [101](#)
- ONINK, M., BRAKMAN, C., TICHELAAR, F., MITTEMEIJER, E., VAN DER ZWAAG, S., ROOT, J. & KONYER, N. (1993). The lattice parameters of austenite and ferrite in Fe-C alloys as functions of carbon concentration and temperature. *Scripta Metallurgica et Materialia*, **29**, 1011–1011. [98](#)

REFERENCES

- PERDEW, J., BURKE, K., WANG, Y. *et al.* (1996). Generalized gradient approximation for the exchange-correlation hole of a many-electron system. *Physical Review-Section B-Condensed Matter*, **54**, 16533–16539. [78](#)
- RAMANUJAN, R., LEE, J. & AARONSON, H. (1992). A discrete lattice plane analysis of the interfacial energy of coherent FCC: HCP interfaces and its application to the nucleation of [gamma] in Al–Ag alloys. *Acta Metallurgica et Materialia*, **40**, 3421–3432. [96](#)
- SETO, K., FUNAKAWA, Y. & KANEKO, S. (2007). Hot rolled high strength steels for suspension and chassis parts ‘NANOHITEN’ and ‘BHT Steel’. *JFE Technical Report*, 19–25. [95](#), [103](#), [120](#), [122](#)
- SHAHANDEH, S. & NATEGH, S. (2007). A computational thermodynamics approach to the Gibbs–Thomson effect. *Materials Science and Engineering: A*, **443**, 178–184. [89](#)
- STAMPFL, C., MANNSTADT, W., ASAH, R. & FREEMAN, A. (2001). Electronic structure and physical properties of early transition metal mononitrides: Density-functional theory LDA, GGA, and screened-exchange LDA FLAPW calculations. *Physical Review B*, **63**, 155106. [83](#)
- STEINLE-NEUMANN, G., STIXRUDE, L. & COHEN, R. (1999). First-principles elastic constants for the hcp transition metals Fe, Co, and Re at high pressure. *Physical Review B*, **60**, 791. [80](#)
- TERESIAK, A. & KUBSCH, H. (1995). X-ray investigations of high energy ball milled transition metal carbides. *Nanostructured Materials*, **6**, 671–674. [78](#), [82](#)
- WAGNER, C. (1961). Theory of precipitate change by redissolution. *Electrochimie*, **65**, 581–591. [102](#)

REFERENCES

- WEINERT, M., WIMMER, E. & FREEMAN, A. (1982). Total-energy all-electron density functional method for bulk solids and surfaces. *Physical Review B*, **26**, 4571. [78](#)
- WIMMER, E., KRAKAUER, H., WEINERT, M. & FREEMAN, A. (1981). Full-potential self-consistent linearized-augmented-plane-wave method for calculating the electronic structure of molecules and surfaces: O₂ molecule. *Physical Review B*, **24**, 864. [78](#)
- YANG, Z. & ENOMOTO, M. (1999). A discrete lattice plane analysis of coherent fcc/B1 interfacial energy. *Acta Materialia*, **47**, 4515–4524. [96](#)
- YANG, Z. & ENOMOTO, M. (2001). Calculation of the interfacial energy of B1-type carbides and nitrides with austenite. *Metallurgical and Materials Transactions A*, **32**, 267–274. [96](#), [98](#)
- YANG, Z. & ENOMOTO, M. (2002). Discrete lattice plane analysis of Baker–Nutting related B1 compound/ferrite interfacial energy. *Materials Science and Engineering: A*, **332**, 184–192. [96](#), [101](#)
- YEN, H., HUANG, C. & YANG, J. (2009). Characterization of interphase-precipitated nanometer-sized carbides in a Ti–Mo-bearing steel. *Scripta Materialia*, **61**, 616–619. [121](#)
- ZENER, C. (1949). Theory of growth of spherical precipitates from solid solution. *Journal of Applied Physics*, **20**, 950–953. [89](#)

Chapter 4

Coarsening

Coarsening is a process, which has been observed in a large number of systems where particles of various sizes are dispersed in a matrix. It involves the growth of large particles at the expense of smaller ones. The driving force of this process is the decrease in total interfacial energy within the sample. The coarsening process is especially interesting for Ti and Mo added HSLA steels, because the thermal stability of (Ti,Mo)C during coiling of sheet steel at a high temperature determines the precipitate strengthening effect. A large number of studies have been conducted to study the coarsening behavior of carbides in steels. The purpose of this chapter is to analyze and compare the coarsening rate of TiC precipitates in a ferrite matrix by applying three models: (1) Lifshitz, Slyozov and Wagner (LSW) theory (Lifshitz & Slyozov, 1961; Wagner, 1961). (2) Software which deals with multi-component diffusion controlled transformations (DICTRA) (Andersson & Agren, 1992) and (3) Kampmann and Wagner's numerical (KWN) approach (Samaras, 2006).

All models use the assumption that the systems contain spherical precipitates with the particle size distribution from LSW theory corresponding to an average particle radius of 2.0 nm. Calculations have been conducted to simulate 0.2Ti-0.04C wt% system aged at 700°C for 1.0×10^5 s.

4.1. Lifshitz, Slyozov and Wagner Model

The interfacial energy between ferrite and TiC particles was assumed to be 493, 339 or 200 mJ m⁻², as obtained for TiC and MoC phases in the first-principles calculations included in the previous chapter. Systems with 0.18Ti-0.04C and 0.15Ti-0.04C wt% also have been analyzed to show the effect of titanium dissolved in the matrix.

4.1 Lifshitz, Slyozov and Wagner Model

One of the outcomes of the LSW theory is the dependence of particle radius on time (Lifshitz & Slyozov, 1961; Wagner, 1961):

$$\bar{r}(t)^n - \bar{r}(0)^n = \frac{8}{9} \frac{\sigma V_m^2 D C_e}{RT} t = Kt \quad (4.1)$$

where K is the coarsening rate constant, t is time, \bar{r} is the average particle radius, σ is the particle/matrix interfacial energy per unit area, D is the diffusion coefficient of the solute which controls the coarsening process, C_e is the equilibrium concentration of solute in the matrix in the units of mol m⁻³ and V_m is the molar volume of the particles. Another important conclusion is that the asymptotic state of the system is independent of the initial conditions. The particle radius distribution is self-similar under the scaling of the mean particle size. In addition to this prediction, an analytic form for the particle distribution function was obtained. This theory used the following assumptions (Baldan, 2002):

- (1) the shape of coarsening precipitates is spherical.
- (2) the particles are fixed in space.
- (3) the inter-particle distances between the particles are large compared with the particle radius.

Eq. (4.1) shows that the coarsening rate constant K is proportional to the interfacial energy, diffusivity of solutes and equilibrium concentration of solutes in the matrix. Therefore, the addition of molybdenum in alloys may suppress the coarsening process of TiC particle because it reduces

4.1. Lifshitz, Slyozov and Wagner Model

the interfacial energy and equilibrium concentration of titanium in the matrix.

In Eq. (4.1), the calculation of the coarsening rate of the particle demands the values σ , V_m , D and C_e . In this research, it is assumed that the coarsening of TiC is governed only by the diffusion of titanium. Accordingly, the precipitation volume of TiC phase per one mole of Ti, the diffusivity of Ti in the ferrite and equilibrium concentration of Ti in ferrite are obtained from the *TCFE6.2* and *MOBFE1* databases (Andersson *et al.*, 2002; Sundman *et al.*, 1985).

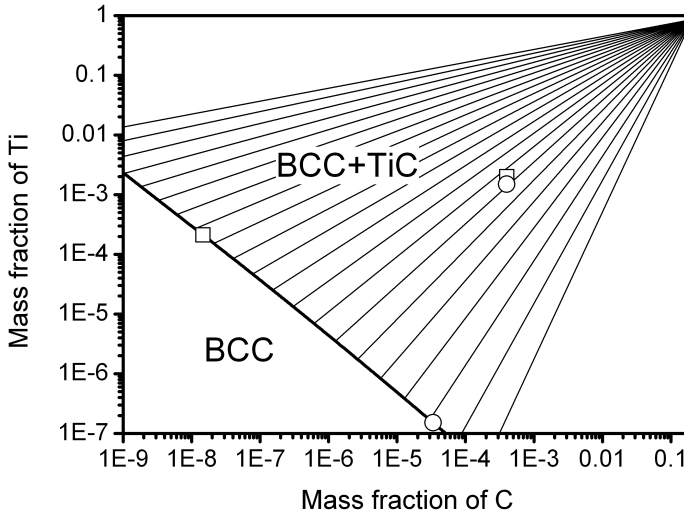


Figure 4.1: Calculated ternary phase diagram of Fe-Ti-C system at 700°C. The concentrations are in mass fractions. The blank rectangle and circle in two phase region correspond to 0.2Ti-0.04C wt% and 0.15Ti-0.04C wt%, respectively. The blank rectangle and circle on the lines between BCC(ferrite) phase region and two phase region indicate equilibrium concentrations in ferrite.

Fig. 4.1 represents the ternary phase diagram of Fe-Ti-C system at

4.1. Lifshitz, Slyozov and Wagner Model

700°C. The equilibrium concentration in the BCC phase follows a straight line with about -1 as the slope. This shows the constant solubility product of Ti and C at a given temperature. The blank circle and rectangle in the two-phase region of BCC and TiC indicate the correspond to 0.2Ti-0.04C and 0.15Ti-0.04C wt%, respectively. The blank circle and rectangle on the line between the BCC single phase region and the two-phase region indicate calculated equilibrium compositions in ferrite for each of the system referred to. In the case of 0.2Ti-0.04C wt%, most of C atoms are consumed to form TiC and certain amount of Ti atoms remained in the ferrite. On the other hand, in the case of 0.15Ti-0.04C wt% alloy, the number of C atoms is enough to consume most Ti, leading little Ti dissolved in the matrix. The equilibrium mass fractions of Ti in ferrite are 2.1×10^{-4} and 1.5×10^{-7} for 0.20Ti-0.04 wt% and 0.15Ti-0.04C wt%, respectively.

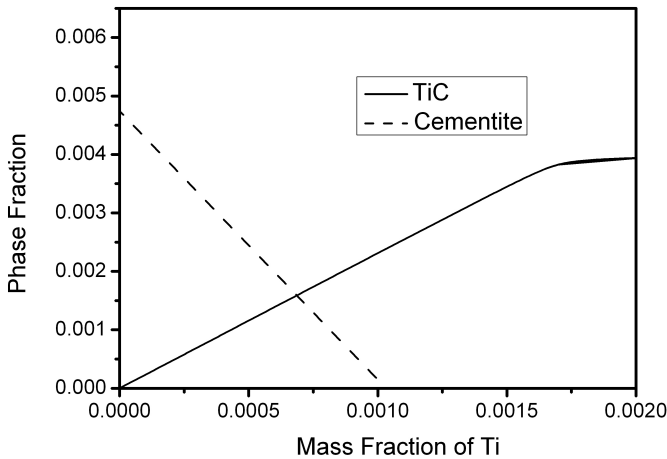


Figure 4.2: Calculated phase fractions at 700°C of TiC and cementite as a function of Ti concentration, using *ThermoCalc* with the *TCFE6.2* database.

4.1. Lifshitz, Slyozov and Wagner Model

Fig. 4.2 includes the calculated equilibrium phase fraction at 700°C of TiC and cementite as a function of Ti concentration based on the 0.04 wt% of carbon. There is no cementite in the region higher Ti concentration than 0.1 wt%. In addition, the amount of TiC phase increases linearly only in the region with less than 0.17 wt% of Ti, but beyond that concentration, the amount of TiC increases slightly with the concentration of Ti. The calculations for the systems with 0.15Ti, 0.18Ti and 0.20Ti wt% are conducted in this chapter.

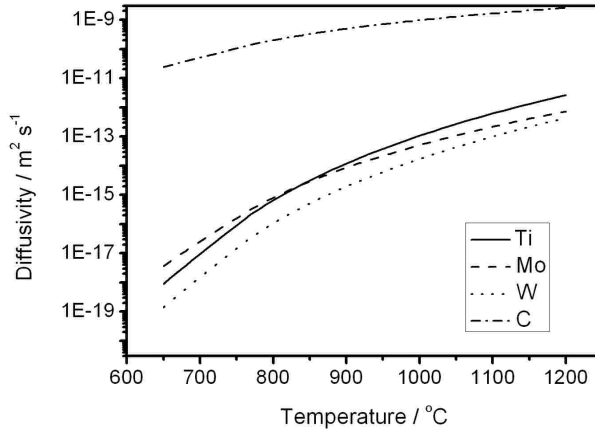


Figure 4.3: Calculated diffusivities in BCC phase of Ti, Mo, W and C in 0.2Ti-0.1Mo-0.1W-0.04C system from the *MOBFE1* database as a function of temperature.

As mentioned previously, the diffusivity of solutes in ferrite, which controls the coarsening process, also affects the coarsening rate in the LSW model. Fig. 4.3 contains the calculated data of some elements, which can affect the formation of carbides, as a function of temperature. The data of Ti, Mo, W and C in BCC phase were achieved from *TCFE6.2* and *MOBFE1* database for 0.2Ti-0.1Mo-0.1W-0.04C wt% system. The diffu-

4.1. Lifshitz, Slyozov and Wagner Model

Table 4.1: Calculated diffusivity, Ti equilibrium concentration in matrix and molar volume of precipitates for one mole of Ti in precipitates at 700°C . The values of C_e are converted to number of moles per volume using mole fraction of Ti in matrix and molar volume of matrix.

wt%	$D / \text{m s}^{-2}$	$C_e / \text{mol m}^{-3}$	$V_m / \text{m}^3 \text{mol}^{-1}$
0.20Ti-0.04C	9.3041×10^{-18}	33.80	1.2452×10^{-5}
0.18Ti-0.04C	9.2739×10^{-18}	7.9383	1.2442×10^{-5}
0.15Ti-0.04C	9.2648×10^{-18}	0.0241	1.2407×10^{-5}

sivity of C at 700°C is $10^6 \sim 10^7$ higher than the substitutional elements. The reported diffusivities of substitutional elements in ferrite shows that Ti has higher impurity diffusivity than Mo or W at 1050 K (Huang *et al.*, 2010; Nitta *et al.*, 2002; Takemoto *et al.*, 2007). The calculated diffusivities of Ti, Mo and W at 700°C are 9.4×10^{-18} , 2.5×10^{-17} and 1.5×10^{-18} $\text{m}^2 \text{s}^{-1}$, respectively. The values of Mo and W are about 2.7 times higher and 0.16 times smaller than that of Ti, respectively. Therefore, the formation of particle with high concentration of Mo at the initial stage of precipitation cannot be explained on the basis of either thermodynamics or diffusion of Mo.

The calculated parameters of the precipitates for 700°C are listed in Table 4.1. The values of Ti equilibrium concentration are converted to number of moles per volume using the molar volume of the matrix. The diffusivity of Ti, the equilibrium concentration of Ti and molar volume of TiC phase increased as the average concentration of Ti increases. Even though the differences of D and V_m between each system are relatively small, there is a significant difference in C_e more than an order of magnitude. As a result, the difference of C_e changes the coarsening rate dramatically.

Fig.4.4 shows the variation in precipitate mean radius calculated using the LSW model to exhibit time dependent coarsening of the TiC phase at

4.1. Lifshitz, Slyozov and Wagner Model

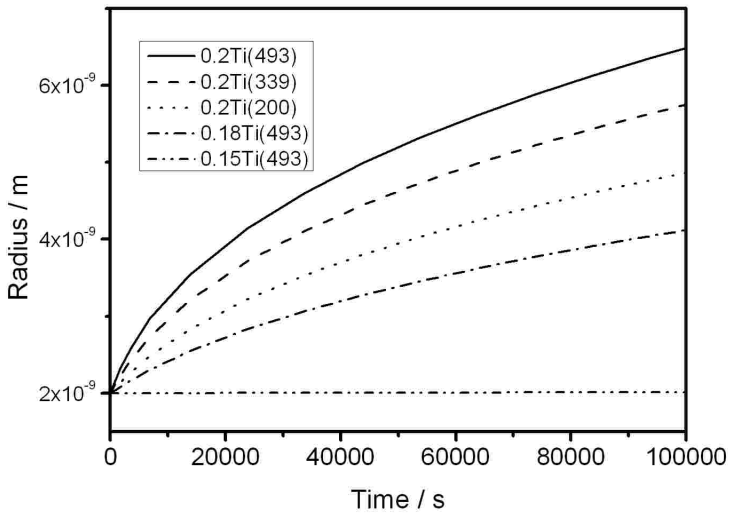


Figure 4.4: Variation of precipitate mean radius calculated using LSW model to exhibit time dependent coarsening of the TiC phase in 0.2Ti-0.04C, 0.18Ti-0.04C and 0.15Ti-0.04C wt% system at 700°C. Three different interfacial energy of 493, 339 and 200 mJ m^{-2} are applied for 0.2Ti-0.04C wt%.

700°C. To reveal the effect of interfacial energy, three values of 493, 339 and 200 mJ m⁻² are applied to 0.2Ti-0.04C wt%. Three different systems with 0.2Ti-0.04C, 0.18Ti-0.04C and 0.15Ti-0.04C wt% are also considered to compare the effect of Ti concentration in a matrix. The particle radii at 10⁵ s of 0.2Ti-0.04C wt% with $\sigma = 493, 339$ and 200 mJ m⁻² are 6.49, 5.75 and 4.87 nm, respectively. The calculated results for 0.2Ti-0.04C, 0.18Ti-0.04C and 0.15Ti-0.04C wt% with same $\sigma = 493$ mJ m⁻² are 6.49, 4.12 and 2.016 nm, respectively. The coarsening rate for 0.15Ti-0.04C wt% is extremely small, because the equilibrium Ti concentration in ferrite is 1/100 times smaller than others. The average concentration of Ti induces significant differences in C_e . Therefore, reducing Ti concentration suppresses effectively the coarsening rate.

4.2 DICTRA Model

The analysis using Eq. (4.1) is simplified since it considers only Ti diffusion. Considering a ternary system of Fe-Ti-C, it would be necessary for the diffusion of two solutes to keep pace in order to maintain local equilibrium at the interface. Because diffusivity of carbon is much faster than titanium, so this cannot in general be satisfied for the tie-line passing through the alloy composition. The local equilibrium compositions are determined by choosing other tie-lines. It is difficult to simulate the determination of local equilibrium condition exactly in LSW theory. In addition, the effects of molybdenum and tungsten cannot be implemented in LSW theory. In this section, the coarsening model has been simulated using *DICTRA* software, which can solve multi-component diffusion problems (Andersson & Agren, 1992).

A schematic representation of the DICTRA model for coarsening is shown in Fig. 4.5. The coarsening of a system can be described by performing calculations on a single particle of maximum size at the center of a spherical cell. It is assumed that the particle size distribution follows

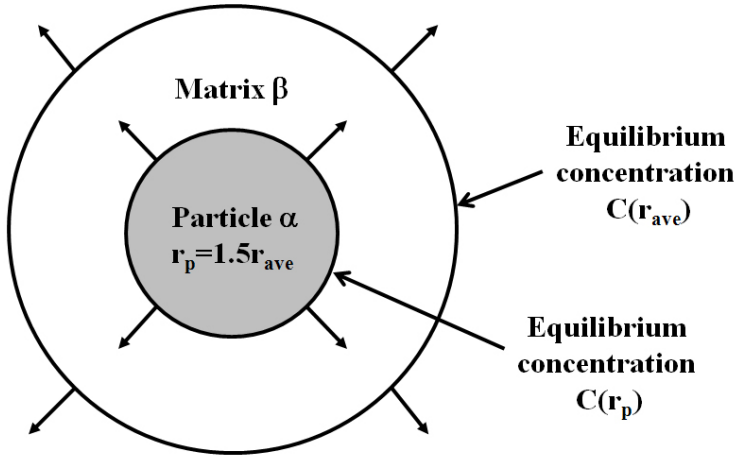


Figure 4.5: A closed system with spherical cell with TiC phase particle at the center of the cell in a ferrite matrix.

the LSW distribution that the maximum particle size is 1.5 times bigger than the average size. A contribution ΔG_m from the interfacial energy is added to Gibbs energy function for the particle due to the capillarity effect.

$$\Delta G_m = \frac{2\sigma V_m}{r} \quad (4.2)$$

where σ is the interfacial energy per unit area, r is the particle radius and V_m is the molar volume. It is assumed that equilibrium between average sized particles, and the matrix holds locally at the cell boundary, taking into account a larger Gibbs energy addition than that of the maximum size particle. Therefore, there is a discrepancy in composition from the cell boundary to the interface between the maximum particle α and matrix β . This difference will make the particle grow and the size of the cell increase in order to maintain the total composition in the cell.

The TiC region is divided with 50 geometrical grid points, with a

4.2.DICTRA Model

Table 4.2: Calculated equilibrium compositions in mass fraction at 700°C. $c_{\text{Ti}}^{\alpha\rho}$ and $c_{\text{C}}^{\alpha\rho}$ are the matrix compositions of Ti and C, which are equilibrium with precipitate phase. $c_{\text{Ti}}^{\rho\alpha}$ and $c_{\text{C}}^{\rho\alpha}$ are the precipitate compositions of Ti and C, which are equilibrium with ferrite.

wt%	$c_{\text{Ti}}^{\alpha\rho}$	$c_{\text{C}}^{\alpha\rho}$	$c_{\text{Ti}}^{\rho\alpha}$	$c_{\text{C}}^{\rho\alpha}$
0.20Ti-0.04C	2.117×10^{-4}	1.464×10^{-8}	0.8173	0.1827
0.18Ti-0.04C	4.971×10^{-5}	7.272×10^{-8}	0.8140	0.1860
0.15Ti-0.04C	1.515×10^{-7}	3.375×10^{-5}	0.8037	0.1963

higher number of grid points at the interface of the region. The ferrite region is divided with 100 equally spaced linear grid points. According to the DICTRA model, a particle size may change, but the spherical shape is maintained throughout the coarsening period. The initial conditions include the chemical compositions and size of the cell. The original chemical compositions in particle and a matrix are obtained from the equilibrium calculation using *ThermoCalc* in combination with the *TCFE6.2* database.

The initial particle radius of r_p is determined to be 3 nm, which is 1.5 times average particle size, assuming that the maximum particle are 1.5 times bigger than average size in LSW theory. The cell size r_v is determined to hold following equation to maintain the phase fractions in the cell.

$$\frac{3/4\pi r_p^3}{3/4\pi r_v^3} = \text{volume fraction of precipitate.} \quad (4.3)$$

Table 4.2 contains the calculated equilibrium compositions at 700°C for three systems. $c_{\text{Ti}}^{\alpha\rho}$ and $c_{\text{C}}^{\alpha\rho}$ are the matrix compositions of Ti and C, which are equilibrium with precipitate phase. $c_{\text{Ti}}^{\rho\alpha}$ and $c_{\text{C}}^{\rho\alpha}$ are the precipitate compositions of Ti and C, which are equilibrium with ferrite, respectively. $c_{\text{Ti}}^{\alpha\rho}$ and $c_{\text{Ti}}^{\rho\alpha}$ increased as the total amount of Ti in system increases. $c_{\text{Ti}}^{\alpha\rho}$ for 0.20Ti-0.04C wt% is about 1000 times higher than that of 0.15Ti-0.04C wt%. The calculated phase fractions of ferrite and precip-

Table 4.3: Calculated equilibrium phase quantities for ferrite and precipitate phase in volume fraction at 700°C. r_v are the radius of total system which matches the volume fraction of precipitate with 3 nm radius.

wt%	ferrite	precipitate	r_v
0.20Ti-0.04C	0.99645	3.552×10^{-3}	19.66
0.18Ti-0.04C	0.99653	3.473×10^{-3}	19.81
0.15Ti-0.04C	0.99703	2.968×10^{-3}	20.87

itate, and its corresponding initial cell size calculated from Eq. (4.3) are listed in Table 4.3. The phase fraction of precipitates in 0.20Ti-0.04C wt% is bigger than those of 0.18Ti-0.04C and 0.15Ti-0.04C wt%. As a result, the cell size r_v of 0.20Ti-0.04C wt% should be smaller than those of others to maintain the equilibrium phase volume fraction.

Fig. 4.6 shows variations of precipitate radius calculated using DICTRA model to exhibit time dependent coarsening rate of the TiC phase at 700°C. The particle radii at 10^5 s of 0.20Ti-0.04C wt% with $\sigma = 493, 339$ and 200 mJ m^{-2} are 6.33, 5.47 and 4.52 nm, respectively. Those values correspond to 7%, 15% and 21% smaller coarsening rate constant K than those from LSW theory. The calculated results for 0.18Ti-0.04C and 0.15Ti-0.04C wt% with fixed $\sigma = 493 \text{ mJ m}^{-2}$ are 4.21 and 2.019 nm, respectively. The coarsening rate constant K of 0.18Ti-0.04C and 0.15Ti-0.04C wt% are about 8% and 19% larger than those from LSW prediction.

Fig. 4.7 demonstrate variation of titanium and carbon concentration across the interface between TiC and ferrite for 0.2Ti-0.04C wt% with $\sigma = 493 \text{ mJ m}^{-2}$, respectively. They contain the profiles at different intervals starting from 0 s to 10^5 s with 10^4 s and 3×10^4 s. The lines at 0 s indicate the profiles with equilibrium compositions. At the introductory stage of the process, both local equilibrium compositions of Ti and C at the interface are determined higher than original compositions. The equi-

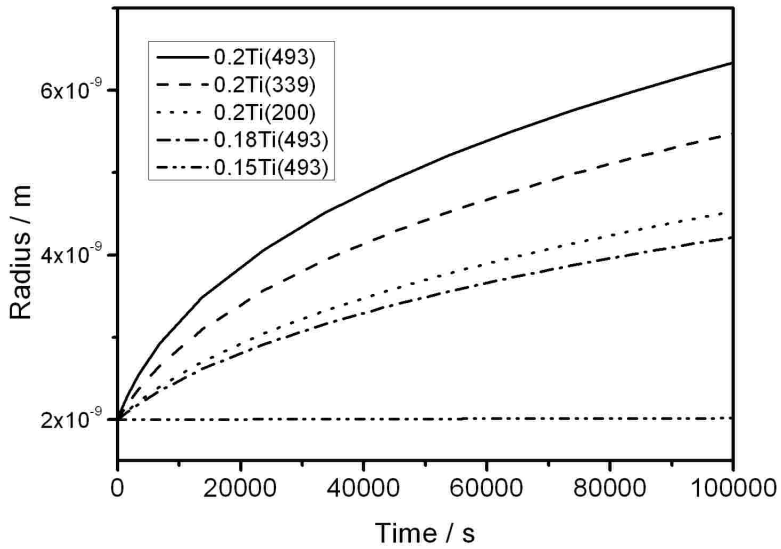


Figure 4.6: Variation of precipitate mean radius calculated using DICTRA model to exhibit time dependent coarsening of the TiC phase in 0.20Ti-0.04C, 0.18Ti-0.04C and 0.15Ti-0.04C wt% system at 700°C. Three different interfacial energy of 493, 339 and 200 mJ m^{-2} are applied for 0.2Ti-0.04C wt%.

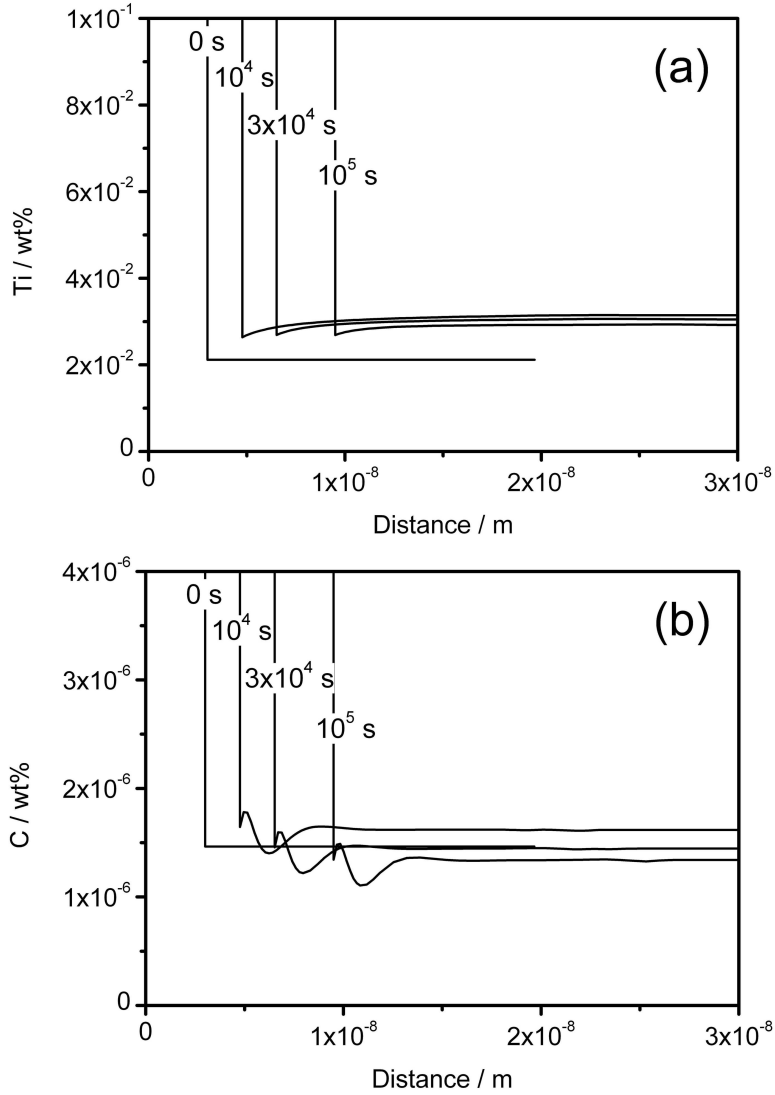


Figure 4.7: Concentration-distance profile for 0.20Ti-0.04C wt% with $\sigma = 0.493 \text{ J m}^{-2}$, showing distribution of (a) Ti and (b) C across the interface between precipitate and ferrite matrix at different time intervals.

librium composition of Ti at the interface increases as interface moves. However, the equilibrium composition of C at the interface decreases to smaller values than original composition as interface moves.

Fig. 4.8 demonstrate variation of Ti and C concentration across the interface between TiC and ferrite for 0.15Ti-0.04C wt% with $\sigma = 493 \text{ mJ m}^{-2}$, respectively. At the initial stage of process, both of the local equilibrium compositions of Ti and C at interface are determined higher than initial compositions like 0.20Ti-0.04C wt%. The equilibrium composition of Ti at the interface decreases slightly as the interface moves, while the equilibrium composition of C at the interface increases.

Fig. 4.9 shows a calculated ternary phase diagram of Fe-Ti-C system at 700°C . The blank rectangle and circle on the lines between BCC phase region and two-phase region indicate equilibrium concentrations in BCC for 0.20Ti-0.04C and 0.15Ti-0.04C wt%, respectively. The solid rectangle and circle indicate the corresponding equilibrium concentration at the interface at 10^2 s and 10^5 s of interface movement. The arrows show the concentration change from 10^2 s to 10^5 s .

During coarsening process, the concentration is not on the phase boundary since the unstable TiC phase widens the BCC phase region due to the capillarity effect. The local equilibrium concentrations are determined based on the combination of the capillarity effect and the difference of diffusivities of Ti and C. In the 0.2Ti-0.04C wt%, Ti concentration is close to the equilibrium, while C concentration is much higher than the equilibrium. The effect of capillarity decreases as interface moves. Thus, the composition moves to the BCC phase boundary as Ti composition increases and C composition decreases. It can be noted that the C composition moves to less than the equilibrium value. However, 0.15Ti-0.04C wt% shows different results. At the initial stage, C concentration is close to the equilibrium, and Ti is larger than equilibrium concentration. During the coarsening process, Ti decreases and C increases.

Based on those results, further calculations about the Mo effect were

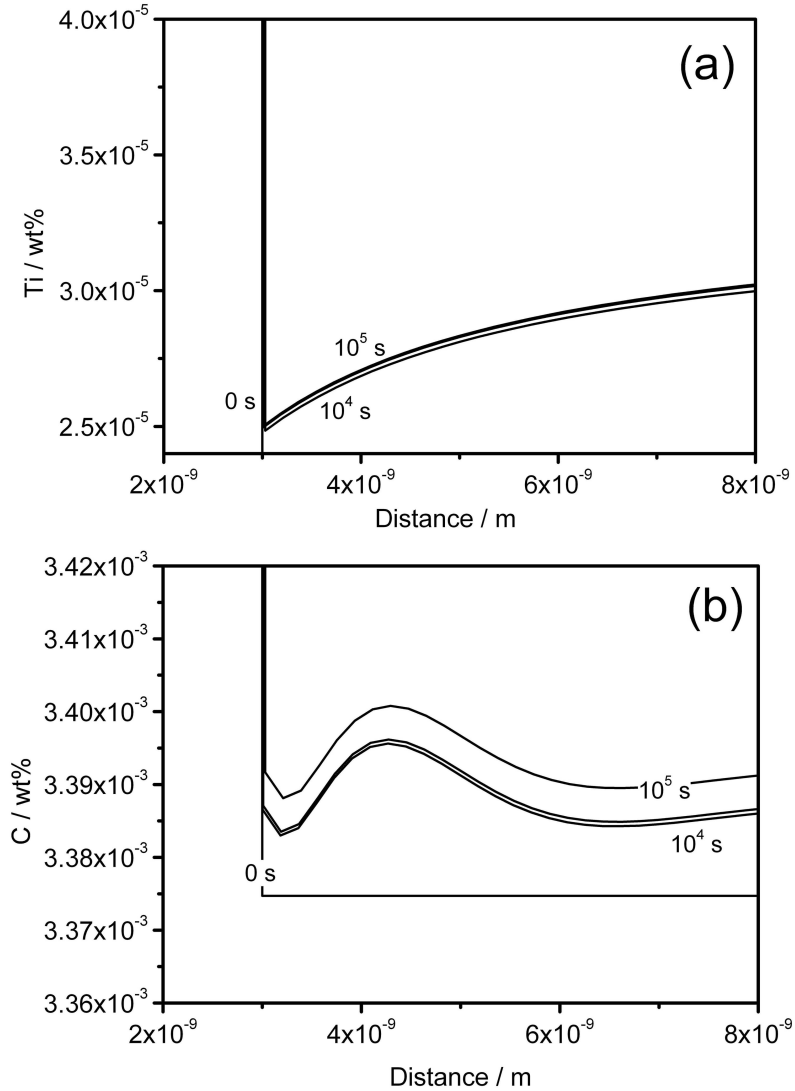


Figure 4.8: Concentration-distance profile for 0.15Ti-0.04C wt% with $\sigma = 0.493 \text{ J m}^{-2}$, showing distribution of (a) Ti and (b) C across the interface between precipitate and ferrite matrix at different time intervals.

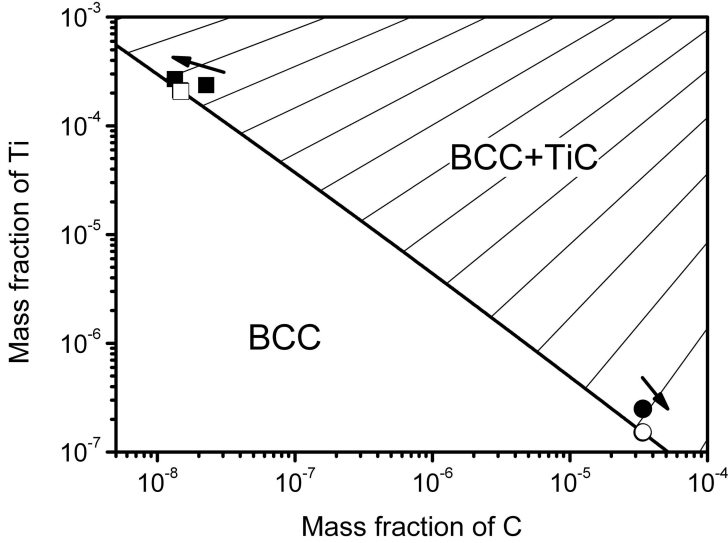


Figure 4.9: Calculated ternary phase diagram of Fe-Ti-C system at 700°C. The concentrations are in mass fractions. The blank rectangle and circle on the lines between BCC phase region and two phase region indicate equilibrium concentrations in BCC. The solid rectangle and circle indicate corresponding equilibrium concentration at the interface at 10^2 s and 10^5 s of interface movement.

Table 4.4: Calculated equilibrium phase quantities for ferrite and precipitate phase in volume fraction at 700°C. r_v are the radius of total system which corresponds to the volume fraction of precipitate with 3 nm radius.

wt%	ferrite	precipitate	r_v
0.20Ti-0.05Mo-0.04C	0.99645	3.552×10^{-3}	19.66
0.15Ti-0.05Mo-0.04C	0.99701	2.993×10^{-3}	20.82

Table 4.5: Calculated equilibrium compositions in mass fraction at 700°C for 0.20Ti-0.05Mo-0.04C wt%.

	Ti	Mo	C
ferrite	2.1169×10^{-4}	5.0104×10^{-4}	1.4745×10^{-8}
precipitate	8.1723×10^{-1}	2.7519×10^{-5}	1.8274×10^{-1}

Table 4.6: Calculated equilibrium compositions in mass fraction at 700°C for 0.15Ti-0.05Mo-0.04C wt%.

	Ti	Mo	C
ferrite	1.6274×10^{-7}	4.7674×10^{-4}	3.1292×10^{-5}
precipitate	7.9239×10^{-1}	1.2767×10^{-2}	1.9483×10^{-1}

performed. Table 4.4 shows the calculated equilibrium phase quantities for ferrite and precipitate phase in a volume fraction at 700°C. r_v is the radius of the total system which corresponds to the volume fraction of a precipitate with 3 nm radius. Tables 4.5 and 4.6 list the calculated equilibrium compositions in mass fraction at 700°C for 0.20Ti-0.05Mo-0.04C and 0.15Ti-0.05Mo-0.04C wt%, respectively.

Fig. 4.10 presents the variation of precipitate radius calculated using DICTRA model. It contains the time-dependent coarsening of the precipitates in 0.15Ti-0.04C and 0.15Ti-0.05Mo-0.04C wt% at 700°C with $\sigma = 0.339 \text{ J m}^{-2}$. The particle sizes of 0.20Ti-0.04C and 0.20Ti-0.05Mo-0.04C wt% are 5.476 and 5.477 nm, respectively, which are almost same. 0.15Ti-0.04C and 0.15Ti-0.05Mo-0.04C wt% show 2.02 and 2.01 nm, respectively, which indicate that the coarsening rates decrease a little due to the Mo addition. It can be caused from that the local equilibrium should be achieved so that interface can move since Mo concentration is relatively higher in the precipitate in the 0.15Ti-0.05Mo-0.04C wt%.

Fig. 4.11 shows variation of Mo concentration in the precipitate close to the interface between (Ti,Mo)C and ferrite for 0.2Ti-0.05Mo-0.04C

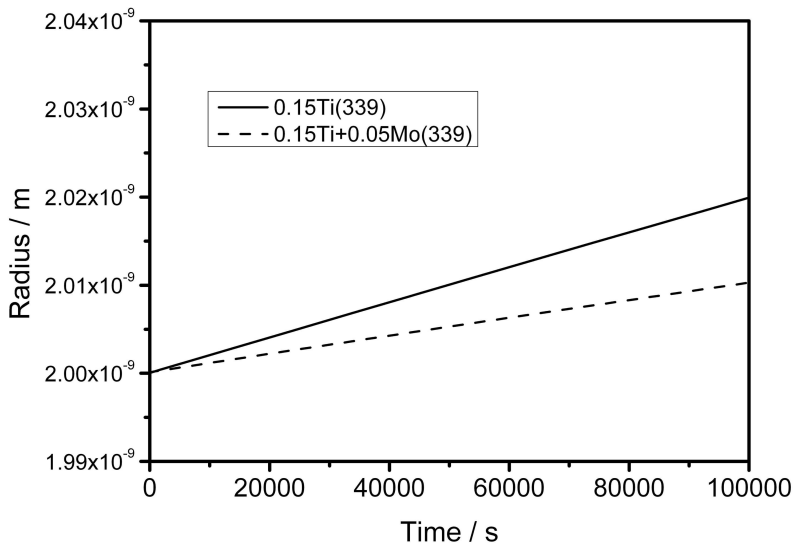


Figure 4.10: Variation of precipitate mean radius calculated using DICTRA model to exhibit time dependent coarsening of the precipitates in 0.15Ti-0.04C and 0.15Ti-0.05Mo-0.04C wt% system at 700°C with 0.339 J m^{-2} as interfacial energy.

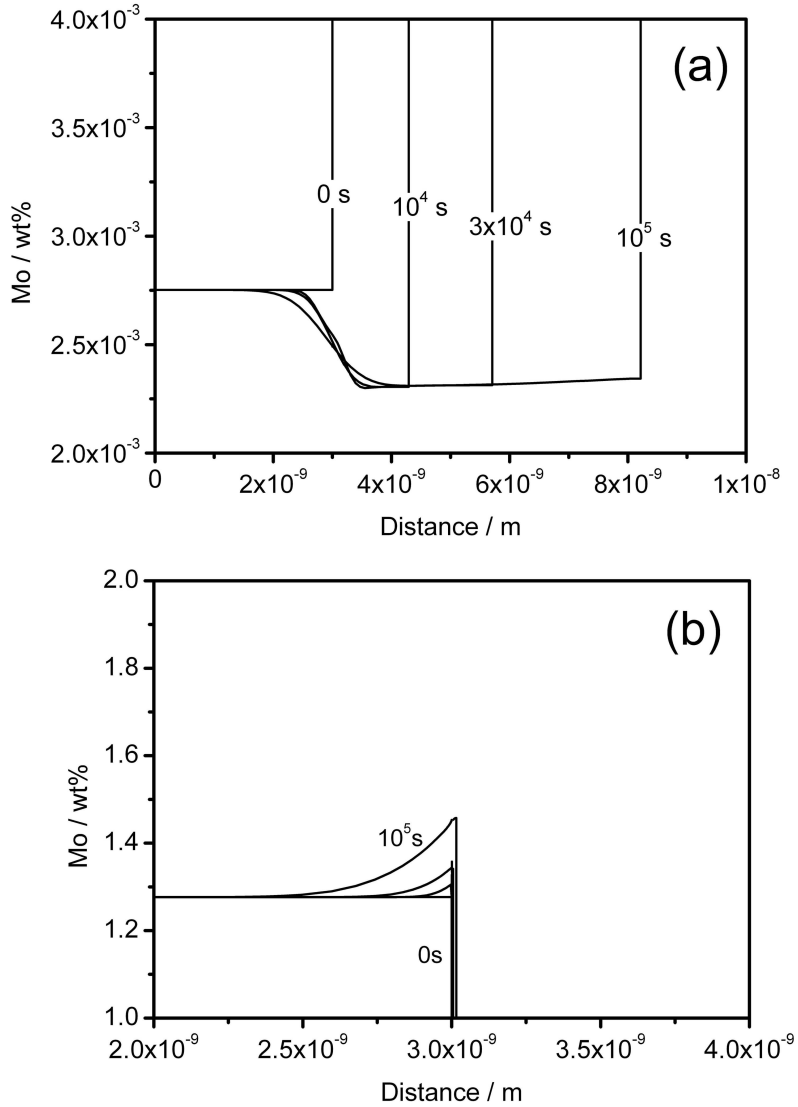


Figure 4.11: Concentration-distance profile for (a)0.20Ti-0.05Mo-0.04C wt% (b)0.15Ti-0.05Mo-0.04C wt% with $\sigma = 0.339 \text{ J m}^{-2}$, showing distribution of Mo across the interface between precipitate and ferrite matrix at different time intervals.

4.3.Kampmann and Wagner’s Numerical Model

and 0.15Ti-0.05Mo-0.04C wt% with $\sigma = 0.339 \text{ J m}^{-2}$. They contain the profiles at different intervals starting from 0 s to 10^5 s with 10^4 s and 3×10^4 s. The lines at 0 s indicate the profiles with equilibrium compositions. The equilibrium Mo concentration of 0.20Ti-0.05Mo-0.04C wt% at the interface in the precipitate is lower than a matrix. It rarely changes during coarsening. In contrast, the amount of Mo of 0.15Ti-0.05Mo-0.04C wt% at the interface in the precipitate is more than a matrix. It is noted that Mo is saturated at the interface in precipitate as interface moves. The interface moves slower than 0.15Ti-0.04C wt%, since the balance between the flux of Mo and the interface velocity has to be achieved.

The coarsening processes for each system have been simulated using DICTRA model. Moreover, the effect of molybdenum on the concentration profile has been studied from the addition of 0.05 wt% Mo. Mo concentrations in the precipitate are 0.0025 wt% and 1.3 wt% for 0.2Ti-0.05Mo-0.04C and 0.15Ti-0.05Mo-0.04C wt%, respectively. However, the amounts of Mo in precipitate are too small to explain the existence of the precipitate with high Mo concentration. The introduction of Mo in TiC cannot be explained from thermodynamics only. Furthermore, the present calculations with the DICTRA model show that Mo in a matrix hardly affects on the multi-component diffusion process.

4.3 Kampmann and Wagner’s Numerical Model

It is possible to predict the effect of interfacial energy and solute concentration on matrix by using LSW and DICTRA models. Modifications of the LSW theory are necessary since the time-independent radius distribution predicted by LSW is usually not observed experimentally (Baldan, 2002). It is common to deal with precipitation from a super-saturated solution as the sequence of nucleation, growth and coarsening processes. Kampmann and Wagner produced a numerical approach (KWN model) capable to describe the particle size distribution in the

4.3.Kampmann and Wagner’s Numerical Model

time domain (Samaras, 2006). This model deals with nucleation-growth-coarsening phenomena within the same formulation. In this research, the coarsening rates of several systems are simulated applying a modification of the KWN framework without nucleation.

The kinetic computations were coupled to *ThermoCalc* software employing the *TCFE6.2* thermodynamic database and the *MOBFE1* mobility database. The thermodynamic calculations are included in the whole program by migration from Fortran subroutines in TQ interface to C language. The time evolution of the precipitates was computed in discrete time steps as 0.01 s from 0 s to 10^5 s. The thermodynamic equilibrium and kinetic data are achieved every 1000 steps. The particle size distribution is divided into a series of 5000 discrete classes. The initial state of particle size distribution is scaled to reach the equilibrium phase fraction of a precipitate. It is assumed that there is no nucleation in the coarsening process. The particles smaller than 0.1 nm radius are deleted in the particle list.

In every time step, the following computations are conducted: (1) an instantaneous phase equilibrium is obtained from *ThermoCalc*, (2) the growth or dissolution rate of the existing particles is obtained accounting for capillarity effects, (3) the particle size in the list and particle list itself is updated (4) mass balance is imposed assuming the matrix composition to be homogeneous using following equation.

$$\bar{c}_{\text{Ti}} = c_{\text{Ti}} - c_{\text{Ti}}^{\rho\alpha} \int_0^{\infty} \frac{4}{3} \pi r^3 \varphi(r) dr \quad (4.4)$$

where $\varphi(r)$ is the size distribution function, c_{Ti} is the mass fraction of Ti in the whole system, $c_{\text{Ti}}^{\rho\alpha}$ is the calculated mass fraction of Ti in precipitate which is equilibrium with ferrite and \bar{c}_{Ti} is the mass fraction remained in the matrix. \bar{c}_{Ti} is used for the thermodynamic calculations in the next step.

Fig. 4.12 shows the variations of precipitate radius calculated using

4.3.Kampmann and Wagner's Numerical Model

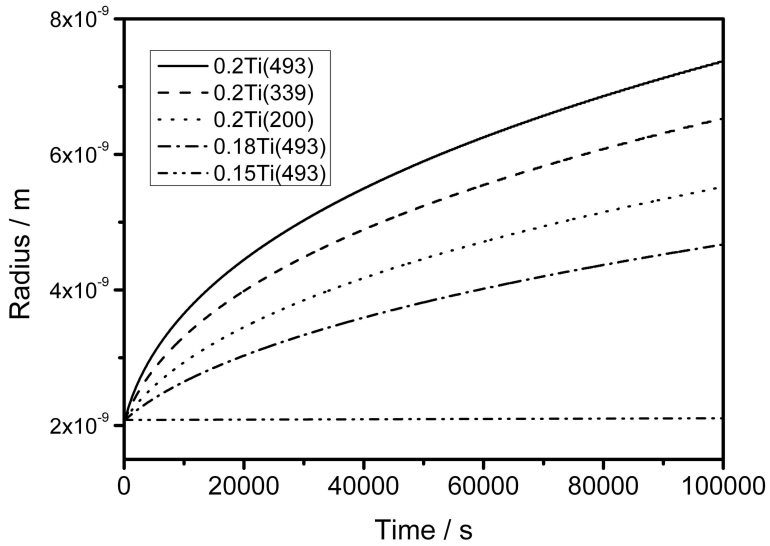


Figure 4.12: Variation of precipitate mean radius calculated using KWN model to exhibit time dependent coarsening of the TiC phase in 0.20Ti-0.04C, 0.18Ti-0.04C and 0.15Ti-0.04C wt% system at 700°C. Three different interfacial energy of 493, 339 and 200 mJ m^{-2} are applied for 0.2Ti-0.04C wt%.

4.3.Kampmann and Wagner’s Numerical Model

KWN model at 700°C. The particle radii at 10⁵ s of 0.2Ti-0.04C wt% with $\sigma = 493, 339$ and 200 mJ m^{-2} are 7.37, 6.53 and 5.52 nm, respectively. The calculated results for 0.20Ti-0.04C, 0.18Ti-0.04C and 0.15Ti-0.04C wt% with same $\sigma = 493 \text{ mJ m}^{-2}$ are 7.37, 4.67 and 2.024 nm, respectively. The comparison of precipitate radius predicted from LSW, DICTRA and KWN model are included in Fig 4.13. They exhibit time dependent coarsening of the TiC phase in 0.2Ti-0.04C and 0.15Ti-0.04C wt% at 700°C with 493 mJ m^{-2} as interfacial energy, respectively. Those values correspond to 48%~52% larger coarsening rate constant K than those from LSW theory. The radii from LSW are underestimated because it is assumed that the normalized particle distribution is independent of time.

Fig. 4.14(a) includes the calculated particle size distribution of 0.20Ti-0.04C wt% with $\sigma = 0.493 \text{ J m}^{-2}$. It contains the distributions at different times starting from 0 s to 10⁵ s with 10⁴ s and 3×10^4 s. The lines at 0 s indicate the LSW distribution. The distributions are achieved from the particle lists by dividing 50 grids from 0 to 15 nm. The particle distribution moves to larger size, and the number of particles decreases dramatically.

Fig. 4.14(a) is redrawn using normalized frequency as a function of normalized radius ($= r/\bar{r}$) in Fig. 4.14(b). The particle lists were normalized by using the average radius at a given time, and particle radii are recounted in the 50 grids from 0 to 1.5. The average radius locates at 1.0. The shape of normalized distribution becomes more symmetric, with the average located at the center. In addition, the distributions are converged to a certain function after critical time. The calculated radii in this model are much bigger than those from predicted in LSW theory since the numbers of small particles are overestimated in LSW theory.

The LSW predicts that after long times the distribution of scaled particle sizes should reach a universal form that is independent of all material’s parameters. However, the measured particle size distributions are different from the LSW theory. The reported distributions are generally

4.3. Kampmann and Wagner's Numerical Model

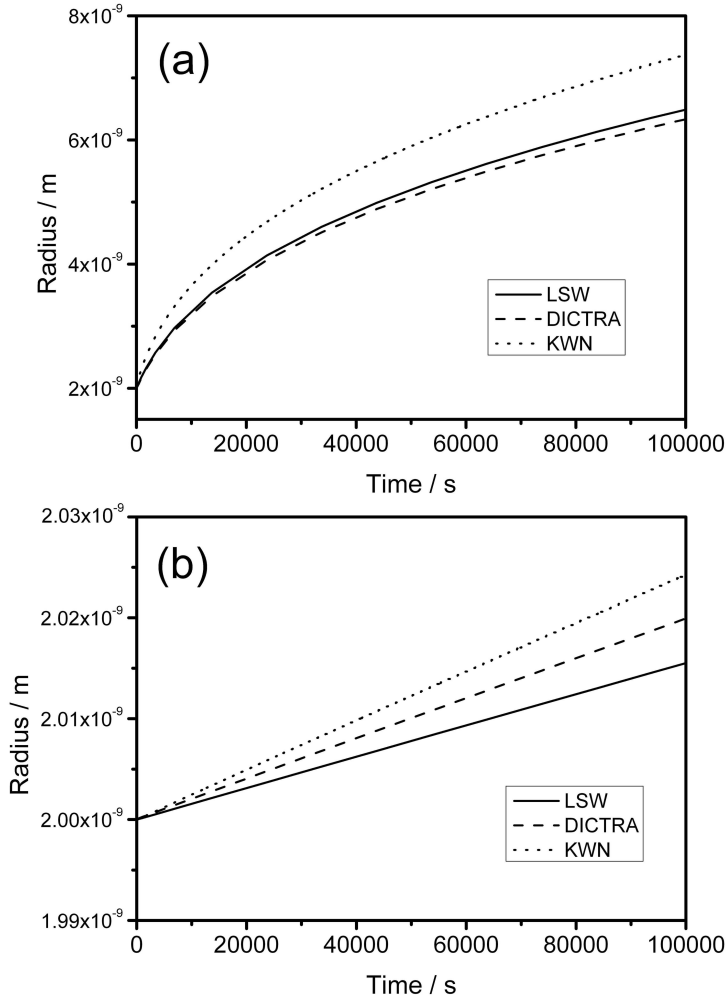


Figure 4.13: Variation of precipitate radius calculated using LSW, DICTRA and KWN model exhibit time dependent coarsening of the TiC phase in (a) 0.20Ti-0.04C (b) 0.15Ti-0.04C wt% at 700°C with 493 mJ m^{-2} as interfacial energy.

4.3.Kampmann and Wagner's Numerical Model

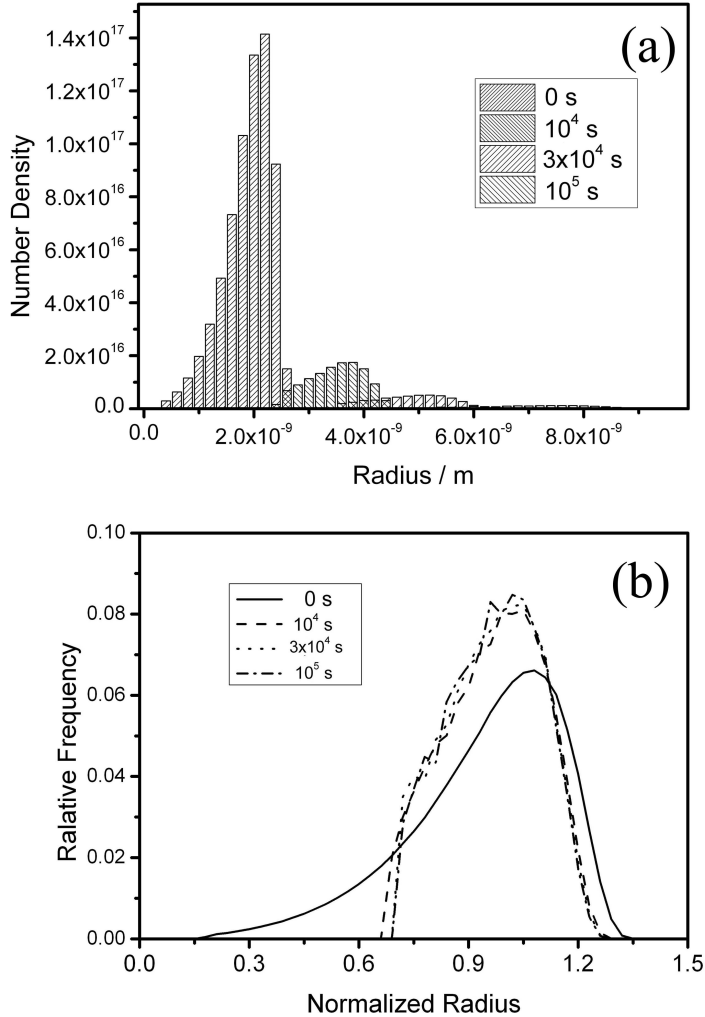


Figure 4.14: Calculated (a) number density of precipitate as a function of particle radius (b) relative frequency of precipitate as a function of normalized particle radius, which are obtained from from the KWN model, in 0.20Ti-0.04C wt% at 700°C with different ageing time.

4.3.Kampmann and Wagner’s Numerical Model

more symmetric than the LSW predictions (Baldan, 2002; Kang & Yoon, 1982). A problem with the LSW approach was the assumption that a coarsening rate is independent of its surrounding. A particle with nearest neighbors which are larger than itself will coarsen at exactly the same rate as if it were surrounded by particles that were of a smaller radius. It causes the apparent disagreement between the theoretically predicted and experimentally measured particle size distribution.

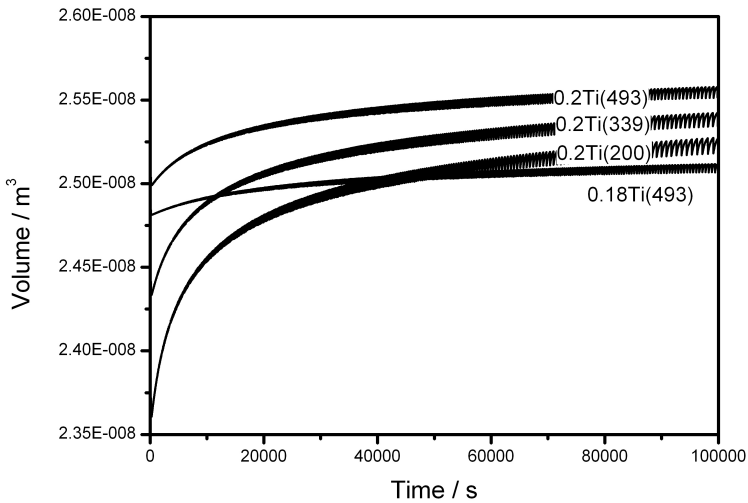


Figure 4.15: Variation of precipitate volume calculated using KWN model to exhibit time dependent coarsening of the TiC phase in 0.20Ti-0.04C and 0.18Ti-0.04C wt% at 700°C with different interfacial energy. The interfacial energies are included in parenthesis in J m^{-2} units.

Figs 4.15, 4.16 and 4.17 show the calculated evolution of precipitate volume, Ti concentration in a matrix and number of precipitates for each system. There are fluctuations in the curves in Figs 4.15 and 4.16, because the precipitate volume and Ti concentration can change abruptly when a large number of particles with same radius are deleted in the

4.3.Kampmann and Wagner’s Numerical Model

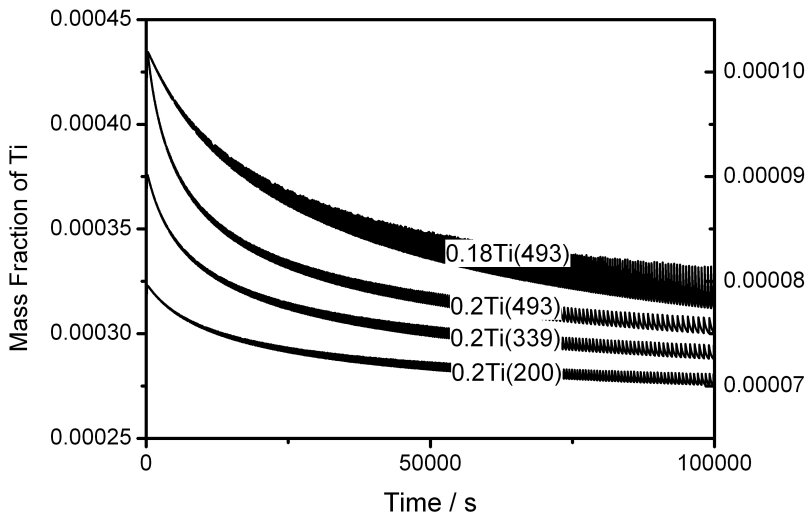


Figure 4.16: Variation of Ti fraction in ferrite matrix calculated using KWN model to exhibit time dependent coarsening of the TiC phase in 0.20Ti-0.04C and 0.18Ti-0.04C wt% at 700°C with different interfacial energy. Units of left and right axis correspond to the values of 0.20Ti-0.04C and 0.15Ti-0.04C wt%, respectively. The interfacial energies are included in parenthesis in J m^{-2} units.

4.3.Kampmann and Wagner’s Numerical Model

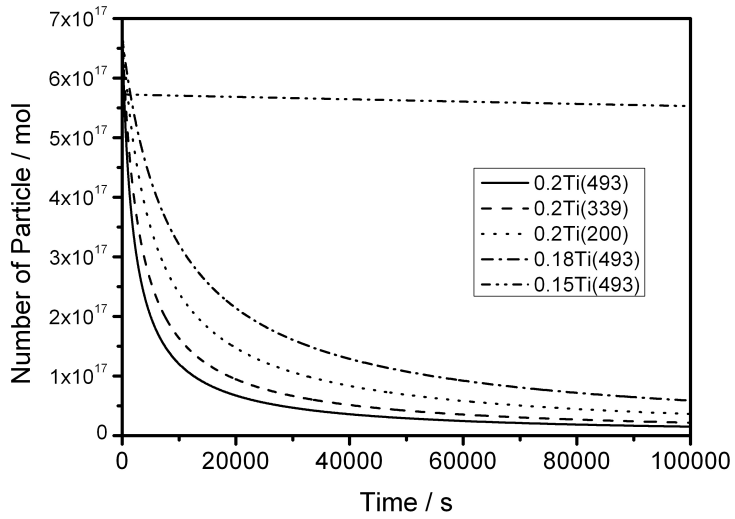


Figure 4.17: Variation of number of precipitates calculated using KWN model to exhibit time dependent coarsening of the TiC phase in 0.20Ti-0.04C and 0.18Ti-0.04C wt% at 700°C with different interfacial energy. The interfacial energies are included in parenthesis in J m^{-2} units.

4.3. Kampmann and Wagner's Numerical Model

list. The radius of the particles decreases at the early stages until the Ti concentration in the matrix reaches critical conditions for coarsening.

In the 0.20Ti-0.04C wt% with $\sigma = 493 \text{ mJ m}^{-2}$, Ti mass fraction in the matrix reaches up to 4.3×10^{-4} , which are much higher than the calculated equilibrium value 2.1×10^{-4} . The simulation results show that the volume fraction decreases more with higher interfacial energy. The volume fraction and Ti concentration approaches to the equilibrium during coarsening process as particle radius increases.

The curvature-dependence of the interface concentration is given by the well-known Gibbs-Thomson equation. For an infinite radius of curvature, the original composition of the matrix α equilibrium with precipitate would be $c^{\alpha\rho}$, but the composition will be increased to $c_r^{\alpha\rho}$ with interface curvature r . Thus, the change in composition becomes

$$c_r^{\alpha\rho} = \left(1 + \frac{2\Gamma}{r}\right)c^{\alpha\rho} \quad (4.5)$$

where Γ is the capillarity constant given by the regular solution approximation ([Christian, 2002](#))

$$\Gamma = \frac{\sigma V_m}{RT(c^{\rho\alpha} - c^{\alpha\rho})}. \quad (4.6)$$

For the 0.20Ti-0.04C wt%, the Ti mass fraction in matrix equilibrium with 3 nm radius precipitate is evaluated to 3.7×10^{-4} . It is larger than the mass fraction of 2.7×10^{-4} from DICTRA model. Therefore, this also contributes to the higher coarsening rate in this model.

It is noted in [Fig. 4.17](#) that the number density of particles decreases monotonically, because the processes are simulated without nucleation. Comparing with different interfacial energy for the 0.20Ti-0.04C wt%, more particles disappeared with higher one.

In this chapter, the effects of interfacial energy and Ti concentration in a matrix on coarsening rate had been investigated applying LSW,

DICTRA and KWN models. The LSW theory derives two well-known results. The first is that the cube of the mean particle radius should change linearly with time. The second result is that an arbitrary distribution of particle radii when scaled by the mean radius should be a specific time-independent form. However, this theory contains restrictions that the distribution is usually not matched with experiments, and it cannot illustrate multi-component diffusion controlled coarsening.

The DICTRA model can simulate the multi-component diffusion controlled coarsening process for the Fe-Ti-C ternary system. The interface composition of Ti and C, which satisfies the equations for the solute flux and interface velocity, has been explored. In addition, the effect of Mo in a matrix on coarsening rate has been studied. However, this model also based on the assumption that the normalized particle distribution function follows time independent universal function. Not only, the particle distribution, but also the local equilibrium concentrations of Mo in the precipitate restrict to simulate the coarsening process with high Mo concentration precipitates.

In the last, the coarsening processes with various radii of the particles are simulated using the interface velocity equation from KWN model without nucleation. The results from this model indicate much faster coarsening rate than those from LSW and DICTRA models. The higher coarsening rate in this model comes from a change of normalized particle distribution and higher Ti concentration in a matrix than that in DICTRA model. It is also noted that normalized particle distribution functions converge to a different function, which is more symmetric and narrower.

References

ANDERSSON, J. & AGREN, J. (1992). Models for numerical treatment of multicomponent diffusion in simple phases. *Journal of Applied Physics*,

- 72**, 1350–1355. [127](#), [134](#)
- ANDERSSON, J., HELANDER, T., HÖGLUND, L., SHI, P. & SUNDMAN, B. (2002). Thermo-calc & dictra, computational tools for materials science. *Calphad*, **26**, 273–312. [129](#)
- BALDAN, A. (2002). Review progress in ostwald ripening theories and their applications to nickel-base superalloys part i: Ostwald ripening theories. *Journal of Materials Science*, **37**, 2171–2202. [128](#), [146](#), [152](#)
- CHRISTIAN, J. (2002). *The Theory of Transformations in Metals and Alloys: Part I+ II.* Elsevier. [155](#)
- HUANG, S., WORTHINGTON, D., ASTA, M., OZOLINS, V., GHOSH, G. & LIAW, P. (2010). Calculation of impurity diffusivities in [alpha]-fe using first-principles methods. *Acta Materialia*, **58**, 1982–1993. [132](#)
- KANG, S. & YOON, D. (1982). Kinetics of grain coarsening during sintering of Co-Cu and Fe-Cu alloys with low liquid contents. *Metallurgical and Materials Transactions A*, **13**, 1405–1411. [152](#)
- LIFSHITZ, I. & SLYOZOV, V. (1961). The kinetics of precipitation from supersaturated solid solutions. *Journal of Physics and Chemistry of Solids*, **19**, 35–50. [127](#), [128](#)
- NITTA, H., YAMAMOTO, T., KANNO, R., TAKASAWA, K., IIDA, T., YAMAZAKI, Y., OGU, S. & IJIMA, Y. (2002). Diffusion of molybdenum in [alpha]-iron. *Acta Materialia*, **50**, 4117–4125. [132](#)
- SAMARAS, S. (2006). Modelling of microstructure evolution during precipitation processes: a population balance approach of the KWN model. *Modelling and Simulation in Materials Science and Engineering*, **14**, 1271. [127](#), [147](#)
- SUNDMAN, B., JANSSON, B. & ANDERSSON, J. (1985). The thermo-calc databank system. *Calphad*, **9**, 153–190. [129](#)

REFERENCES

- TAKEMOTO, S., NITTA, H., IJIMA, Y. & YAMAZAKI, Y. (2007). Diffusion of tungsten in α -iron. *Philosophical Magazine*, **87**, 1619–1629. [132](#)
- WAGNER, C. (1961). Theory of precipitate change by redissolution. *Electrochimie*, **65**, 581–591. [127](#), [128](#)

Chapter 5

Conclusions

Interphase precipitation has been observed by using transmission electron microscope for Ti-Nb and Ti-Nb-Mo bearing steels. The heat-treatment condition for the formation of interphase precipitation has been confirmed for Ti-Nb bearing steels and Ti-Nb-Mo bearing steels. The addition of Mo reduces the spacing of interphase (Ti,Nb,Mo)C and the size of the precipitates. The precipitates also at first contain a large amount of Mo. It appears that the incorporation of Mo into the carbide facilitates nucleation and reduces the particle coarsening rate relative to a steel containing the same amount of Ti but without Mo.

The formation energy, crystal lattice parameter and bulk moduli of (Ti,M)C and M(C,Va) with a B1 crystal structure have been investigated using first-principles calculations, where M represents Nb, V, Mo and W. The estimated lattice parameters and formation energies of TiC, NbC and VC with a perfect B1 structure are consistent with experimental data. Calculations show that the introduction of vacancies into the structure makes MoC and WC more stable. The calculated lattice parameters of Mo(C,Va) and W(C,Va) show that the replacement of Ti by Mo or W will reduce the misfit with ferrite, which facilitates easier nucleation. At the same time, the substitution of Ti by Mo or W will reduce the equilibrium Ti concentration in the ferrite matrix during coarsening, which

5. Conclusions

possibly decelerates the coarsening process of (Ti,M)C precipitation. The effect of W predicted by first-principles calculations is validated with a microstructural characterization on Ti-, Ti-Mo- and Ti-W- bearing model alloys. It is confirmed that Mo or W addition can mitigate the lattice mismatch between the carbide particle and the ferrite matrix as predicted by the calculations.

The effects of interfacial energy and Ti concentration in a matrix on coarsening rate have been studied based on the Lifshitz, Slyozov and Wagner (LSW) theory, the multicomponent diffusion-controlled transformations (DICTRA) model and Kampmann and Wagner's numerical (KWN) models. The simulated results show the higher coarsening rate for higher interfacial energy and higher Ti concentration in a matrix for the fixed system. The results from KWN model indicate faster coarsening rate than those from LSW and DICTRA models. The results from KWN model also show the convergence of normalized particle distribution function, which is different from the analytic function from LSW theory.

Acknowledgements

I would like to express my sincerely thanks to my supervisor, Professor, Dong-Woo Suh, who showed me the beauty of science and the fundamental attitude to be a researcher. I am extremely grateful to Professor Bhadeshia, H. K. D. H., my co-advisor, for his constant guidance, support and great friendship. I also thanks to Professor In-Gee Kim for his advise and guidance. I would like to show my gratitude to Professor, Byeong-Joo Lee for numerous fruitful discussions and speeches with great enthusiasm.

I am indebted to POSCO for their strong financial support and establishment of POSTECH and GIFT. I am also thankful to Dr. Jae-Kon Lee, who made available his support in a number of ways with encouragement.

I acknowledge to the past and present members of the Computational Metallurgy Laboratory (CML), in particular to Eun-Ju Song, Jae-Yong Chae, Joo-Hyun Ryu, Hong-Suk Yang, Jun-Hak Pak, Min-Sung Joo, You-Young Song, Tae-Ki Jung, Hong-Yeob Lee, Jeong-In Kim, Seung-Woo Seo, Geun-Su Jung, Jee-Yong Lee, Won-Seok Yun, Young-Bhum Kim and Eun-Jeong Kwon. It was an enormous pleasure to work with them.

I take this opportunity to express my gratitude to my family, specially my parents and younger brother Sung-Hyun, for everything. This thesis would not have been possible without their support and encouragement.

Lastly, I would like to show my gratitude to all of those who supported me in any respect during the completion of the project.

CURRICULUM VITAE

Name: Jang, Jae Hoon (장 재 훈)

E-mail: impurity@postech.ac.kr, impurity@posco.co.kr

Date of birth: 16 January, 1980

Place of birth: Pohang, South Korea

Education

Ph. D. 2012, POSTECH (Pohang, Korea), Graduate Institute of Ferrous Technology, Computational Metallurgy Group.

M. S. 2009, POSTECH (Pohang, Korea), Graduate Institute of Ferrous Technology, Computational Metallurgy Group.

B. S. 2007, POSTECH (Pohang, Korea), Department of Mathematics / Computer Science and Engineering.

Publication

Jang, J. H., Kim, I. G. and Bhadeshia, H. K. D. H., Substitutional solution of silicon in cementite: A first-principles study, *Computational Materials Science*, doi:10.1016/j.commatsci.2008.08.022, 2008.

Pak, J. H., Jang, J. H., Bhadeshia, H. K. D. H., and Karlsson, L., Optimization of Neural Network for Charpy Toughness of Steel Welds, *Materials and Manufacturing Processes*, doi:10.1080/10426910802540232, 2009.

Jae Hoon Jang, In Gee Kim and H. K. D. H. Bhadeshia, First-principles

calculations and the thermodynamics of cementite, *Materials Science Forum*, 638-642 (2010) pp3319-3324.

J. H. Jang, I. G. Kim and H. K. D. H. Bhadeshia, epsilon-carbide in alloy steels: First-principles assessment, *Scripta Materialia* 63 (2010) 121-123.

J. Y. Chae, J. H. Jang, G. H. Zhang, K. H. Kim, J. S. Lee, H. K. D. H. Bhadeshia and D. W. Suh, Dilatometric analysis of cementite dissolution in hypereutectoid steels containing chromium, *Scripta Materialia* 65 (2011) 245-248.

J. H. Jang, C. H. Lee, Y. U. Heo and D. W. Suh, Stability of (Ti,M)C (M=Nb, V, Mo and W) carbide in steels using first-principles calculations, *Acta Materialia* 60 (2012) 208-217.

H. S. Yang, J. H. Jang, H. K. D. H. Bhadeshia and D. W. Suh, Critical Assessment: Martensite Start-Temperature for the γ to ϵ Transformation, *CALPHAD* 36 (2012) 16-22.

Academic Activity

Jang, J. H., Kim, I. G. and Bhadeshia, H. K. D. H., First Principles Calculation and The Thermodynamics of Cementite, Thermec 2009, *International Conference on PROCESSING and MANUFACTURING OF ADVANCED MATERIALS Processing, Fabrication, Properties, Applications*, August 25-29, 2009, Berlin, Germany.

Jang, J. H., Suh, D. W., Kim, I. G. and Bhadeshia, H. K. D. H., Thermodynamic calculation of Fe-carbides based on databases with First-principle approach, *The 5th KIMS-Kyushu University Joint Symposium on Steel Research*, 2010, Fukuoka, Japan.

Jae Hoon Jang, In Gee Kim and H. K. D. H. Bhadeshia, Crystal structure and formation energy of epsilon-carbide, *CALPHAD XXXIX*, 2010,

Jeju, KOREA.

Jang, J. H., Kim, I. G., Bhadeshia, H. K. D. H. and Suh D. W., The Roll of Mo for TiC Precipitation Strengthening in HSLA steel : A first-principles study, Thermec 2011, *International Conference on PROCESSING and MANUFACTURING OF ADVANCED MATERIALS Processing, Fabrication, Properties, Applications*, August 1-5, 2011, Quebec, Canada.

Jang, J. H., Suh, D. W and Bhadeshia, H. K. D. H., Stability of (Ti,M)C (M=Nb, V, Mo and W) carbide in steels using first-principles calculation, *The 6th KIMS-Kyushu University Joint Symposium on Steel Research*, 2011, Seoul, Korea.